NASA/TM–2022–104606/Vol. 62

Technical Report Series on Global Modeling and Data Assimilation, Volume 62

Randal D. Koster, Editor

Climate Characteristics of the Atmospheric Analysis Increments from the GEOS S2S V3 AOGCM Replayed to MERRA-2

Yehui Chang, Siegfried Schubert, Randal Koster, Andrea Molod, and Young-Kwon Lim

September 2022

NASA STI Program ... in Profile

Since its founding, NASA has been dedicated to the advancement of aeronautics and space science. The NASA scientific and technical information (STI) program plays a key part in helping NASA maintain this important role.

The NASA STI program operates under the auspices of the Agency Chief Information Officer. It collects, organizes, provides for archiving, and disseminates NASA's STI. The NASA STI program provides access to the NTRS Registered and its public interface, the NASA Technical Reports Server, thus providing one of the largest collections of aeronautical and space science STI in the world. Results are published in both non-NASA channels and by NASA in the NASA STI Report Series, which includes the following report types:

- TECHNICAL PUBLICATION. Reports of completed research or a major significant phase of research that present the results of NASA Programs and include extensive data or theoretical analysis. Includes compilations of significant scientific and technical data and information deemed to be of continuing reference value. NASA counterpart of peer-reviewed formal professional papers but has less stringent limitations on manuscript length and extent of graphic presentations.

- TECHNICAL MEMORANDUM. Scientific and technical findings that are preliminary or of specialized interest, e.g., quick release reports, working papers, and bibliographies that contain minimal annotation. Does not contain extensive analysis.

- CONTRACTOR REPORT. Scientific and technical findings by NASA-sponsored contractors and grantees.

- CONFERENCE PUBLICATION. Collected papers from scientific and technical conferences, symposia, seminars, or other meetings sponsored or co-sponsored by NASA.

- SPECIAL PUBLICATION. Scientific, technical, or historical information from NASA programs, projects, and missions, often concerned with subjects having substantial public interest.

- TECHNICAL TRANSLATION. English-language translations of foreign scientific and technical material pertinent to NASA's mission.

Specialized services also include organizing and publishing research results, distributing specialized research announcements and feeds, providing information desk and personal search support, and enabling data exchange services.

For more information about the NASA STI program, see the following:

- Access the NASA STI program home page at http://www.sti.nasa.gov

- E-mail your question to help@sti.nasa.gov

- Phone the NASA STI Information Desk at 757-864-9658

- Write to:
  NASA STI Information Desk
  Mail Stop 148
  NASA Langley Research Center
  Hampton, VA 23681-2199

NASA/TM–2022–104606/Vol. 62

Technical Report Series on Global Modeling and Data Assimilation, Volume 62

Randal D. Koster, Editor

Climate Characteristics of the Atmospheric Analysis Increments from the GEOS S2S V3 AOGCM Replayed to MERRA-2

Yehui Chang
Morgan State University, Baltimore, MD

Siegfried Schubert
Science Systems and Applications Inc., Lanham, MD

Randal Koster
NASA Goddard Space Flight Center, Greenbelt, MD

Andrea Molod
NASA Goddard Space Flight Center, Greenbelt, MD

Young-Kwon Lim
University of Maryland, Baltimore County, Baltimore, MD

National Aeronautics and
Space Administration

Goddard Space Flight Center
Greenbelt, Maryland 20771

September 2022

Level of Review: This material has been technically reviewed by technical management.

Available from

NASA STI Program
Mail Stop 148
NASA's Langley Research Center
Hampton, VA 23681-2199

National Technical Information Service
5285 Port Royal Road
Springfield, VA 22161
703-605-6000

Table of Contents

List of Figures **3**

Executive Summary **13**

1.0 Introduction and Motivation **18**

2.0 The Model and Datasets **20**

2.1 The S2S Version 3 GEOS AOGCM *20*

2.2 MERRA-2 and other observational datasets *21*

2.3 The Replay Experiment *and Interpretation of the Increments* *23*

3.0 Results: The Atmospheric Increments from Replay **28**

3.1 Mean Annual and Diurnal Cycles of u, v, T and q increments *28*

a) Seasonal means of zonal means *28*

b) Seasonal means at selected levels *37*

c) The mean diurnal cycle *50*

d) The wind increments viewed in terms of stream function and velocity potential *57*

3.2 Variability of the increments and impacts of observational inhomogeneities 62

a) Stream function and velocity potential *64*

b) Temperature and moisture *81*

3.3 Correlations with atmospheric/ocean phenomena *97*

3.4 A more direct link between increments and model errors *115*

4.0 Concluding Remarks **123**

Acknowledgements and Data Availability **127**

Appendix: Additional Diagnostics **128**

References **131**

List of Figures

Figure 1: a) A schematic of the replay approach used to compute the analysis increments (IAU, or Δx in our current terminology) from an existing analysis (figure taken from Chang et al. 2019). Here IAU refers to the incremental analysis update procedure for performing data assimilation developed by Bloom et al. (1996). See also Takacs et al. (2018) for further information about the numerical stability of replay. b) A schematic of the evolution of the free running model's $[\frac{\partial x}{\partial t} = f(x)]$ climate drift which saturates to the climate bias at long leads. Replay $[\frac{\partial x}{\partial t} = f(x) + \Delta x\ ]$ provides information on the initial drift (the time mean of the increments or tendency bias).

Figure 2: The seasonal and zonal means of the u-wind analysis increments (shaded, m/s/day), with the tendency of the u-wind due to turbulence processes (black contours) and the time mean zonal wind (green contours) superimposed. Dashed contours indicate negative values. The results are from the GEOS S2S V3 AOGCM replayed to MERRA-2 averaged over the time period 1981-2016. The vertical axis is pressure in mb. Black contour levels are '-18 -16 -14 -12 -10 -8 -6 -4 -2 2 4 6 8 10 12 14 16 18' and contouring south of 70°S is suppressed due to the noisiness of the fields.

Figure 3: Same as Figure 2, but for the v-wind.

Figure 4a: The seasonal and zonal means of the temperature analysis increments (shaded, °C/day), with the tendency of the temperature due to moist processes superimposed (contour intervals are "-4.5 -4.0 -3.5 -3.0 -2.5 -2.0 -1.5 -1.0 -.5 .5 1.0 1.5 2.0 2.5 3.0 3.5 4.0 4.5", negative values have dashed contours). The results are from the GEOS S2S V3 AOGCM replayed to MERRA-2 averaged over the time period 1981-2016. The vertical axis is pressure in mb.

Figure 4b: The zonal mean of the long-term seasonal means of the temperature tendency due to moist processes from MERRA-2 (contoured, negative values have dashed contours), and the difference between Base 9 and replay (shaded). Units are (°C/day).

Figure 5: The seasonal and zonal means of the specific humidity analysis increments (shaded, g/kg/day), with the tendency of the specific humidity due to moist processes superimposed (contour interval is 0.5 g/kg/day, negative values have dashed contours). The results are from the GEOS S2S

V3 AOGCM replayed to MERRA-2 averaged over the time period 1981-2016. The vertical axis is pressure in mb. Note that the outermost contour corresponds to -0.5.

Figure 6: The seasonal and zonal means of the specific humidity analysis increments (shaded, g/kg/day), with the tendency of the specific humidity due to turbulence processes superimposed (contour interval is 0.5 g/kg/day, solid contours indicate positive values). The results are from the GEOS S2S V3 AOGCM replayed to MERRA-2 averaged over the time period 1981-2016. The vertical axis is pressure in mb.

Figure 7: The model level 72 (approximately 992mb) seasonal means of the u-wind analysis increments (shaded, m/s/day) with the u-wind superimposed (contour intervals are 2 m/s with negative values indicated by dashed contours). The results are from the GEOS S2S V3 AOGCM replayed to MERRA-2 averaged over the time period 1981-2016.

Figure 8: The 500mb seasonal means of the u-wind analysis increments (shaded, m/s/day) with the u-wind superimposed (contour intervals are 5 m/s with negative values indicated by dashed contours). The results are from the GEOS S2S V3 AOGCM replayed to MERRA-2 averaged over the time period 1981-2016.

Figure 9: The model level 72 (approximately 992mb) seasonal means of the v-wind analysis increments (shaded, m/s/day) with the v-wind superimposed (contour intervals are 1 m/s with negative values indicated by dashed contours). The results are from the GEOS S2S V3 AOGCM replayed to MERRA-2 averaged over the time period 1981-2016.

Figure 10: The model level 72 (approximately 992mb) seasonal means of the wind increments displayed as vectors (m/s/day), from the GEOS S2S V3 AOGCM replayed to MERRA-2 averaged over the time period 1981-2016. The shaded fields (mm/day) are the differences between the precipitation from the replay run and that of the free running model (without replay, internal designation is "base 9", see text).

Figure 11: Same as Fig. 10, but at model level 63 (approximately 857mb).

Figure 12: The 250mb seasonal means of the wind increments displayed as vectors (m/s/day), from the GEOS S2S V3 AOGCM replayed to MERRA-2 averaged over the time period 1981-2016.

Figure 13: The model level 72 (approximately 992mb) seasonal mean temperature increments normalized by the standard deviation of the monthly means (1/dispersion). The results are from the GEOS S2S V3 AOGCM replayed to MERRA-2 averaged over the time period 1981-2016. Units are standard deviations.

Figure 14: Same as Fig. 13, but at 650mb. Contours are the 650mb temperature.

Figure 15: Same as Fig. 13, but at 250mb.

Figure 16: The model level 72 (approximately 992mb) seasonal mean specific humidity increments normalized by the standard deviation of the monthly means (1/dispersion). The results are from the GEOS S2S V3 AOGCM replayed to MERRA-2 averaged over the time period 1981-2016. Units are standard deviations.

Figure 17: Same as Fig. 16, but at model level 63 (approximately 857mb).

Figure 18: The model level 72 (approximately 992mb) DJF mean temperature increment anomalies (°C/day) for 00z, 06Z, 12Z and 18Z. The results are from the GEOS S2S V3 AOGCM replayed to MERRA-2 averaged over the time period 1981-2016.

Figure 19: Same as Fig. 18, but for JJA.

Figure 20: The model level 72 (approximately 992mb) DJF mean specific humidity increment anomalies (g/kg/day) for 00z, 06Z, 12Z and 18Z. The results are from the GEOS S2S V3 AOGCM replayed to MERRA-2 averaged over the time period 1981-2016.

Figure 21: Same as Fig. 20, but for JJA.

Figure 22: Vertical cross sections (130°W to 60°W, from about 992mb to 500mb) at 35°N of the JJA v-wind increments (shaded, m/s/day) and v-wind (contoured with dashed contours indicating

negative values, m/s) for a) 00z, b) 06Z, c) 12Z and d) 18Z. The results are from the GEOS S2S V3 AOGCM replayed to MERRA-2 averaged over the time period 1981-2016.

Figure 23: Vertical cross sections (130°W to 60°W, from 1000mb to 500mb, on pressure levels) at 35°N of the JJA v-wind differences (Base9-RPL; shaded, m/s/day) and RPL v-wind (contoured with dashed contours indicating negative values, m/s) for a) 00z, b) 06Z, c) 12Z and d) 18Z. The results are from the GEOS S2S V3 AOGCM replayed to MERRA-2 averaged over the time period 1981-2016.

Figure 24: The model level 72 (approximately 992mb) seasonal mean stream function increments. The results are from the GEOS S2S V3 AOGCM replayed to MERRA-2 averaged over the time period 1981-2016. Units are 10^6 $m^2/s/day$.

Figure 25: Same as Fig. 24, but for 250mb.

Figure 26: The model level 72 (approximately 992mb) seasonal mean velocity potential increments. The results are from the GEOS S2S V3 AOGCM replayed to MERRA-2 averaged over the time period 1981-2016. Units are 10^6 $m^2/s/day$.

Figure 27: Same as Fig. 26, but for 250mb.

Figure 28: Left panels: the leading REOFs of the model level 72 (approximately 992mb) stream function increments. Right panels: the associated PCs plotted separately for each time of day. The REOFs were obtained from monthly anomalies that were computed separately for each time of day: 00z, 06z, 12z and 18z. The PCs were obtained by projecting the 6-hourly anomalies (obtained by removing separate 6-hourly climatologies for each time of day) onto the monthly REOFs (see text for details). The results are from the GEOS S2S V3 AOGCM replayed to MERRA-2 for 1981-2016.

Figure 29: The time series of the modulus of the wavelet decomposition of PC 1 of the model level 72 (approximately 992mb) stream function increments (see text for details). The results are from the GEOS S2S V3 AOGCM replayed to MERRA-2 for 1981-2016.

Figure 30: Same as Fig. 29 except for PC 2.

Figure 31: Left panels: the leading REOFs of the model level 72 (approximately 992mb) velocity potential increments. Right panels: the associated PCs plotted separately for each time of day. The REOFs were obtained from monthly anomalies that were computed separately for each time of day: 00z, 06z, 12z and 18z. The PCs were obtained by projecting the 6-hourly anomalies (obtained by removing separate 6-hourly climatologies for each time of day) onto the monthly REOFs (see text for details). The results are from the GEOS S2S V3 AOGCM replayed to MERRA-2 for 1981-2016.

Figure 32: The time series of the modulus of the wavelet decomposition of PC 1 of the model level 72 (approximately 992mb) velocity potential increments (see text for details). The results are from the GEOS S2S V3 AOGCM replayed to MERRA-2 for 1981-2016.

Figure 33: Same as Fig. 32 except for PC 2.

Figure 34: Left panels: the leading REOFs of the 250mb stream function increments. Right panels: the associated PCs plotted separately for each time of day. The REOFs were obtained from monthly anomalies that were computed separately for each time of day: 00z, 06z, 12z and 18z. The PCs were obtained by projecting the 6-hourly anomalies (obtained by removing separate 6-hourly climatologies for each time of day) onto the monthly REOFs (see text for details). The results are from the GEOS S2S V3 AOGCM replayed to MERRA-2 for 1981-2016.

Figure 35: The time series of the modulus of the wavelet decomposition of PC 1 of the 250mb stream function increments (see text for details). The results are from the GEOS S2S V3 AOGCM replayed to MERRA-2 for 1981-2016.

Figure 36: Same as Fig. 35 except for PC 2.

Figure 37: Left panels: the leading REOFs of the 250mb velocity potential increments. Right panels: the associated PCs plotted separately for each time of day. The REOFs were obtained from monthly anomalies that were computed separately for each time of day: 00z, 06z, 12z and 18z. The PCs were obtained by projecting the 6-hourly anomalies (obtained by removing separate 6-hourly climatologies for each time of day) onto the monthly REOFs (see text for details). The results are from the GEOS S2S V3 AOGCM replayed to MERRA-2 for 1981-2016.

Figure 38: The time series of the modulus of the wavelet decomposition of PC 1 of the 250mb velocity potential increments (see text for details). The results are from the GEOS S2S V3 AOGCM replayed to MERRA-2 for 1981-2016.

Figure 39: Same as Fig. 38 except for PC 2.

Figure 40: The time series of the real part of the wavelet decomposition of PC 3 of the 250mb velocity potential increments (see text for details). The results are from the GEOS S2S V3 AOGCM replayed to MERRA-2 for 1981-2016.

Figure 41: Left panels: the REOFs of the model level 72 (approximately 992mb) temperature increments. Right panels: the associated PCs plotted separately for each time of day. The REOFs were obtained from monthly anomalies that were computed separately for each time of day: 00z, 06z, 12z and 18z. The PCs were obtained by projecting the 6-hourly anomalies (obtained by removing separate 6-hourly climatologies for each time of day) onto the monthly REOFs (see text for details). The results are from the GEOS S2S V3 AOGCM replayed to MERRA-2 for 1981-2016.

Figure 42: The time series of the real part of the wavelet decomposition of PC 1 of the model level 72 (approximately 992mb) temperature increments (see text for details). The results are from the GEOS S2S V3 AOGCM replayed to MERRA-2 for 1981-2016.

Figure 43: Same as Fig. 42 except for PC 2.

Figure 44: The time series of the modulus of the wavelet decomposition of PC 3 of the model level 72 (approximately 992mb) temperature increments (see text for details). The results are from the GEOS S2S V3 AOGCM replayed to MERRA-2 for 1981-2016.

Figure 45: Left panels: the REOFs of the 250mb temperature increments. Right panels: the associated PCs plotted separately for each time of day. The REOFs were obtained from monthly anomalies that were computed separately for each time of day: 00z, 06z, 12z and 18z. The PCs were obtained by projecting the 6-hourly anomalies (obtained by removing separate 6-hourly climatologies for each time of day) onto the monthly REOFs (see text for details). The results are from the GEOS S2S V3 AOGCM replayed to MERRA-2 for 1981-2016.

Figure 46: The time series of the modulus of the wavelet decomposition of PC 1 of the 250mb temperature increments (see text for details). The results are from the GEOS S2S V3 AOGCM replayed to MERRA-2 for 1981-2016.

Figure 47: Same as Fig. 46 except for PC 2.

Figure 48: Same as Fig. 46 except for PC 3.

Figure 49: Left panels: the REOFs of the model level 72 (approximately 992mb) specific humidity increments. Right panels: the associated PCs plotted separately for each time of day. The REOFs were obtained from monthly anomalies that were computed separately for each time of day: 00z, 06z, 12z and 18z. The PCs were obtained by projecting the 6-hourly anomalies (obtained by removing separate 6-hourly climatologies for each time of day) onto the monthly REOFs (see text for details). The results are from the GEOS S2S V3 AOGCM replayed to MERRA-2 for 1981-2016.

Figure 50: The time series of the real part of the wavelet decomposition of PC 1 of the model level 72 (approximately 992mb) specific humidity increments (see text for details). The results are from the GEOS S2S V3 AOGCM replayed to MERRA-2 for 1981-2016.

Figure 51: Same as Fig. 50 except for PC 2.

Figure 52: Left panels: the REOFs of the model level 63 (approximately 857mb) specific humidity increments. Right panels: the associated PCs plotted separately for each time of day. The REOFs were obtained from monthly anomalies that were computed separately for each time of day: 00z, 06z, 12z and 18z. The PCs were obtained by projecting the 6-hourly anomalies (obtained by removing separate 6-hourly climatologies for each time of day) onto the monthly REOFs (see text for details). The results are from the GEOS S2S V3 AOGCM replayed to MERRA-2 for 1981-2016.

Figure 53: The time series of the real part of the wavelet decomposition of PC 1 of the model level 63 (approximately 857mb) specific humidity increments (see text for details). The results are from the GEOS S2S V3 AOGCM replayed to MERRA-2 for 1981-2016.

Figure 54: Same as Fig. 53 except for PC 4.

Figure 55: Middle panels: The Antarctic Oscillation (AAO) determined here as the first REOF (22% explained variance) of the SH 700mb mean height using monthly ERA5 data for the period 1981-2016, and the associated PC time series. Top left panels: the correlations between the AAO and a) the 250mb velocity potential increments, and b) the model level 72 (approximately 992mb) velocity potential increments. Bottom left panels: the correlations between the AAO and a) the 250mb stream function increments, and b) the model level 72 (approximately 992mb) stream function increments. Top right panels: the correlations between the AAO and a) the model level 63 (approximately 992mb) specific humidity increments, and b) the model level 72 (approximately 992mb) specific increments. Bottom right panels: the correlations between the AAO and a) the 250mb temperature increments, and b) the model level 72 (approximately 992mb) temperature increments.

Figure 56: Same as Fig. 55 except for the Arctic Oscillation (AO). The AO is determined here as the first REOF (13.5% explained variance) of the NH 1000mb monthly ERA5 height data for the period 1981-2016.

Figure 57: Same as Fig. 55 except for the North Atlantic Oscillation (NAO). The NAO is determined here as the second REOF (7.3% explained variance) of the NH 500mb monthly ERA5 height data for the period 1981-2016.

Figure 58: Same as Fig. 55 except for the Pacific/North American (PNA) pattern. The PNA is determined here as the fourth REOF (5.4% explained variance) of the NH 500mb monthly ERA5 height data for the period 1981-2016.

Figure 59: Same as Fig. 55 except for the Niño3.4 index, and the middle panel shows the correlations between the Niño3.4 index and SST globally.

Figure 60: Same as Fig. 55 except for the PDO index. The PDO is determined here as the third REOF (6.4% explained variance) of the monthly NOAA Extended Reconstructed Sea Surface Temperature (ERSST) data for the period 1981-2016.

Figure 61: The Madden-Julian Oscillation (MJO) as determined from the first two rotated complex EOFs (RCEOFs) of the daily filtered (time scales longer than 10 days) 250mb velocity potential

field computed from MERRA-2 data for the period 1980-2018. The first RCEOF explains 35% of the variance while the second explains 17% of the variance. The different panels indicate the different phases of the waves as they complete a circuit of the globe. See text for details.

Figure 62: Composites associated with RCEOF 1 (contours), of the specific humidity increments at model level 63 (approximately 857mb, left panels) and those at model level 72 (approximately 992mb, right panels). The composites are based on those time periods when the associated complex PC 1 has magnitudes exceeding 1 standard deviation during 1981-2016.

Figure 63: Same as Fig. 62 except for RCEOF 2.

Figure 64: The correlations between the monthly averaged PCs associated with the seven leading REOFs of the analysis increments and the monthly indices of the various climate modes (AO, AAO, PNA, AAO, PDO, and Niño3.4) for: a) the stream function increments at model level 72, b) the stream function increments at 250mb, c) the velocity potential increments at model level 72, d) the velocity potential increments at 250mb, e) the temperature increments at model level 72, f) the temperature increments at 250mb, g) the specific humidity increments at model level 72, h) the specific humidity increments at model level 63. Correlations with absolute values greater than 0.19 are significant at the 1% level (highlighted in red). See text for details.

Figure 65: The correlations between the increments of the temperature at the lowest model level (L=72) at time (*n*) and the corresponding temperature field one day earlier corr(ΔT_n, T_{n-1}) for a) JJA, b) DJF, and c) annual. The calculation of the 1-day lag correlations includes all times of the day (00z, 06z, 12z and 18z). See text for details.

Figure 66: The correlations between the increments of the specific humidity at the lowest model level (L=72) at time (*n*) and the corresponding specific humidity field one day earlier corr($\Delta \mathrm{q}_n$, q_{n-1}) for a) JJA, b) DJF, and c) Annual. The calculation of the 1-day lag correlations includes all times of the day (00z, 06z, 12z and 18z). See text for details.

Figure 67: The correlations between the increments of the specific humidity at model level 63 at time (n) and the corresponding specific humidity field one day earlier corr(Δq_n, q_{n-1}) for a) JJA, b) DJF, and c) Annual. The calculation of the 1-day lag correlations includes all times of the day (00z, 06z, 12z and 18z). See text for details.

Figure A1: Left set of panels: The seasonal mean precipitation from the replay run (top panels) and the free running model (bottom panels). Right set of panels: the same as left but for the differences with respect to the MERRA-2 corrected precipitation. Units: mm/day.

Figure A2: Left set of panels: The seasonal mean SST bias with respect to Reynolds for the replay run (left panels) and the free running model (right panels). Units: °C. Right set of panels: The seasonal mean surface latent energy flux bias with respect to MERRA-2 for the replay run (left panels) and the free running model (right panels). Units: W/m^2.

Executive Summary

The history of analysis increments produced as a biproduct of a reanalysis provide an important source of information for addressing model deficiencies. This is facilitated by the NASA Global Modeling and Assimilation Office's (GMAO's) development of a "replay" capability (Takacs et al. 2018), which can be used with any model and any existing reanalysis to produce a history of analysis increments (difference between an existing analysis and the first guess) specific to that model. As such, replay provides an important tool for model development without the need to build a full-blown data assimilation infrastructure around the model in question. We present here an analysis of the climate characteristics of the analysis increments obtained from replaying the latest version of the NASA/GMAO GEOS coupled model to the MERRA-2 atmospheric reanalysis for the period 1981-2016. The ultimate goal of this study is to use information about the analysis increments to extend the TBC approach of Chang et al. (2019) – to introduce, for example, state-dependent bias corrections – in the hopes of improving subseasonal to seasonal predictions.

The results presented here are comprehensive and can be viewed as a reference for anyone interested in obtaining an in-depth assessment of this version of the NASA/GMAO GEOS S2S coupled model's short-term (6-hourly) analysis increment biases and variability, including the extent to which that variability reflects changes in the observing system and/or dependencies on climate variability. Furthermore, we hope this study can provide a framework for the type of in-depth analysis of model errors that can be done routinely as major new versions of the S2S model come on-line. The results include an assessment of the mean annual and diurnal cycles of u, v, T and q increments and the (non-systematic) variability of those increments on semi-diurnal to decadal time scales. The systematic (time mean) components of the increments are compared with the model's

physical forcing terms to provide some insight into how the increments appear in some cases to be correcting those physical forcing terms. To make the assessment of the non-systematic variability of the increments tractable we decompose it into rotated empirical orthogonal functions (REOFs) and focus on the leading modes. The time variability associated with those REOFs (the principal components or PCs) is analyzed using a wavelet analysis to allow a clearer picture of how the spectral properties of the increments change over time. The potential connections to climate variability are quantified by examining the links (based on correlations or composites) between the increments and some of the leading modes of climate variability: the AAO, the AO, the NAO, the PNA, the MJO, ENSO (Niño3.4) and the PDO. Finally, we present a linear framework for more directly linking the time-variability of the increments to potential deficiencies in the model formulation of the physical forcing terms, together with some preliminary results.

The following lists some of the highlights of our analysis.

1) The time mean increments appear to correct, in part, biases linked to deficiencies in the model's physical parameterizations. In particular we find that:
    a. The zonal mean increments are drying (and warming) much of the boundary layer and moistening (and cooling) the levels just above that, presumably compensating for deficiencies in the model's boundary layer moist physics and turbulent vertical transport. Spatially, this problem is concentrated over the subtropical oceans.
    b. There is an overall tendency for the temperature increments to warm the equatorial upper troposphere during all seasons, thereby correcting what is apparently insufficiently deep tropical heating due to the model's moist processes.

c. The increments act to correct the tendency for the free running model to produce an unrealistic double ITCZ, as reflected in the changes in the zonal mean moist heating profiles and precipitation, especially during DJF.

d. The temperature increments act to warm the lower troposphere in both the NH and SH storm tracks, suggesting that the model may be producing insufficient heating associated with middle latitude synoptic-scale disturbances. This appears to be tied to the free-running model's insufficient transient eddy activity, especially $\omega'T'$.

e. The wind increments act to suppress convergence in the tropical Pacific boundary layer, while above that, the wind increments are acting to enhance the upward motion (producing anomalous low-level convergence and upper-level divergence) and presumably acting to increase the precipitation. As such, these results suggest that the source of the excessive tropical Pacific precipitation likely lies in the boundary layer formulation.

f. Composites of the moisture increments over the different phases of the MJO indicate that the model is deficient in moving moisture out of the boundary layer at the leading edge of the active region of the MJO (where the rising motion occurs) – moisture the MJO presumably needs to advance the area of rising motion eastward. Somewhat paradoxically, the increments also indicate that the active phase of the MJO (as it moves across the dateline) leaves in its wake a too dry boundary layer and excessively wet conditions overhead.

g. The JJA wind increments are for the most part negative within the domain of the U.S. Great Plains Low Level Jet (GPLLJ) during all times of the day, consistent with the fact that the free-running model has an excessively strong GPLLJ. It is noteworthy

that negative increments underneath the LLJ maximum extend to the surface, suggesting that there may be insufficient surface friction in the model.

2) The variability of the increments has rather complicated structures in both space and time, reflecting in part changes in the observing system. This is especially true for the specific humidity and temperature increments, and less so for the non-divergent wind increments. In particular,
    a. A significant fraction of the increment variability is in the semi-diurnal (two cycles per day) and diurnal cycles reflecting differences in the predominate observational type entering the analysis at different times of the day. This variability in many cases varies dramatically over the course of the 36 years (1981-2016), reflecting changes in the observing system used to produce MERRA-2.
    b. A major shift in the character of the increments tends to occur around the year 2000 (+/- 2 years) and appears to be associated with the introduction of AMSU and AIRS data.
    c. Some of the largest long-term changes in the character of the near surface temperature and moisture increment variability occur in the high latitude SH at the ice margins and likely reflects changes in the MERRA-2 boundary forcing (SST and sea ice) data.

3) Despite the above impacts of the changing observing system, there do appear to be substantial dependencies (on monthly time scales) of the increments on various climate modes of variability. In particular, significant correlations are found with the AO, NAO, AO and PNA. Links are also found with the PDO and ENSO, with some of the strongest

correlations occurring between the Niño3.4 index and the temperature and moisture increments in the tropical Pacific.

4) A more direct link between the increment variability and model error is quantified assuming a linear propagator as an approximation to the GEOS coupled model. Within that framework we show that the model propagator could be corrected/improved by adding a term which essentially involves the correlations between the increments and the previous analysis. A preliminary assessment of those correlations indicates that the model tends to produce near surface fluctuations that have excessively long time scales over the oceans and excessively short time scales over land, especially during DJF.

Introduction and Motivation

The history of analysis increments produced as a biproduct of a reanalysis provide an important source of information on model deficiencies. These deficiencies, which manifest themselves as biases in the analysis increments (analysis minus first guess, see Section 2.3 and Fig. 1a), can in fact be used to correct the model employed in the reanalysis (Chang et al. 2019). NASA's Global Modeling and Assimilation Office (GMAO) developed a "replay" capability (Takacs et al. 2018, see section 2.3) that allows recovering the analysis increments for a given model design from an existing reanalysis with little more than the cost of performing a model simulation. In fact, the replay approach can, in principle, be used with any model and any existing reanalysis to develop a history of analysis increments specific to that model. As such, replay (including regional replay, see Schubert et al. 2019) serves as an important tool for model development that makes use of analyzed weather but avoids the need to build a full-blown data assimilation infrastructure around the model in question.

Here we examine the history of analysis increments produced from a replay to the MERRA-2 atmospheric reanalysis. The model in question in this case is a recent version of the GEOS coupled atmospheric/ocean model (see Section 2). Here it is important to emphasize that we are not only replaying to an atmospheric model different from that used to produce MERRA-2 (it is a much up-dated version), we are replaying to an atmospheric model coupled to an ocean/ice model. We have in fact found that replaying the atmosphere in a coupled environment produces analysis increments that differ substantially from those produced when replaying the same atmospheric model within an atmosphere-only framework, highlighting the need to address coupled model error through a replay in a coupled environment (Chang et al. 2019). While replaying to the ocean, in addition to the

atmosphere, seems like a natural approach for replaying with a coupled model, we have not done that here. Our focus here is on improving the atmospheric component of the coupled model, and we believe that there is some advantage to not correcting the ocean in the process of replaying. For example, it may be advantageous to take a two-step approach to addressing potential atmosphere/ocean coupling errors (replaying first to the atmosphere and then to both the ocean and atmosphere) to better isolate the source of the model deficiencies. In any event, there are additional challenges involved with generating a consistent long-term history of analysis increments for the ocean, given the sparseness of the subsurface observational record prior to the early 2000s (prior to the deployment of Argo floats, Argo (2000)). Nevertheless, given some early successes in utilizing the ocean analysis increments to correct a coupled model bias (Lu et al. 2020), we do plan to pursue the more comprehensive approach in the near future.

The systematic components of analysis increments are of course not fully reflective of model bias; they may, in part, reflect biases in the observations being assimilated (Gelaro et al. 2017). While considerable progress has been made in correcting observational biases (e.g. Dee and Todling 2000; Dee and Uppala 2009), there is to some extent still an interplay between model and observational biases that make the interpretation of the analysis increment biases a challenge. Here, in our analysis of the replay results, we rely heavily on a comprehensive assessment of the observations assimilated in MERRA-2 produced by McCarty et al. (2016).

It is important to emphasize that our ultimate goal here is not to address MERRA-2 quality; rather, it is to better understand and potentially correct coupled model error based on the information contained in the analysis increments. In particular, by quantifying the long-term variability (the climate

characteristics) of the analysis increments obtained from the coupled model replay to MERRA-2, we hope to be able to use that information to refine the TBC approach of Chang et al. (2019), e.g., by allowing TBC to utilize state-dependent bias corrections.

This report is organized as follows. Section 2 describes the model and datasets. Our assessment of the climate characteristics of the replayed increments is presented in section 3. Section 4 provides some concluding remarks. The Appendix provides some additional diagnostics geared to an assessment of the quality of some of the surface flux fields over the ocean.

2. The Model and Datasets

2.1 The S2S Version 3 GEOS AOGCM

This study uses version 3 of the GEOS S2S Atmosphere-Ocean General Circulation Model (AOGCM). The S2S designation indicates that it is the GEOS model tailored for the GMAO's subseasonal to seasonal (S2S) prediction efforts.

GEOS S2S-3 is fundamentally similar to version 2 (described below). It does, however, include advancements geared to improving the simulation of the ocean. The model also underwent a major tuning exercise that resulted in substantial reductions of the biases in the simulation of sea surface temperature, net surface heating, and atmospheric temperature, humidity and winds (Molod et al. 2022). As described in Molod et al. (2020), the main components of the GEOS S2S V2 (and V3) AOGCM are the GEOS atmospheric general circulation model [Molod et al., 2015; Rienecker et al., 2008], the Catchment land surface model [Koster et al., 2000], the Goddard Chemistry Aerosol

Radiation and Transport (GOCART) aerosol model [Chin et al, 2002; Colarco et al, 2010], the Modular Ocean Model-5 (MOM5) ocean general circulation model [Griffies et al., 2005; Griffies, 2012], and the Community Ice CodE-4 (CICE 4) sea ice model [Hunke and Lipscomb, 2008].

The GEOS AGCM simulates large-scale transport and dynamics with an adaptation of the flux-form semi-Lagrangian (FFSL) finite-volume (FV) dynamics of Lin [2004], adapted for a cubed sphere horizontal discretization [Putman and Lin, 2007]. A comprehensive description of baseline versions of the physical parameterizations, which include convection, cloud macro- and micro-physics, longwave and shortwave radiation, turbulence, and gravity wave drag, is found in Rienecker et al. [2008], and the updates used within a more recent version of the AGCM are found in Molod et al. [2015].

For all the results presented here, the AGCM component was run at ~0.5° spatial resolution (on a cubed sphere grid) with 72 hybrid sigma/pressure levels, while the OGCM was run at ~0.25° with 50 levels. While almost all of the results presented here are from the replay run, we do (on a very limited basis) make comparisons with the results of a long free-running (without replay) simulation performed with the same model. This ~200-year simulation is hereafter referred to as the "Base 9" simulation.

2.2 MERRA-2 and other observational datasets

The atmospheric reanalysis data used for this study is the Modern-Era Retrospective analysis for Research and Applications version 2 (MERRA-2; Gelaro et al. 2017). MERRA-2, developed by

NASA Goddard Space Flight Center (GSFC) / Global Modeling and Assimilation Office (GMAO), is an updated version of MERRA (Rienecker et al. 2011) that includes an improvement of the assimilating model's physical parameterizations of moist processes, turbulence, land and ocean surface processes, and gravity wave drag (Bosilovich et al. 2015; Molod et al. 2015; Gelaro et al. 2017). Other differences from MERRA include aerosol data assimilation, as well as new developments in the representation of ozone and in the use of precipitation observations to force the land surface. The horizontal resolution of the MERRA-2 data is 0.625° longitude × 0.5° latitude. The key variables examined here consist of the precipitation, temperature, specific humidity, winds and geopotential heights. We note, however, that the MERRA-2 precipitation used in this study for verification is an observationally-corrected product in which the precipitation generated by the atmospheric model underlying MERRA-2 was merged with gauge and satellite precipitation observations (Reichle and Liu 2014, Reichle et al. 2017). In the following, we will use the words observations and MERRA-2 interchangeably with, of course, the understanding that MERRA-2 is a reanalysis product that combines a model-based first guess with observations and, as such, the reanalysis products are themselves potentially impacted by model biases.

While most of the results presented here are based on MERRA-2 (the replay experiment), we also, on a more limited basis (in Section 3.3), make use of ERA5 (C3S 2017) and the NOAA Extended Reconstructed Sea Surface Temperature (ERSST) data. Also, in the Appendix the SST biases are calculated with respect to the observational product produced by Reynolds et al. (2002).

2.3 The Replay Experiment and Interpretation of the Increments

As noted in the Introduction, the focus of this study is on the results of a replay experiment in which the GEOS S2S V3 AOGCM is replayed to MERRA-2. The replay experiment is carried out for the period 1981-2016. In the following we briefly review the replay approach.

The replay methodology takes advantage of the incremental analysis update (IAU) procedure (Bloom et al. 1996) employed in the GEOS data assimilation system (Rienecker et al. 2008) in which the equations governing the assimilation have the form:

$$\frac{\partial x}{\partial t} = f(x) + \Delta x \qquad (1)$$

where $\Delta x = (analysis - forecast)/6hrs$ is the instantaneous analysis increment (applied to the model's prognostic variables), and f(x) consists of all the dynamics and physics terms of the model (f(x) thus basically representing the changes induced by the uncorrected model).

As described in Takacs et al. (2018) and Chang et al. (2019), replay (see Fig. 1a) takes advantage of the incremental analysis update (IAU) procedure employed in the GEOS data assimilation system to force a model to track a *pre-existing analysis*. The equations governing replay have the same form as noted earlier for the assimilation (see eq. 1). The difference from the assimilation is that now the analysis used in computing $\Delta x = (analysis - forecast)/6hrs$ is a pre-existing analysis which is simply read in during the course of the integration (Figure 1a). As such, the increments from replay are a more direct estimate of the tendency biases for that particular model. It should be noted that had we employed the exact same version of the model used to produce MERRA-2 (here we did not,

since the atmospheric model is a newer version and coupled to the ocean, see above), the replay increments (Δx) would be the same as those obtained from MERRA-2. This, in fact, highlights another key advantage of replay – the ability to recreate exactly an existing reanalysis without having to actually redo the analysis with the full data assimilation system.

We note that while the algorithm for replaying to MERRA-2 with a coupled model has the option of running with a "dual ocean" in which the AGCM is forced with observed SST during the forecast phase (Fig. 1a), that was not done here. This has been shown to produce improved surface fluxes and correct problems with salinity and the ocean circulation. An inspection of the surface fluxes here, however, showed no apparent problems with the fluxes or SST (see the Appendix), though we have not looked at the subsurface ocean in this run. Furthermore, we did not replay aerosols.

Figure 1b illustrates the climate drift of the model, highlighting the tendency bias (the initial drift) obtained from replay and the final drift (long term bias) of the free running model. To help in the interpretation of the time mean increments (retaining the diurnal and annual cycles, Section 3.1) and the potential link to model error we consider three different averages. These are:

$$\overline{f_1(x)}^{(m)} + \overline{f_2(x)}^{(m)} + \cdots \overline{f_N(x)}^{(m)} \qquad = 0, \tag{2a}$$

$$\overline{f_1(x)}^{(r)} + \overline{f_2(x)}^{(r)} + \cdots \overline{f_N(x)}^{(r)} + \qquad \overline{\Delta x}^{(r)} = 0, \tag{2b}$$

$$\overline{g_1(x)}^{(r)} + \overline{g_2(x)}^{(r)} + \cdots \overline{g_N(x)}^{(r)} + \qquad \overline{g_{N+1}(x)}^{(r)} + \overline{g_{N+2}(x)}^{(r)} + \cdots = 0. \tag{2c}$$

Here, (2a) is the time mean budget of the free running model, where $\overline{f_k(x)}^{(m)}$ is the long-term average of the kth component of the model's physics/dynamics terms, and the averaging is done over the free-running model's climate (denoted by m). Similarly, (2b) is the time mean budget of the replay run, where $\overline{f_k(x)}^{(r)}$ is again the long-term average of the kth component of the model's physics/dynamics terms, but here the averaging is done over the reanalysis climate (denoted by r). Finally, (2c) is the time mean budget of a hypothetical perfect model, where $\overline{g_k(x)}^{(r)}$ is the long-term average of the kth component of the perfect model's physics/dynamics terms, and the averaging is again done over the reanalysis climate (denoted by r). Here we include additional physics/dynamics terms (N+1, N+2, …) to allow for the possibility that the current model is missing processes that occur in nature (the perfect model). By comparing (2a) and (2b), we will examine in the following (Section 3a) whether replay produces better estimates of the various forcing terms compared with those of the free running model. In terms of the above equations (2), we are asking whether the following inequality is true (here, $\| \ \|$ refers to magnitude):

$$\left\| \overline{f_k(x)}^{(r)} - \overline{g_k(x)}^{(r)} \right\| < \left\| \overline{f_k(x)}^{(m)} - \overline{g_k(x)}^{(r)} \right\|, \text{ k=1,…, N.} \tag{3}$$

If true, we can say that the analysis increments are correcting *non-structural model deficiencies*. Furthermore, comparing 2(b) and (2c), we are equating the time mean increments with potentially missing physical processes, though this could also include corrections associated with, say, inadequate resolution or incorrectly tuned versions of the current model's parameterizations. We say that the time mean increments are correcting *structural model deficiencies*, and a key challenge will be to interpret the time mean increments in terms of specific deficiencies in the model formulation.

Finally, we also examine whether there is information about model error associated with the time variability of the increments. That is, is there a state-dependence of the increments? We address this question in two different ways. One way (Section 3.3) considers whether the increments (and therefore model error) vary systematically in association with specific climate modes of variability. For example, a dependence of the increments on the phase of the MJO could reflect model deficiencies such as insufficient preconditioning of the moisture at the leading edge of the MJO. We should note, however, that dependencies of the increments on climate modes of variability could occur even in a perfect model, given, for example, that the magnitude of atmospheric variability (and thus the potential size of the increments) can change with the phase of a climate mode (e.g., ENSO). The other approach we take (Section 3.4) looks more directly at the link between the variability in the increments and model error, formulating a correction to the model in a linear framework.

a

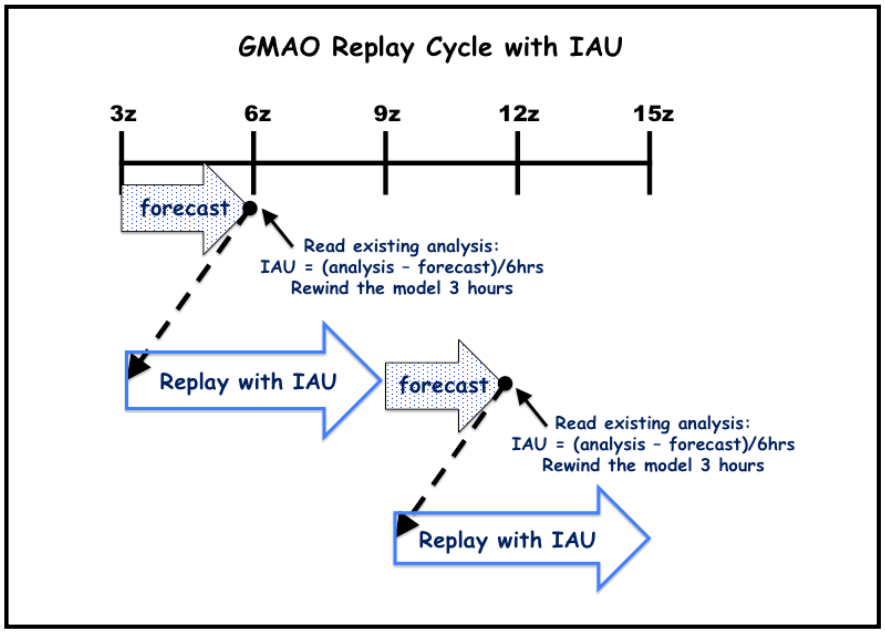

b

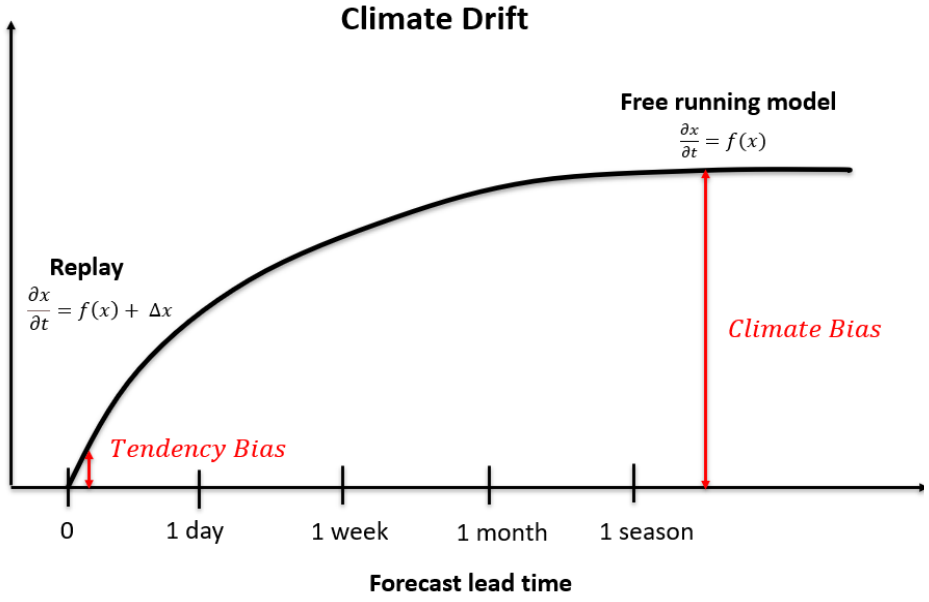

Figure 1: a) A schematic of the replay approach used to compute the analysis increments (IAU, or Δx in our current terminology) from an existing analysis (figure taken from Chang et al. 2019). Here IAU refers to the incremental analysis update procedure for performing data assimilation, as developed by Bloom et al. (1996). See also Takacs et al. (2018) for further information about the numerical stability of replay. b) A schematic of the evolution of the free running model's $[\frac{\partial x}{\partial t} = f(x)]$ climate drift which saturates to the climate bias at long leads. Replay $[\frac{\partial x}{\partial t} = f(x) + \Delta x\ ]$ provides information on the initial drift (the time mean of the increments, or tendency bias).

In the interpretation of our results, we of course must keep in mind that the observing system used in producing MERRA-2 is not constant and as such can introduce spurious variability into the replayed increments that having nothing to do with model error. We address this in Section 3.2.

3. Results: The Atmospheric Increments from Replay

In the following two sections we present various climate characteristics of the increments, including in Section 3.1 their mean annual and diurnal cycles, zonal means and global distributions, and in Section 3.2 their variability on time scales ranging from 6 hourly to decadal (to the extent the latter time scales are resolved in the 3 1/2 decades of replay examined here). To help interpret the increments, we include in some of the figures certain aspects of the replayed fields themselves, such as the corresponding state variables or the relevant model physics terms. In a few cases, we also compare the replay results with those from a long free-running model simulation (the Base 9 simulation, see Section 2.1). When examining the increment variability, we also try to assess whether any unusual behavior is tied to changes in the observing system. Section 3.3 focuses on the extent to which the behavior of the increments is linked to specific climate phenomena, while Section 3.4 looks at whether we can use information about the variability of the increments to more directly identify and quantify deficiencies in the model formulations.

3.1 Mean Annual and Diurnal Cycles of u, v, T and q increments

a) Seasonal means of zonal means

We begin by examining the zonal mean increments for each season with a focus on the troposphere. Figure 2 shows the zonal mean u-wind increments for each season. In order to better orient the

reader, the mean zonal winds (from the replay run) are superimposed on the increments with green contours. A second set of contours (black) shows the zonal wind eastward tendency due to the model's turbulence processes. A general feature of the increments is the tendency for positive values to occur in the middle latitude (30° - 60°) boundary layers of both hemispheres, while negative values occur in the boundary layer centered at about 60°N during DJF, MAM and SON. In the upper troposphere, during DJF, MAM and SON, the increments are acting to shift the NH jet equatorward. During DJF and MAM, just below the jet maximum at about 30°N, the increments are positive and are acting to counter the dissipation from the turbulence scheme. The tropical increments tend to be negative in the mid troposphere especially during JJA. In the SH, there is a general tendency for negative increments poleward of about 60°S during all seasons, acting to counter the dissipation from the turbulence scheme there, while just to the north of that (on the poleward flank of the jet) the increments are acting to strengthen the westerlies. We will take a closer look at the u-wind increments at specific levels later in this section.

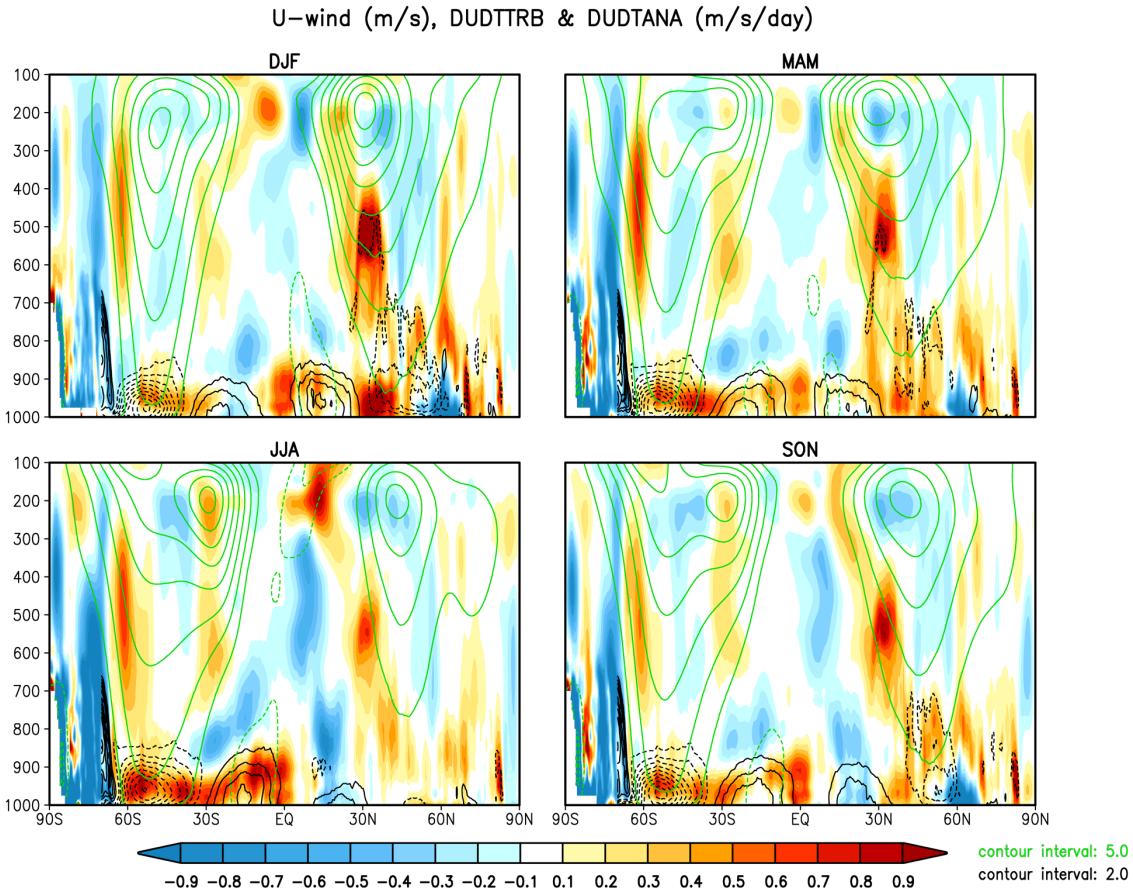

Figure 2: The seasonal and zonal means of the u-wind analysis increments (shaded, m/s/day), with the tendency of the u-wind due to turbulence processes (black contours) and the time mean zonal wind (green contours) superimposed. Dashed contours indicate negative values. The results are from the GEOS S2S V3 AOGCM replayed to MERRA-2 averaged over the time period 1981-2016. The vertical axis is pressure in mb. Black contour levels are '-18 -16 -14 -12 -10 -8 -6 -4 -2 2 4 6 8 10 12 14 16 18' and contouring south of 70°S is suppressed due to the noisiness of the fields.

Figure 3 shows the zonal mean v-wind increments (shaded) with the superimposed tendency due to turbulence (black contours) and the mean-v-wind (green contours). The v-wind shows the expected strong annual cycle, with the Hadley cell shifted into the NH in DJF and into the SH in JJA, and with the transition seasons showing Hadley Cells more centered on the equator. The increments have somewhat noisy structures, though a few things stand out. During both JJA and SON positive increments act to strengthen the northern edge (just north of the equator) of the lower tropospheric

return branch of the Hadley Cell. During the transition seasons (MAM and SON) the increments act to increase the height of the lower tropospheric return flow in the tropics of both hemispheres, and as such act to increase the convergence just above the boundary layer between about 800mb-900mb. In the upper troposphere the increments tend to strengthen the equatorial outflow during all seasons. There is also some tendency to weaken the lower tropospheric branches of the Polar and Ferrel Cells in the SH. Near the surface, there is a tendency for the increments to reduce the equatorial inflow and therefore effectively enhance the near surface dissipation.

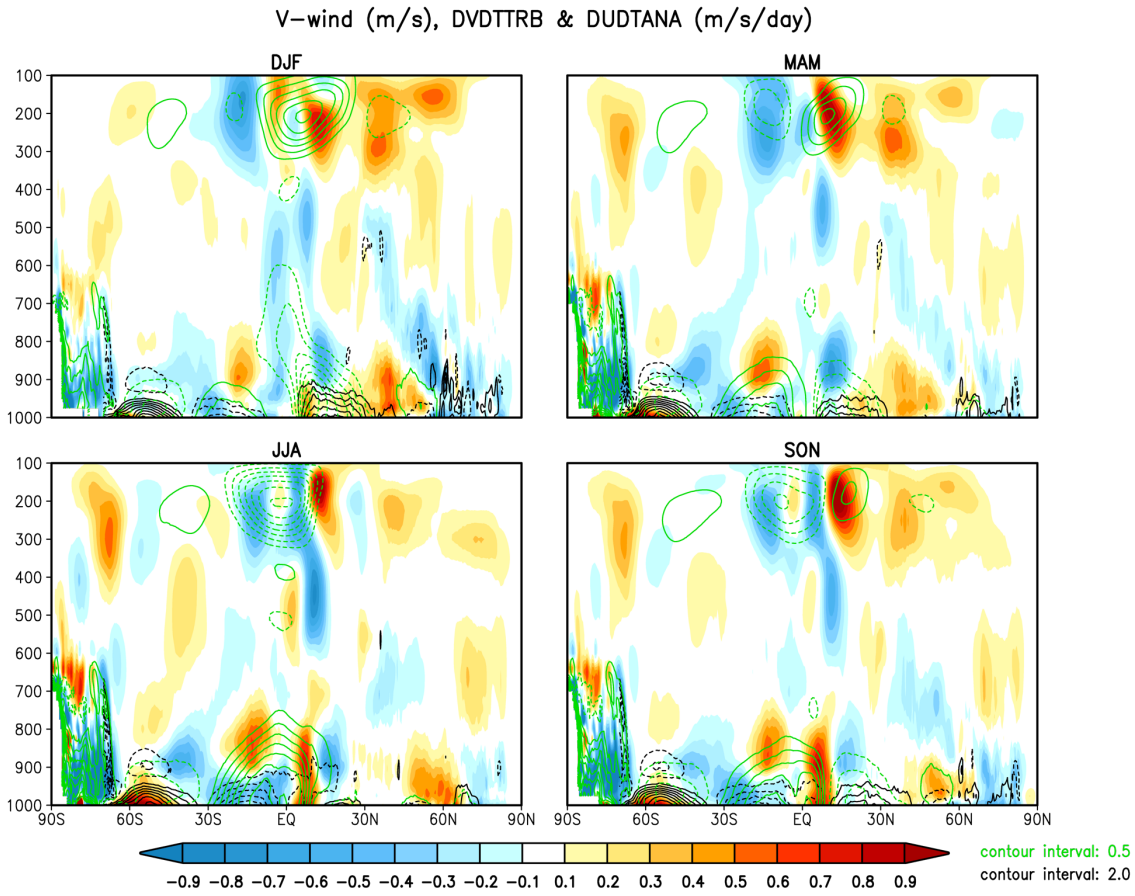

Figure 3: Same as Figure 2, but for the v-wind.

The zonal mean temperature increments (Fig. 4a) act to warm much of the troposphere below about 900 mb, counteracting the strong cooling from moist processes. On the other hand, there is an overall tendency for the increments to cool the troposphere above the boundary layer between about 900mb and 800mb (countering the warming there due to moist processes). The increments produce a warming tendency in the equatorial upper troposphere (with cooling below that, especially at about 650mb) during all seasons, where they support an upward extension of the tropical deep heating due to moist processes. While we suspect the insufficient deep heating primarily reflects errors in the model's moist convective heating, it likely also involves errors in cloudiness and the heating from longwave and shortwave radiation. Disentangling such errors is however beyond the scope of this study.

The increments also act to warm the lower troposphere in the SH middle latitudes during all seasons, supporting the warming due to moist processes. This suggests that the model may be producing insufficient heating associated with SH middle latitude synoptic-scale disturbances. We will look at that in more detail when examining the spatial distributions of the temperature increments at selected levels in Section 3.1b. A key question posed in Section 2.3 has to do with whether the heating profiles from the replay shown in Fig. 4 are a more accurate representation of the true heating profiles compared to that produced by the free running model. A well-known problem with coupled models is the tendency to produce a double ITCZ. This is true for the S2S v3 model (see Appendix).

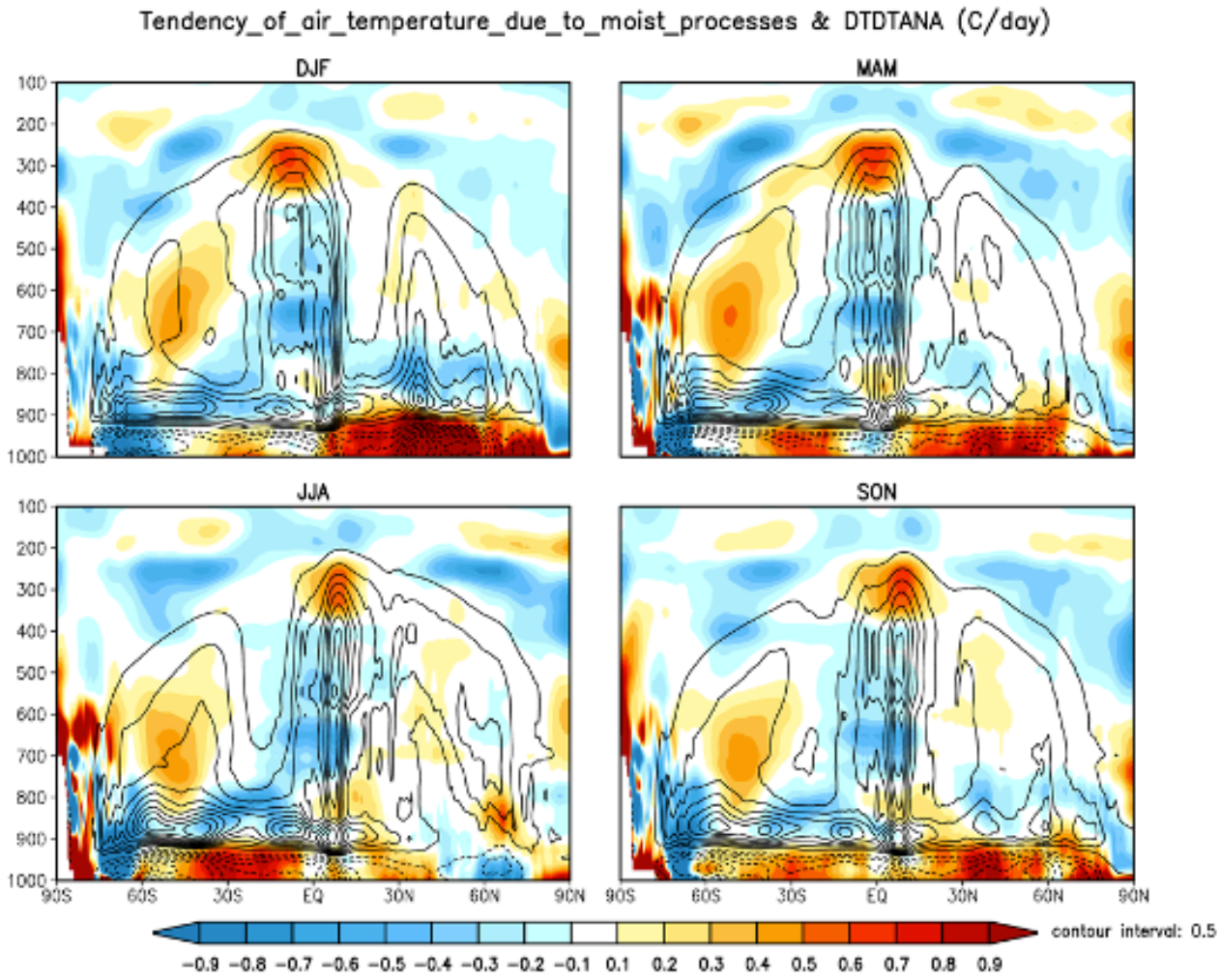

Figure 4a: The seasonal and zonal means of the temperature analysis increments (shaded, °C/day), with the tendency of the temperature due to moist processes from replay superimposed (contour intervals are "-4.5 -4.0 -3.5 -3.0 -2.5 -2.0 -1.5 -1.0 -.5 .5 1.0 1.5 2.0 2.5 3.0 3.5 4.0 4.5", negative values have dashed contours). The results are from the GEOS S2S V3 AOGCM replayed to MERRA-2 averaged over the time period 1981-2016. The vertical axis is pressure in mb.

While we of course do not have the true heating profiles available for comparison, we can compare the heating with what MERRA-2 produces (contours in Figure 4b). That heating looks remarkably similar to the heating from the replay (cf. contours in Figure 4a and 4b). This is remarkable since the free running model tends to produce reduced heating at the equator and enhanced heating off the equator, consistent with an unrealistic double ITCZ (see shading in Fig. 4b), especially during DJF

and MAM. This suggests that indeed, given more accurate input, the model's moist physics routines produce more accurate heating profiles. We note that MAM does show a double ITCZ in both the MERRA-2 and replay results. This is consistent with other observations (e.g., Liu and Xie 2002) which indicate that nature does tend to produce a double ITCZ in the Pacific during this season. We also see from Fig. 4b that, in the lower troposphere, the free running model (Base 9) tends to have too much heating near the top of the boundary layer (just below 900mb) and too little heating just above that during all seasons.

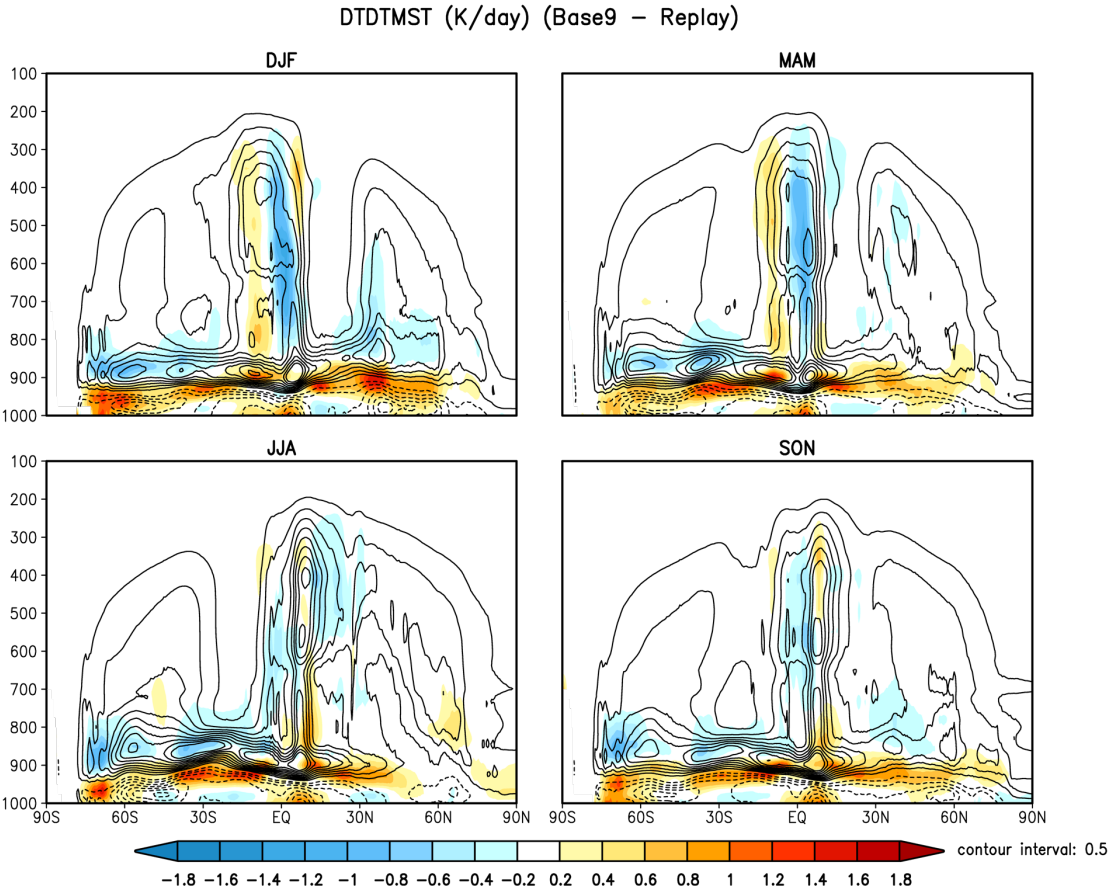

Figure 4b: The seasonal and zonal means of the temperature tendency due to moist processes from MERRA-2 (contoured, negative values have dashed contours), and the difference in the moist heating between Base 9 and replay (shaded). Units are (°C/day).

The zonal mean moisture increments (Fig. 5) act to dry the troposphere below about 900mb and moisten the atmosphere between about 950mb and 800mb during all seasons, with the largest amplitudes occurring in the subtropical regions of both hemispheres. In the tropical middle and upper troposphere, the increments show a tendency to moisten the atmosphere, counteracting the moisture removal from moist processes there. It is noteworthy that the largest reduction in

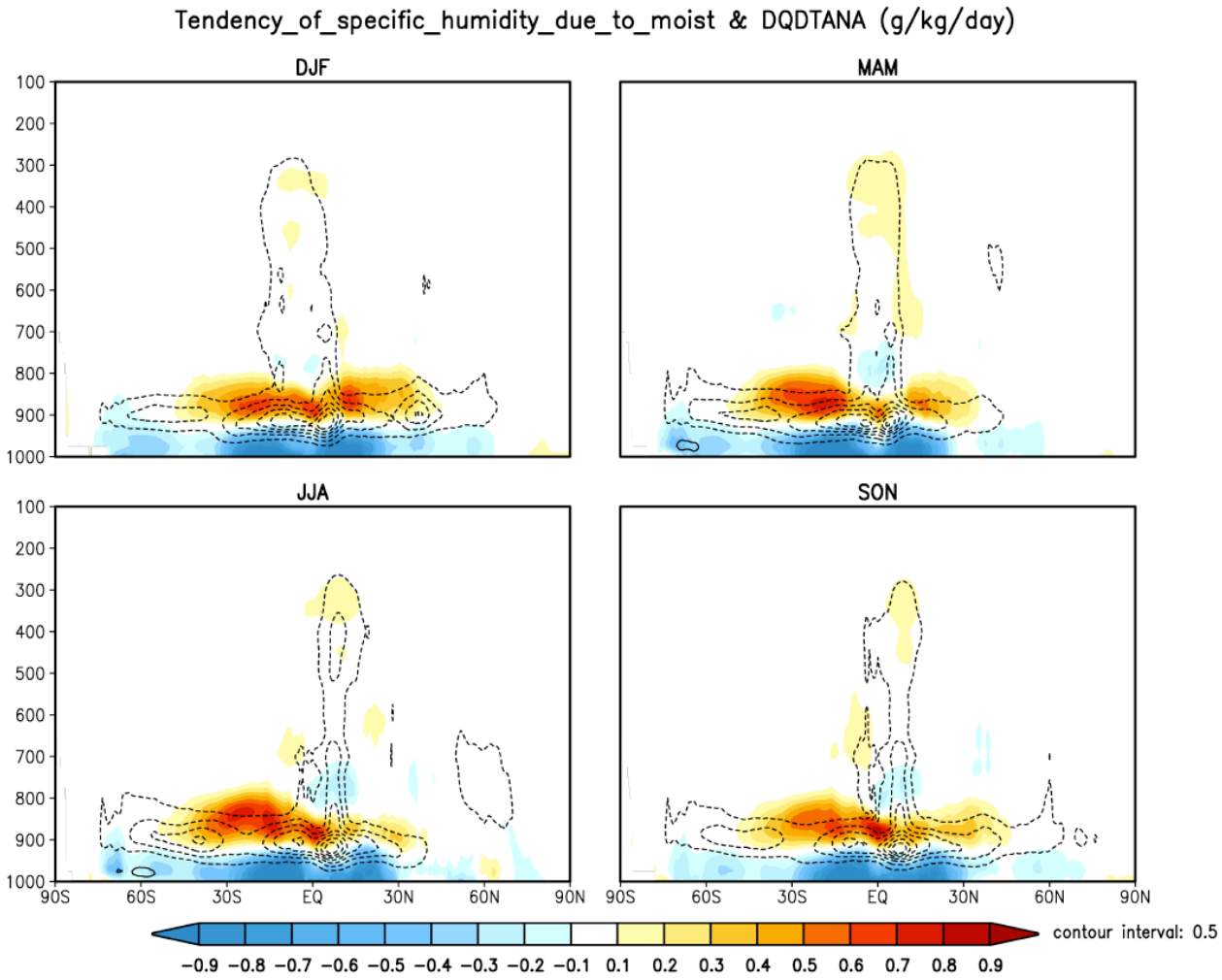

Figure 5: The seasonal and zonal means of the specific humidity analysis increments (shaded, g/kg/day), with the tendency of the specific humidity due to moist processes superimposed (contour interval is 0.5 g/kg/day, negative values have dashed contours). The results are from the GEOS S2S V3 AOGCM replayed to MERRA-2 averaged over the time period 1981-2016. The vertical axis is pressure in mb. Note that the outermost contour corresponds to -0.5.

atmospheric moisture from moist processes occurs around 900mb (at the node of the pattern of moisture increments). Figure 6, which again displays the zonal mean moisture increments but now with superimposed moistening from turbulent processes, shows that the moisture increments act to support the moistening from turbulent processes just above the boundary layer (above about 900mb),

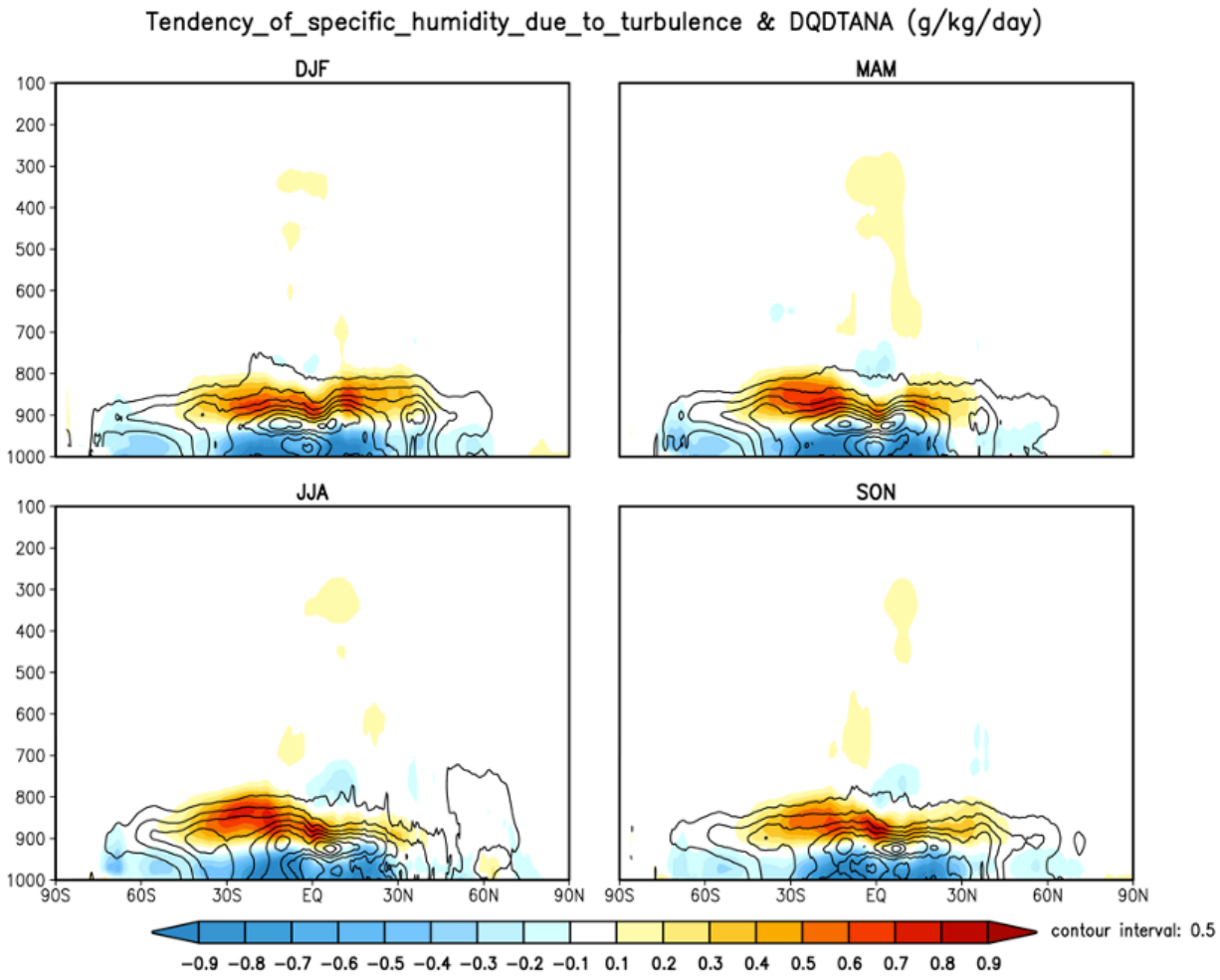

Figure 6: The seasonal and zonal means of the specific humidity analysis increments (shaded, g/kg/day), with the tendency of the specific humidity due to turbulence processes superimposed (contour interval is 0.5 g/kg/day, solid contours indicate positive values). The results are from the GEOS S2S V3 AOGCM replayed to MERRA-2 averaged over the time period 1981-2016. The vertical axis is pressure in mb.

while counteracting the moistening due to turbulent processes below about 950mb. As such, the increments are drying much of the boundary layer and moistening the region just above that, presumably compensating for excessive drying at the top of the boundary layer by the model's moist physics, and/or insufficient vertical transport of moisture in the boundary layer from turbulent processes. To aid in the interpretation of these results, we will look at the moisture increments at selected levels in the next section.

b) Seasonal means at selected levels

We next examine the global distribution of the seasonal mean analysis increments at selected levels, focusing in particular on those levels characterized in the previous section by large values in the zonal means.

Figure 7 shows the seasonal mean u-wind increments at the lowest model level (roughly 992mb or 60 meters above the surface). Here we see that the relatively strong positive zonal mean u-wind increments near the surface just north of 30°N for all but the summer months (Figure 2) reflect to a large extent the westerly flow acceleration over the Tibet region, while during DJF there is also a tendency to accelerate the westerlies just off the west coast of both Asia and North America. Also, the near-surface deceleration centered on 60°N that we saw in the zonal mean (Figure 2, again for all but the summer months) to a large extent reflects the westerly flow deceleration over Eurasia. Westerly flow deceleration also occurs over much of eastern North America while western North America (over the Rocky Mountains) is characterized by an acceleration of the westerly flow for all seasons. There is a general tendency for westerly acceleration (impeding the easterly flow) over the SH land masses during all seasons. There is also a tendency to accelerate the easterlies over the

Pacific and Atlantic Oceans. The above results suggest that there may be insufficient surface friction over continental regions, while the high topography may be acting too strongly to impede the flow.

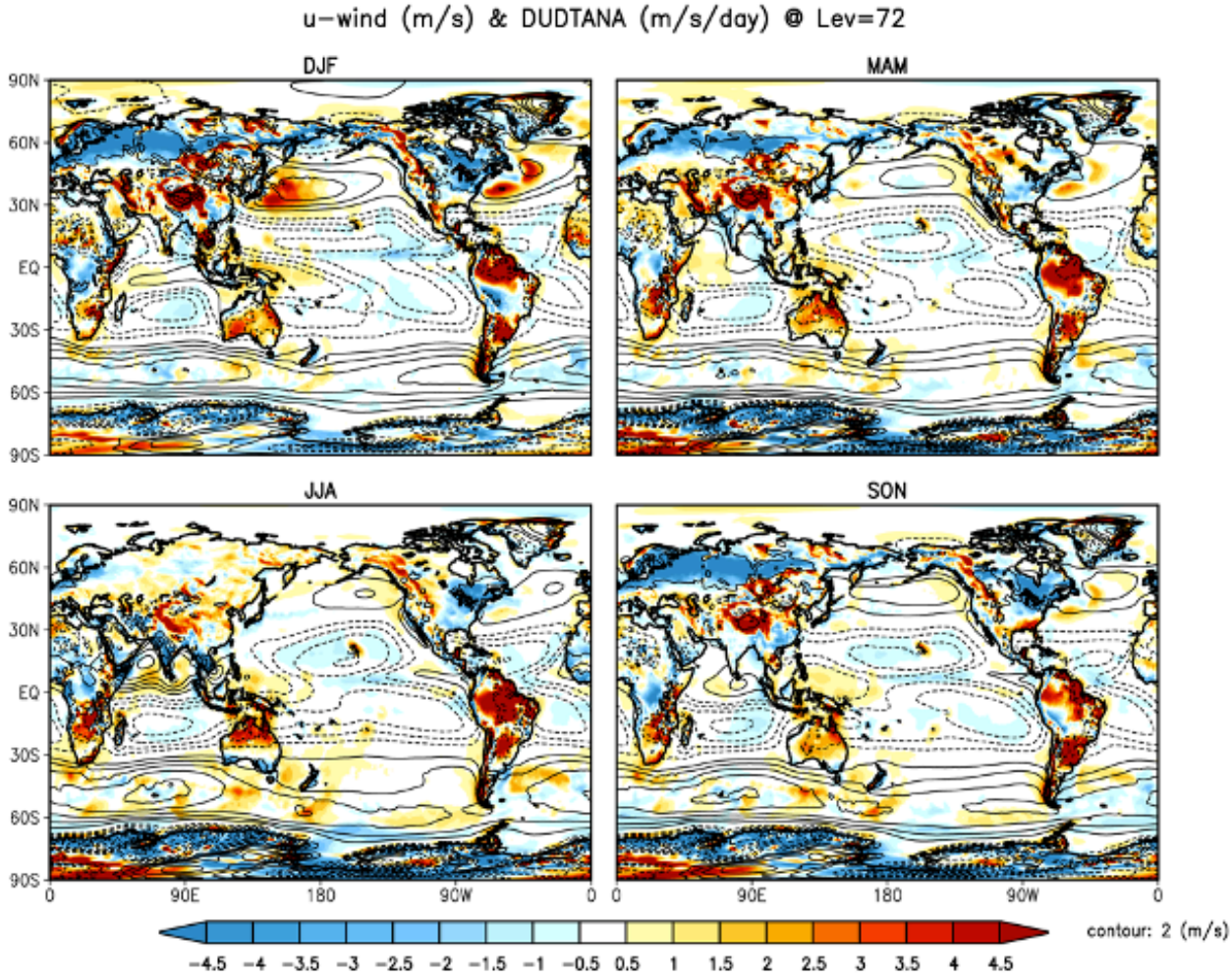

Figure 7: The model level 72 (approximately 992mb) seasonal means of the u-wind analysis increments (shaded, m/s/day) with the u-wind superimposed (contour intervals are 2 m/s with negative values indicated by dashed contours). The results are from the GEOS S2S V3 AOGCM replayed to MERRA-2 averaged over the time period 1981-2016.

Figure 8 shows the seasonal mean u-wind increments at 500mb – the level with the local positive maximum in the zonal mean u-wind increments (centered at 30°N) we saw in Fig. 2. This shows that the westerly acceleration during all seasons at those latitudes occurs primarily over Tibet and the North Pacific jet entrance region, as well as in the North Atlantic jet entrance region (over the

southeast U.S. and Gulf of Mexico). In the Southern Hemisphere, the increments act to enhance the split of the westerlies (centered over New Zealand) and to accelerate the westerlies south of 60°S (just north of Antarctica). In the tropics the increments generally produce an easterly acceleration.

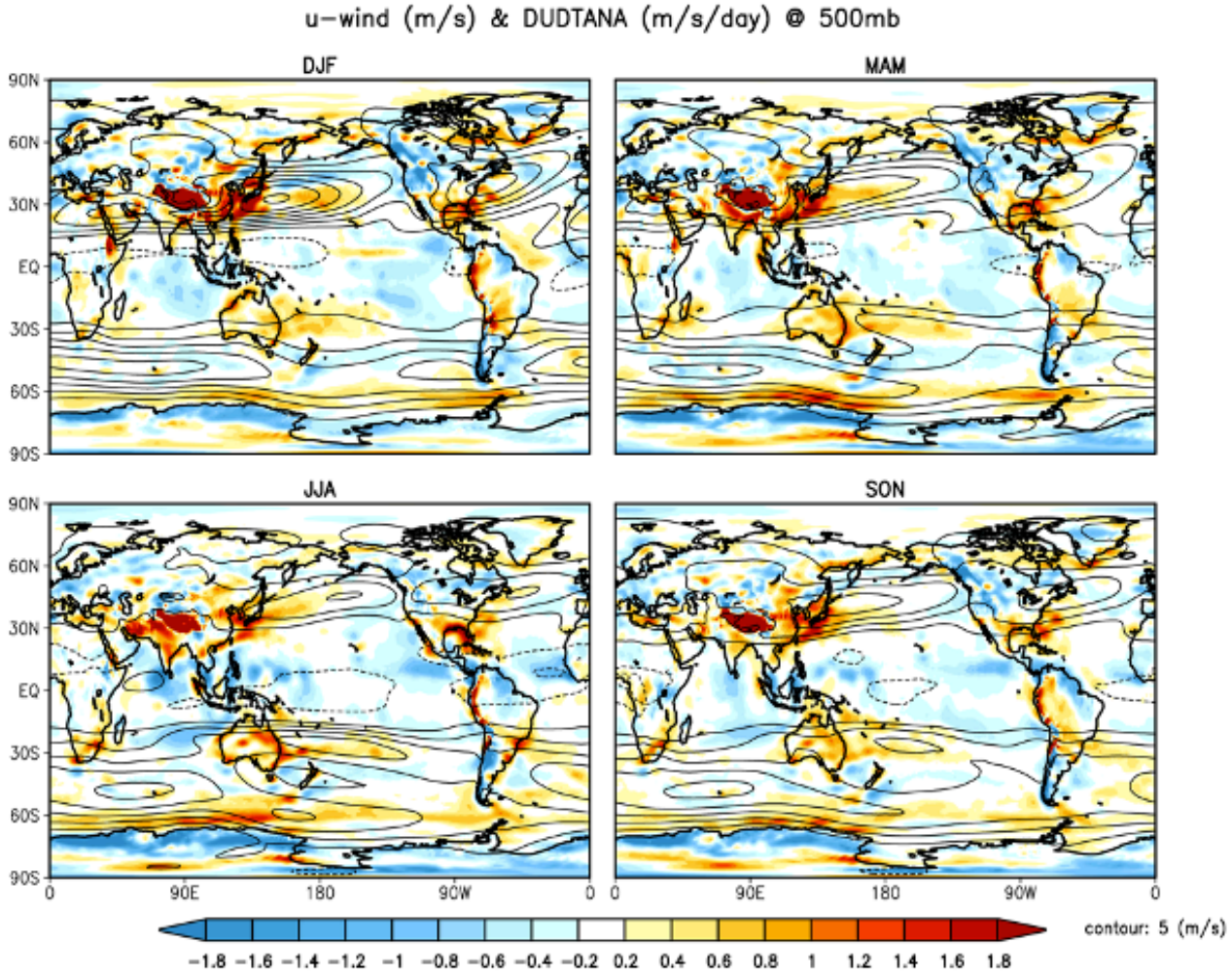

Figure 8: The 500mb seasonal means of the u-wind analysis increments (shaded, m/s/day) with the u-wind superimposed (contour intervals are 5 m/s with negative values indicated by dashed contours). The results are from the GEOS S2S V3 AOGCM replayed to MERRA-2 averaged over the time period 1981-2016.

Figure 9 shows the seasonal mean v-wind increments at the lowest model level. While spatially somewhat noisy, there are a few things that stand out. There is a general tendency for a southerly wind tendency throughout the Southern Hemisphere middle latitudes for all but DJF. There is also

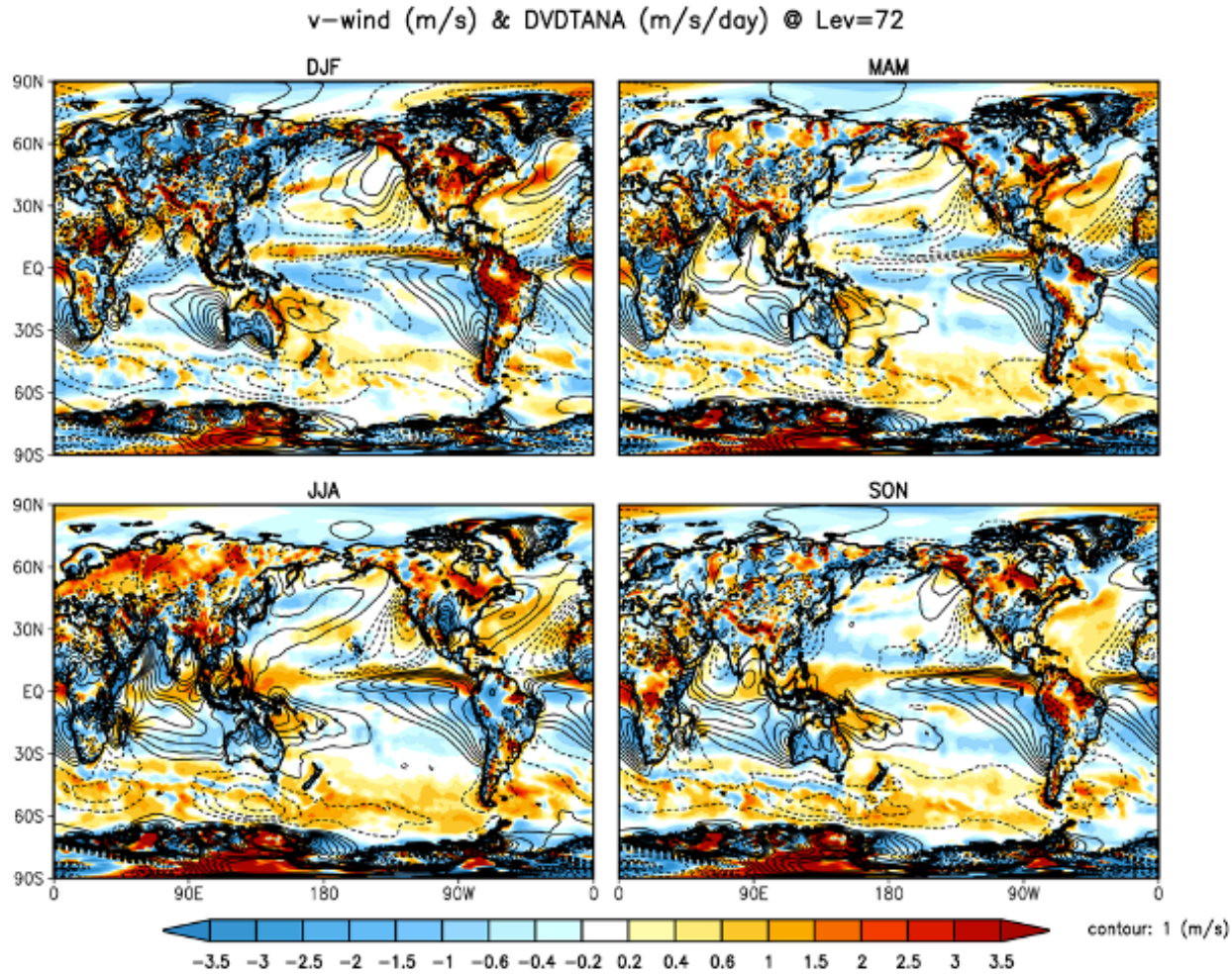

Figure 9: The model level 72 (approximately 992mb) seasonal means of the v-wind analysis increments (shaded, m/s/day) with the v-wind superimposed (contour intervals are 1 m/s with negative values indicated by dashed contours). The results are from the GEOS S2S V3 AOGCM replayed to MERRA-2 averaged over the time period 1981-2016.

a northerly wind tendency over much of the North Atlantic during all seasons. Over northern Eurasia, DJF is characterized by a northerly wind tendency, while JJA is characterized by a southerly wind tendency. Over the United States, JJA (and to a lesser extent MAM and SON) shows a northerly

wind tendency, indicating a deceleration of the Great Plains Low Level Jet (GPLLJ) by the increments. We will focus again on the GPLLJ later in this section.

In order to get a better sense of the combined impact of the low-level u and v wind increments over the oceans, we next plot the wind increments at the lowest model level as vector quantities (Figure 10). We superimpose on those vector fields the precipitation differences between the free-running

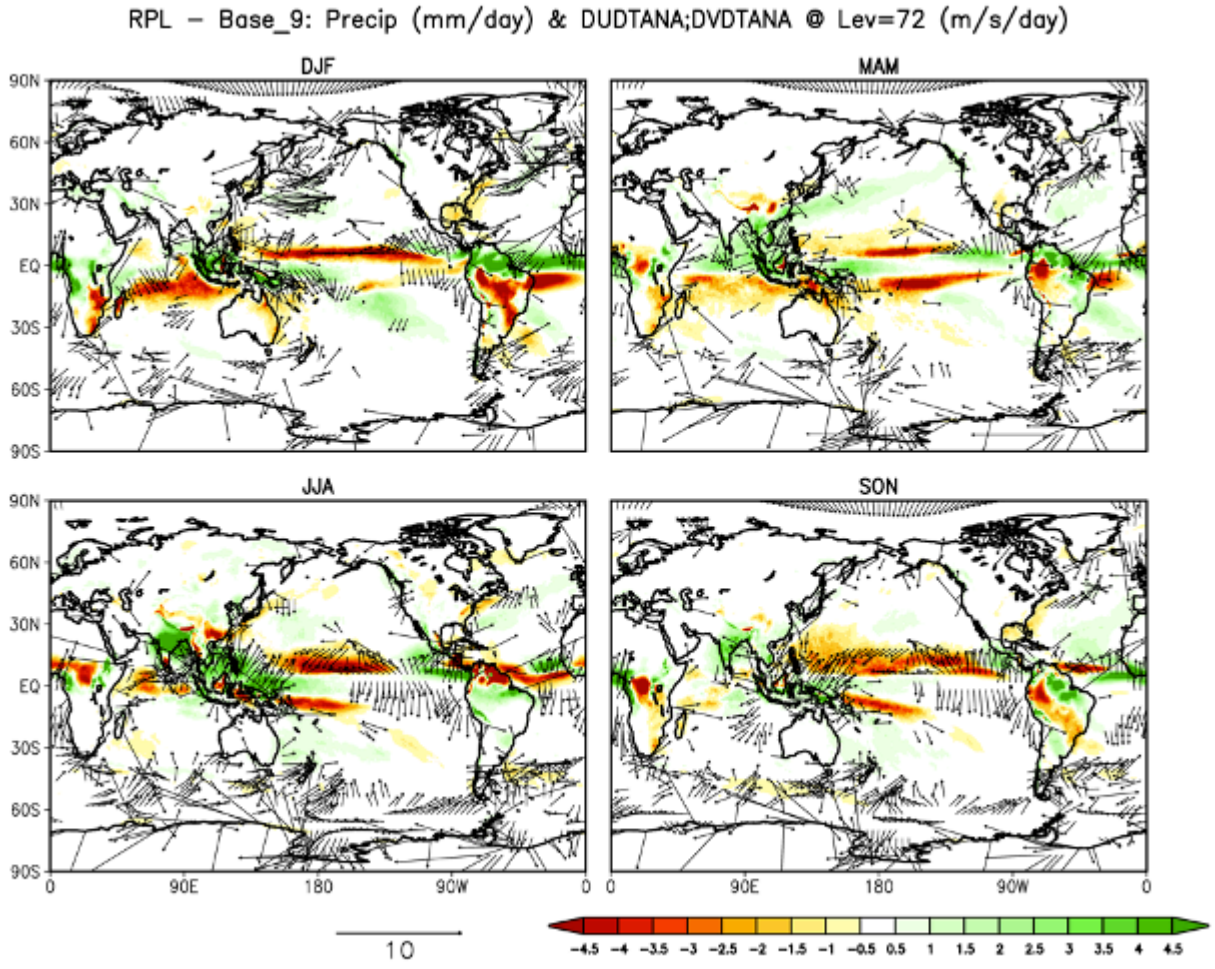

Figure 10: The model level 72 (approximately 992mb) seasonal means of the wind increments displayed as vectors (m/s/day), from the GEOS S2S V3 AOGCM replayed to MERRA-2 averaged over the time period 1981-2016. The shaded fields (mm/day) are the differences between the precipitation from the replay run and that of the free running model (without replay, internal designation is "Base 9", see text).

model (Base 9) and the replay run, with the hope of gaining some insight into how the wind increments may have played a role in correcting some of the long-standing precipitation biases of the model (excessive tropical precipitation, a split ITCZ, and insufficient Indian summer monsoon precipitation, see the Appendix). Focusing on the tropical Pacific, we see that the wind increments act to enhance low level divergence (suppress convergence) over much of the eastern equatorial Pacific during all seasons though especially during JJA and SON. During DJF the increments also act to enhance the easterlies just north of the equator, coinciding with the region where the replay run produces substantially less precipitation than the base 9 run (possibly by enhancing the cold water upwelling there). The increments are divergent over the maritime continent south of the equator during JJA, presumably helping to reduce the precipitation compared to base 9 in that region.

Figure 11 shows that things are quite different at model level 63 (roughly 857 mb), with the wind increments in the tropical Pacific indicating a tendency for convergence especially in the western Pacific, while in the upper troposphere (250mb, Fig. 12) the wind increments act to increase divergence over much of the tropical Pacific. As such, these results suggest that the source of the excessive tropical Pacific precipitation likely lies in the boundary layer formulation where the increments are acting to suppress convergence. Above that, the increments are actually acting to enhance the upward motion (producing anomalous low-level convergence and upper-level divergence) and presumably acting to increase the precipitation.

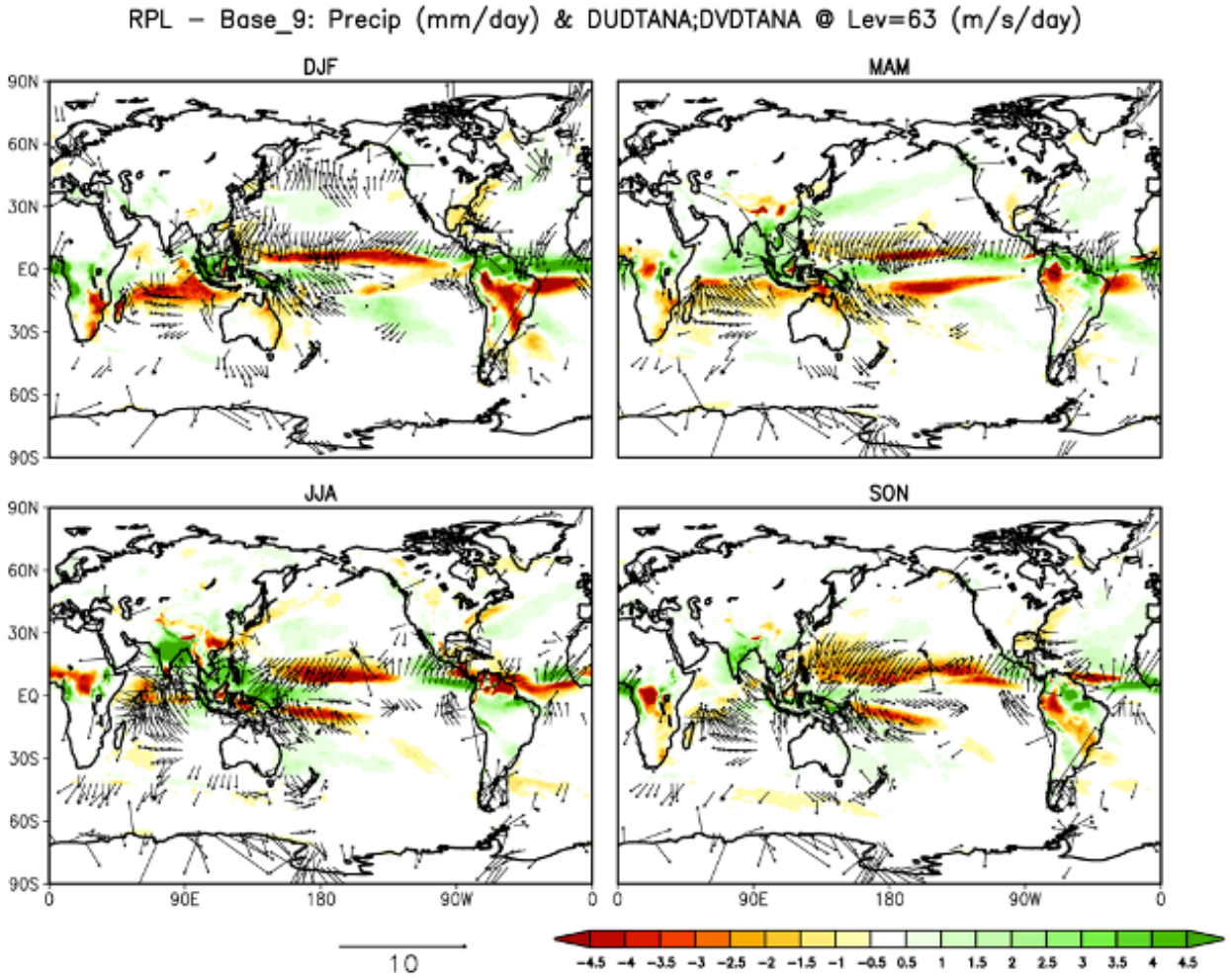

Figure 11: Same as Fig. 10, but at model level 63 (approximately 857mb).

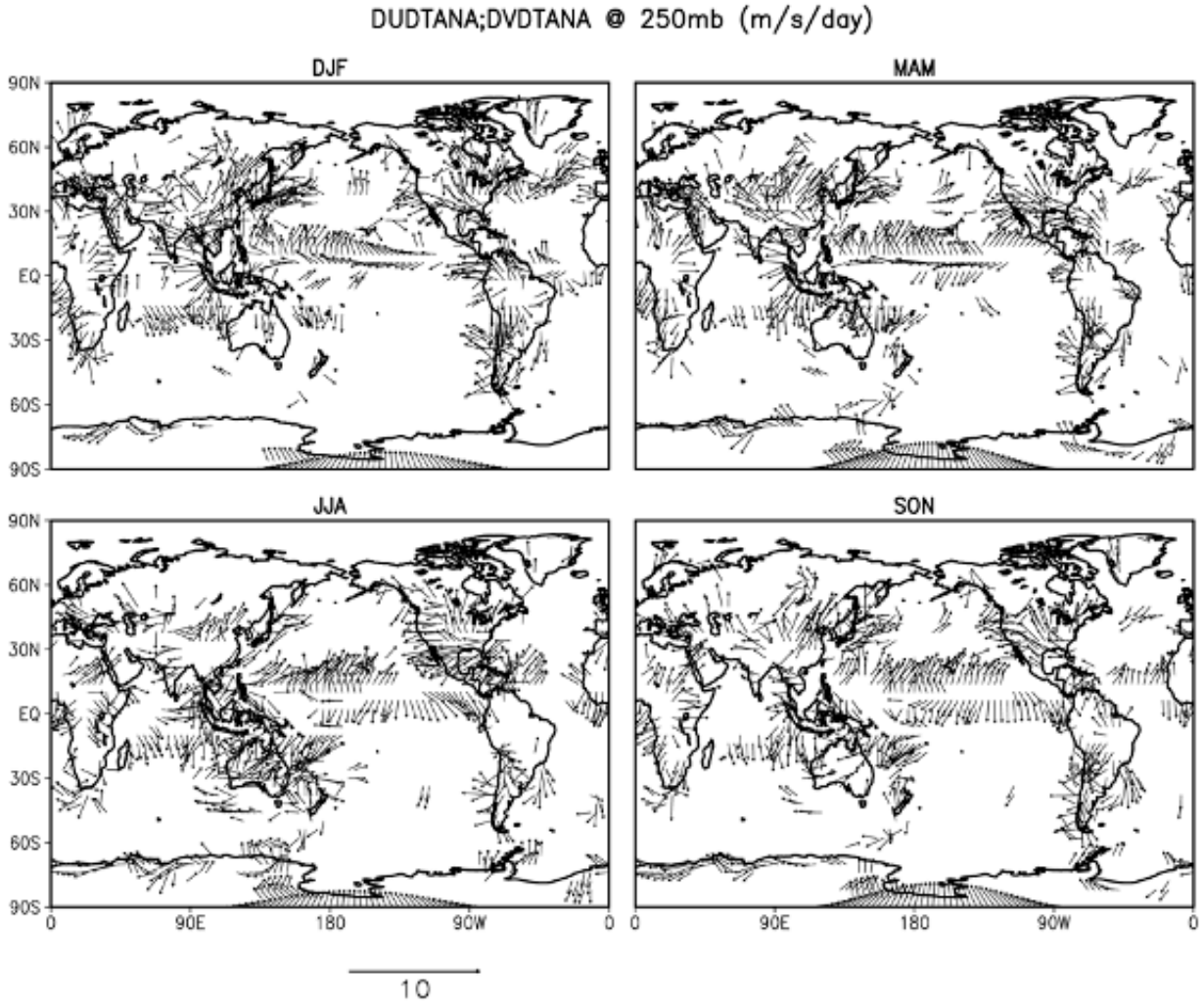

Figure 12: Same as Fig. 10, but at 250mb and without the precipitation differences.

We next turn to the spatial distribution of the temperature increments (Figs 13 - 15) and moisture increments (Figs 16 and 17). In these figures we plot the seasonal mean increments normalized by the standard deviation of the monthly means (1/dispersion) as a way of highlighting those regions where the mean values are statistically the most robust. Figure 13 shows that the zonal mean boundary layer warming that we saw in Fig. 4a during all seasons is concentrated over the subtropical oceans. This is presumably compensating for insufficient heating (too strong cooling) from the

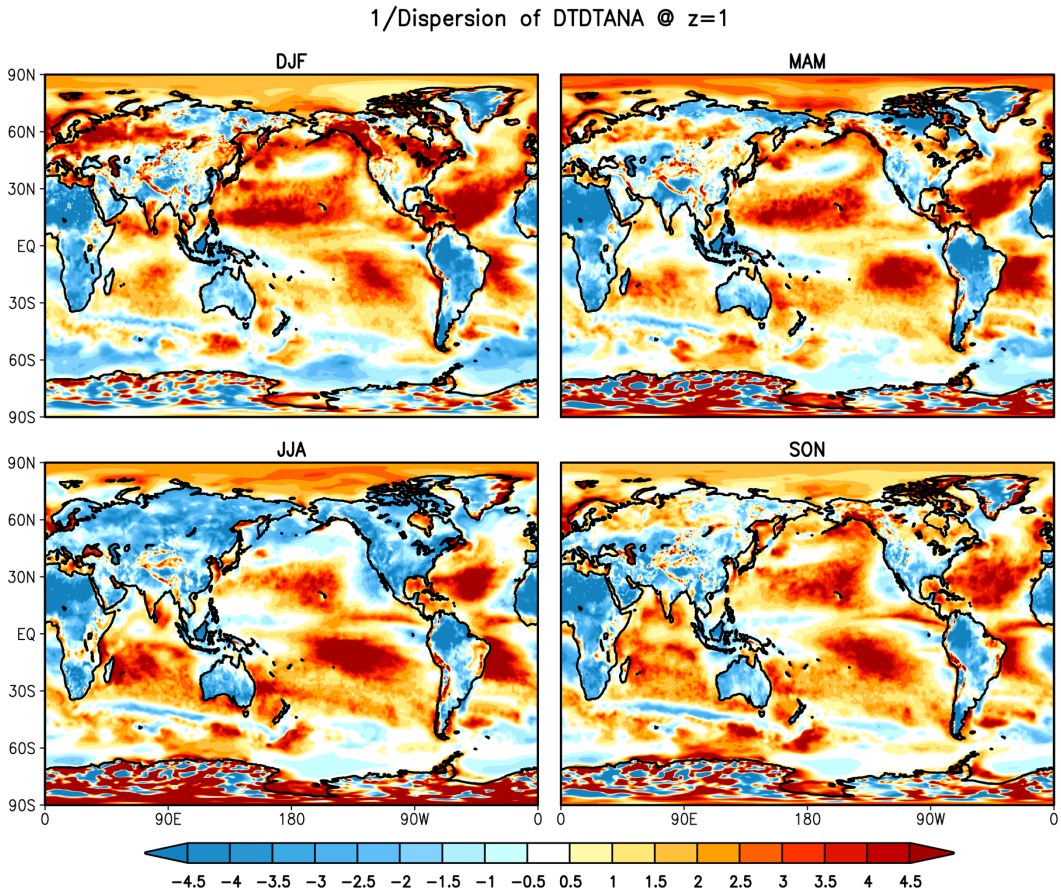

Figure 13: The model level 72 (approximately 992mb) seasonal mean temperature increments normalized by the standard deviation of the monthly means (1/dispersion). The results are from the GEOS S2S V3 AOGCM replayed to MERRA-2 averaged over the time period 1981-2016. Units are dimensionless.

model's moist boundary layer processes over those regions. During JJA, the near surface increments act to cool the NH land areas, whereas during DJF the increments act to warm much of the NH middle and high latitude land areas. Low level cooling tendencies also occurs over Africa, Australia and South America during all seasons.

The temperature increments at 650mb (Fig. 14) are quite different from those near the surface, showing maximum warming in the storm tracks of both hemispheres during all seasons (recall the relatively large positive zonal mean values in the SH middle latitudes, Fig. 4a). Here we see that the

temperature increments are also positive in the NH storm tracks at 650mb (in both the North Pacific and North Atlantic Oceans) though these do not show up in the zonal means (Fig. 4a) due to the negative temperature increments over the intervening land areas. This is likely compensating for the free-running model's insufficient transient eddy variability, and in particular for the insufficient heating associated with biases in the vertical transient eddy heat fluxes ($\overline{\omega' T'}$, not shown). The increments are negative throughout the tropics, with the largest amplitudes roughly coinciding with the regions of maximum precipitation.

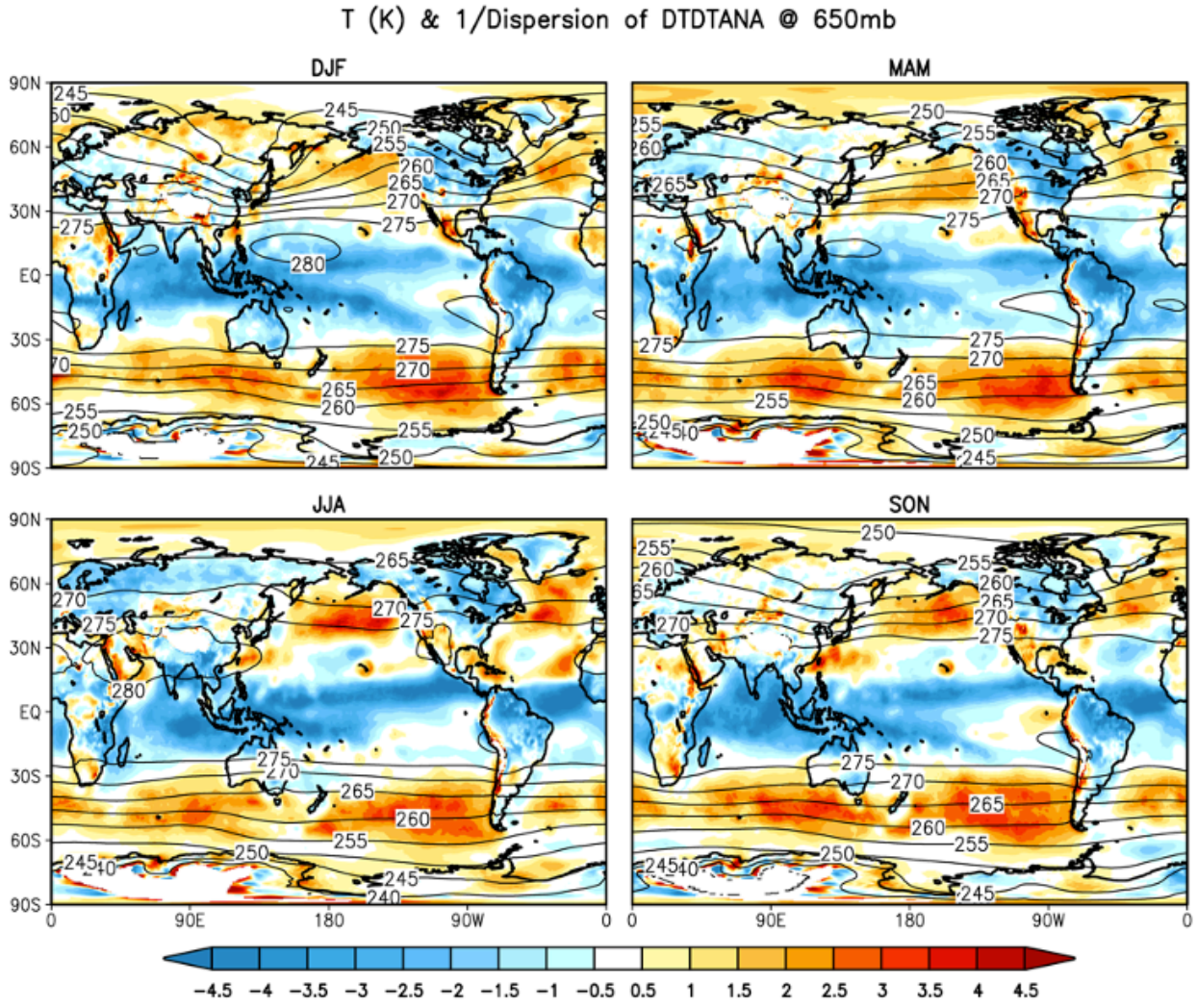

Figure 14: Same as Fig. 13, but at 650mb. Contours show the 650mb temperature.

At 250mb (Fig. 15) we see that the zonal mean upper tropospheric warming (Fig. 4a) is the result of warming tendencies that occur throughout the tropics. The warming is to a large extent spatially tied to the locations of the maxima in tropical precipitation and is likely compensating for insufficient deep convective heating in those regions. Some of the largest warming tendencies occur over northern South America during DJF and MAM. Outside of the tropics the increments act to cool the atmosphere at 250mb during all seasons, especially in the SH storm tracks during MAM and over much of the NH land areas during JJA.

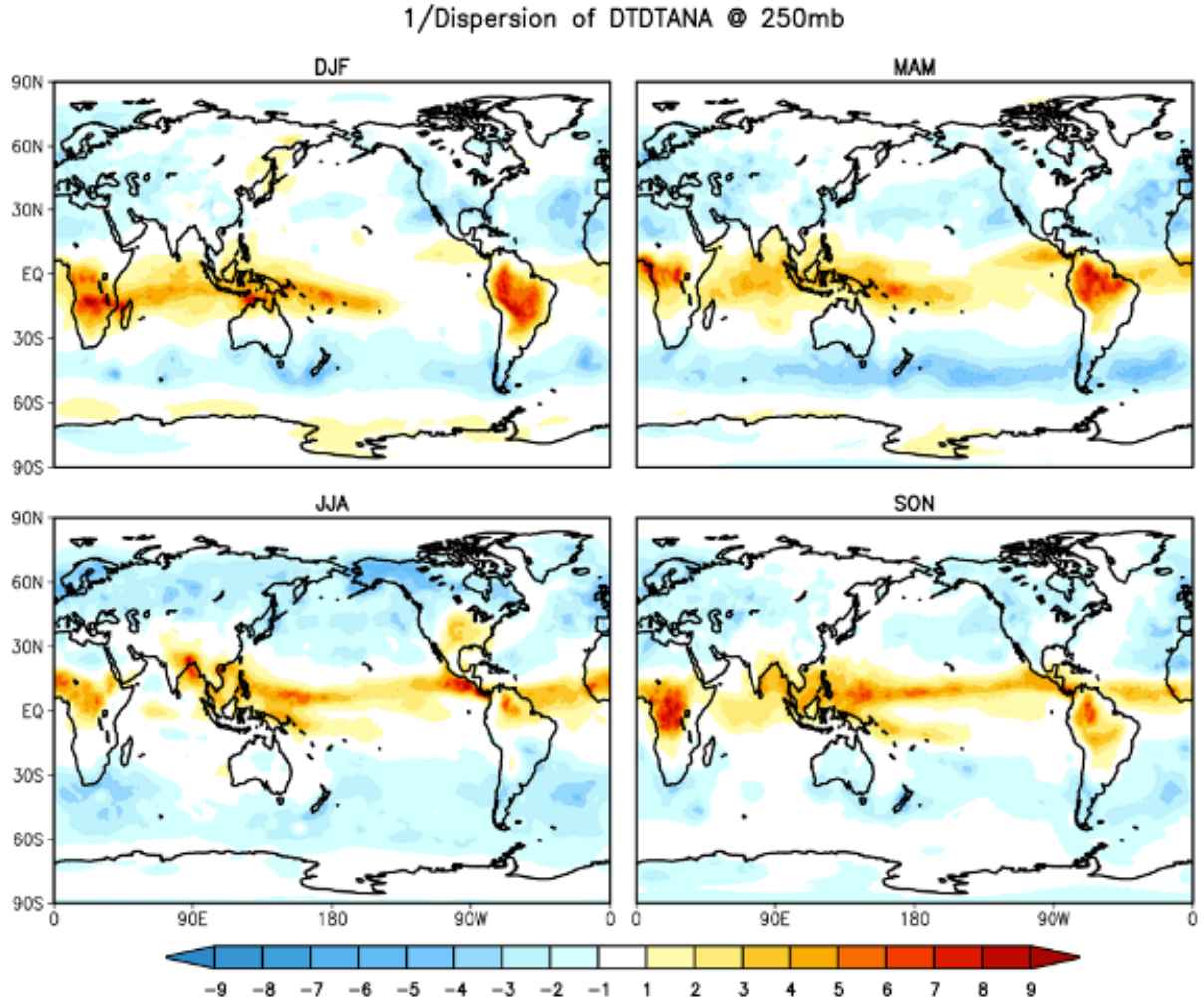

Figure 15: Same as Fig. 13, but at 250mb.

Figure 16 shows that the moisture increments are acting to dry the lowest level of the model almost everywhere over the oceans during all seasons. Some moistening occurs during all seasons over northern South America, western North America, tropical Africa and the maritime continent. Moistening also occurs over northern Eurasia during JJA and MAM and over Antarctica during MAM and JJA. As expected from the zonal mean results (Fig. 5), things are quite different at model level 63 (approx. 857mb), with the increments acting to moisten the atmosphere almost everywhere over the subtropical oceans during all seasons (Fig. 17). Over land, the increments show a general tendency to dry the atmosphere, with the main exception being over Eurasia during DJF where there

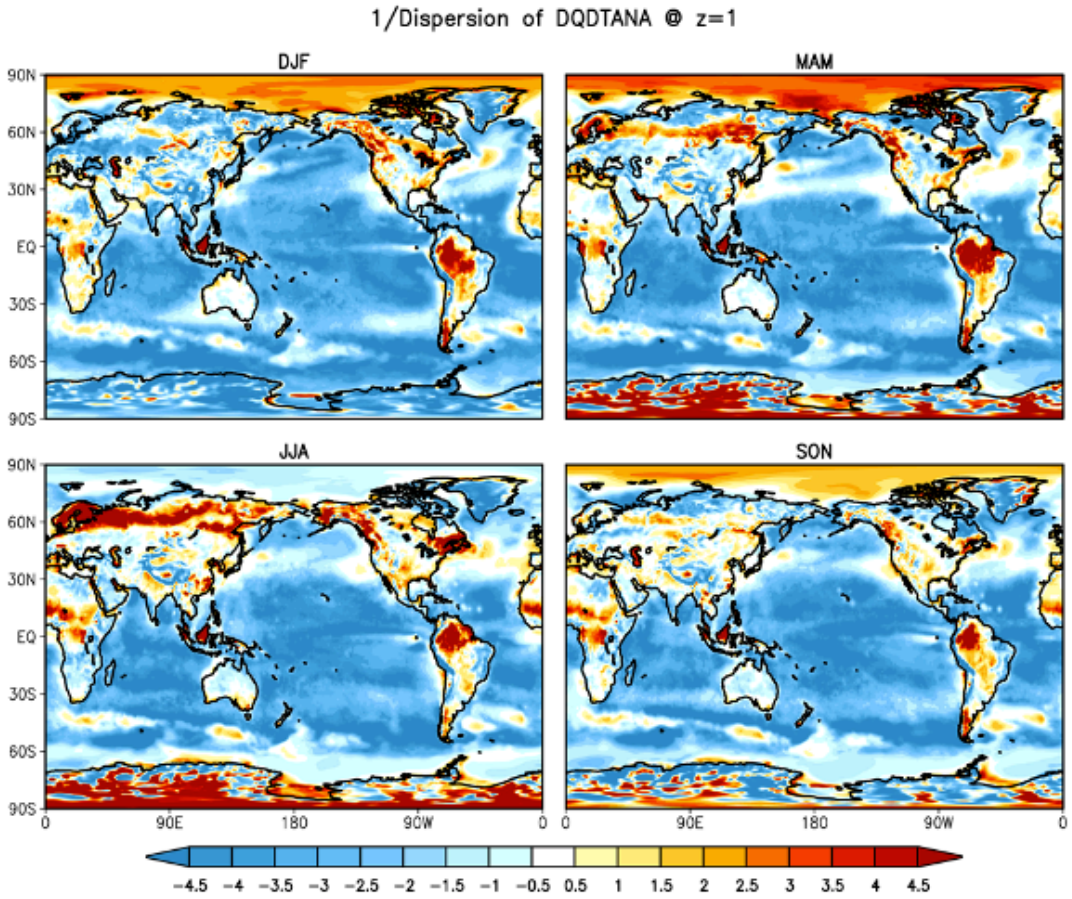

Figure 16: The model level 72 (approximately 992mb) seasonal mean specific humidity increments normalized by the standard deviation of the monthly means (1/dispersion). The results are from the GEOS S2S V3 AOGCM replayed to MERRA-2 averaged over the time period 1981-2016. Units are dimensionless.

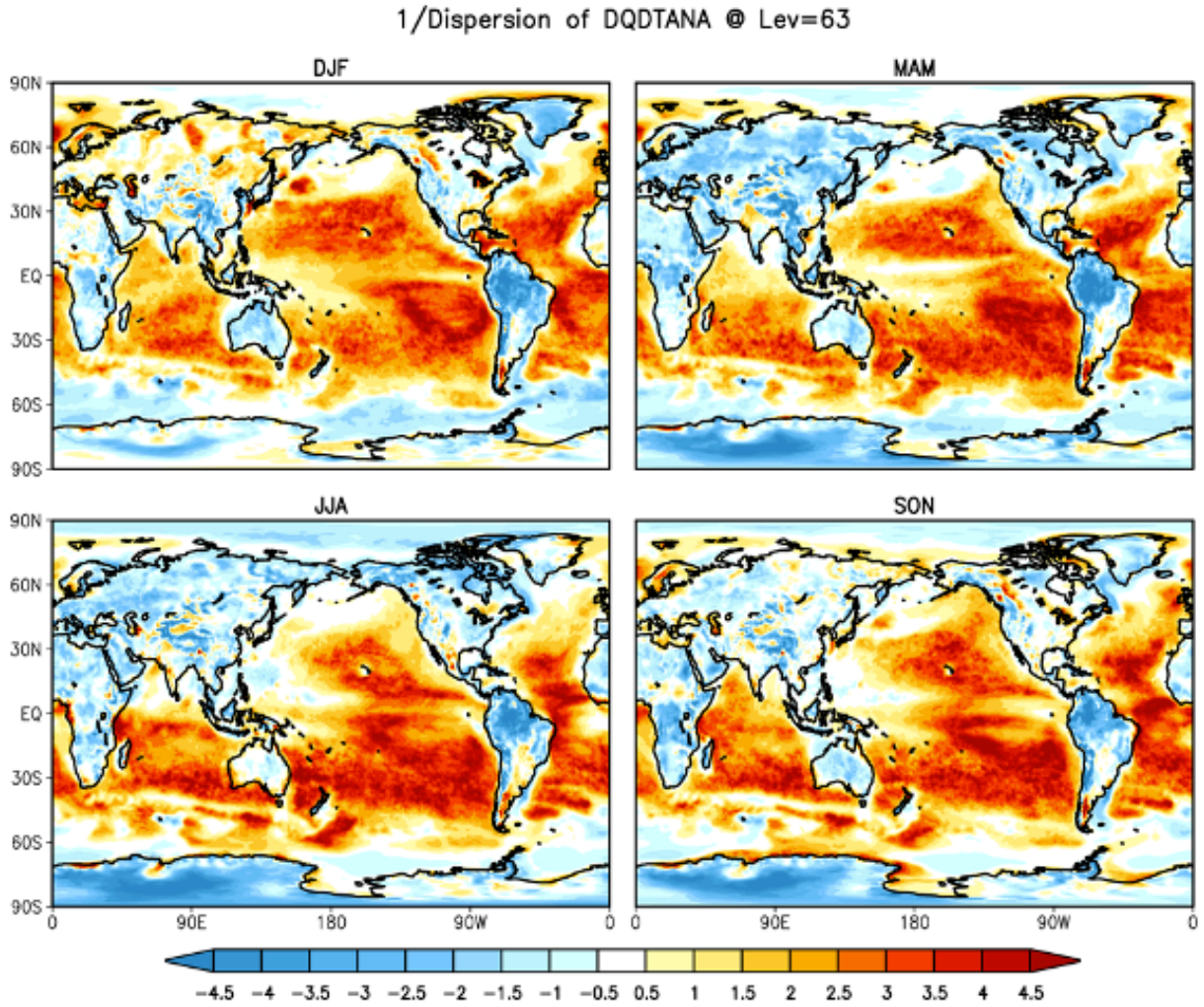

Figure 17: Same as Fig. 16, but at model level 63 (approximately 857mb).

is some tendency to moisten the atmosphere. These results highlight the rather abrupt change in the vertical structure of the moisture increments over the oceans, characterized by drying in the boundary layer and moistening just above that (see Fig. 5). This again presumably compensates for deficiencies in the model's boundary layer processes over the oceans that result in too little moisture being transported vertically out of the boundary layer. We note that an abrupt change in the vertical also occurs over northern South America, though in this case the increments act to moisten the boundary layer and produce drying just above that.

We next turn to an assessment of the diurnal cycle of the increments, focusing on DJF and JJA.

c) The mean diurnal cycle

We focus here on the lowest level of the model where we expect the diurnal cycle of the atmosphere (and the increments) to be the largest. In order to more easily identify the diurnal cycle, we present in Figures 18 -21 the diurnal cycle *anomalies* of u, v, T and q computed for each time of the day (00z, 06Z, 12Z, 18Z) as the difference from the time mean fields (the single average of the four instantaneous 00Z, 06Z, 12Z, 18Z fields). We should note that, by that definition, the anomalies for the four times of the day add to zero.

Figure 18 shows the diurnal cycle anomalies for the temperature increments at the lowest model level for DJF. The anomalies are generally weak over the oceans with however somewhat larger (0.5°/day – 1 °/day) spatially coherent positive anomalies over the North Pacific at 00Z. The largest anomalies clearly occur over land, where there is an overall tendency for positive anomalies at 12Z and negative anomalies at 06Z. The main exceptions are the very large positive anomalies over southeast Asia at 06Z, balanced by negative anomalies during the other times of the day. Over Africa, relatively large positive anomalies occur at 12Z. Over northern Eurasia, the relatively large positive anomalies at 12Z are largely balanced by negative anomalies at 18Z. Also, the large positive anomalies that occur along the coastal and southern regions of South America at 18Z are largely balanced by negative anomalies in those regions at 06Z. Over Australia, positive anomalies at 00Z and 06Z are balanced by negative anomalies at the other times of the day. We note that some of the timing of the largest positive values of the increments may in part reflect the position of the sun, and so an analysis based on the local time of day might provide more intuitive results, though we do not pursue that approach here.

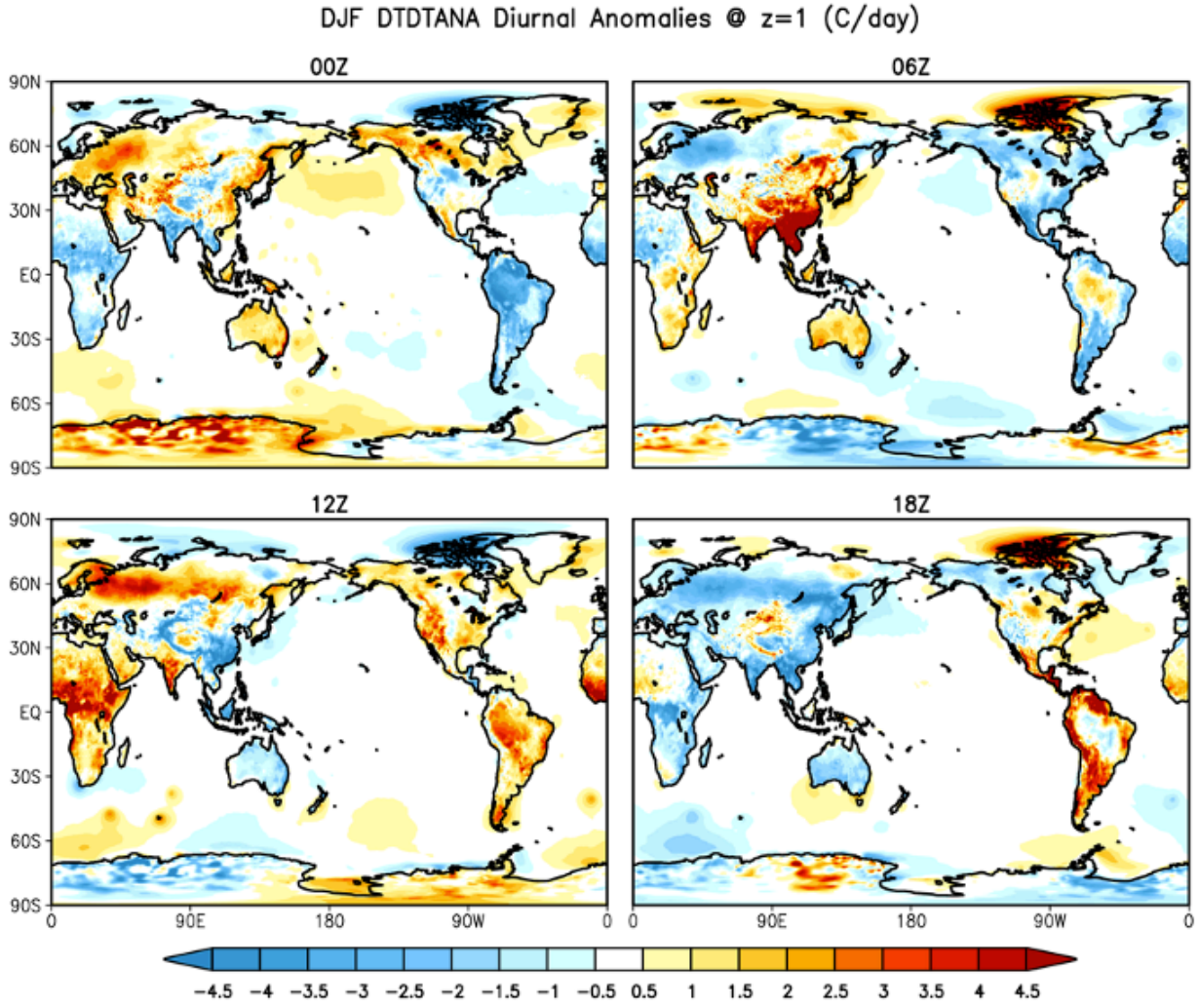

Figure 18: The model level 72 (approximately 992mb) DJF mean temperature increment anomalies (°C/day) for 00z, 06Z, 12Z and 18Z. The results are from the GEOS S2S V3 AOGCM replayed to MERRA-2 averaged over the time period 1981-2016.

Figure 19 shows that the diurnal cycle anomalies for the temperature increments at the lowest model level for JJA are overall similar to those for DJF (Fig. 18). Some notable differences are the spatially more extensive negative anomalies over Eurasia during 18Z and, over North America, the more pronounced negative anomalies during 06Z and positive anomalies during 18Z. There are also somewhat greater positive anomalies over the North Pacific Ocean during 00Z (cf. Figs. 18 and 19) that are primarily balanced by negative anomalies during 12Z and 06Z.

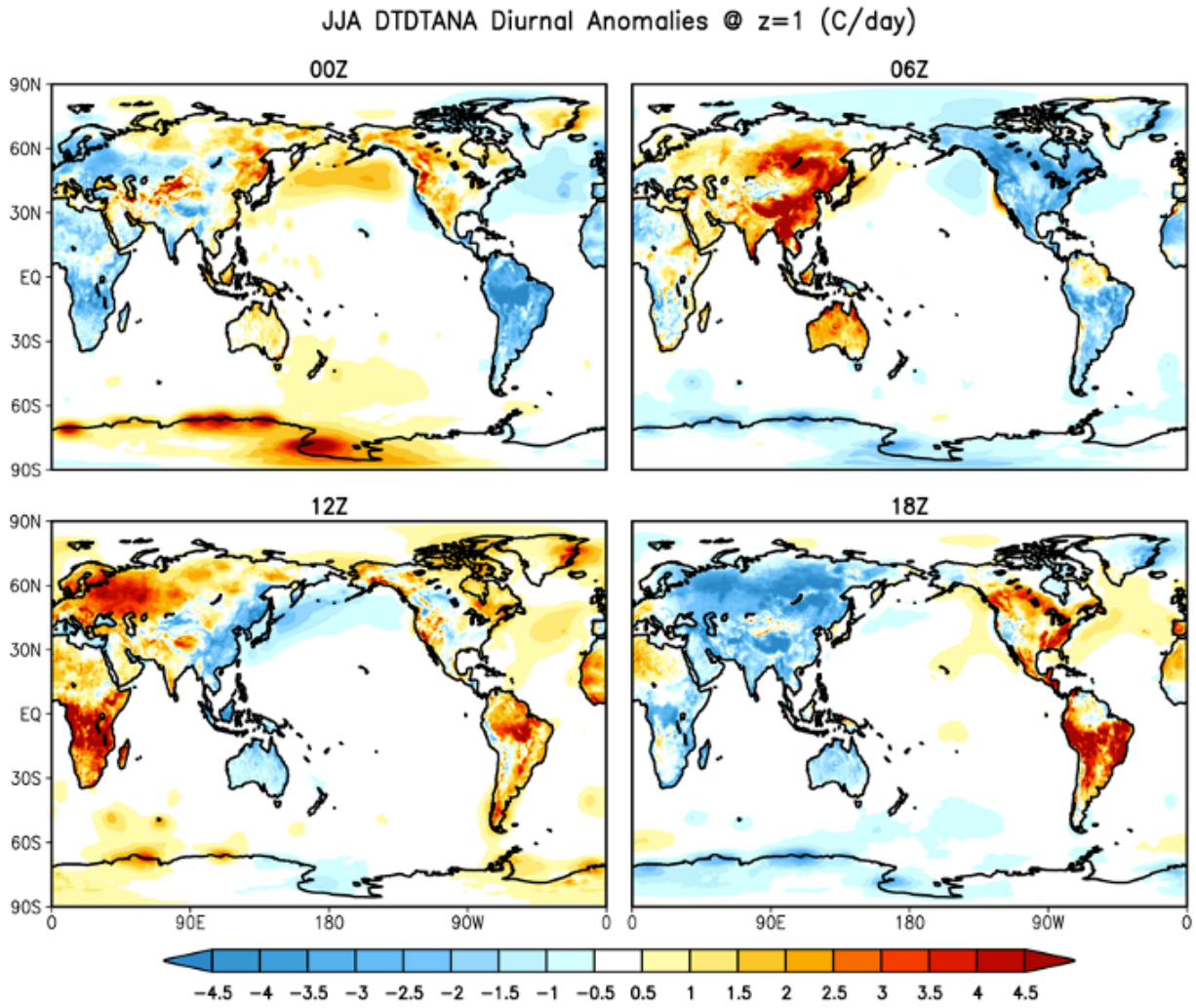

Figure 19: Same as Fig. 18, but for JJA.

Figure 20 shows the diurnal cycle anomalies for the moisture increments at the lowest model level for DJF. Most striking are the large positive values over northern South America during 00Z, which are balanced by negative anomalies during 06Z and 12Z. Tropical Africa has large positive values during 18Z that are balanced by negative anomalies during 00Z and 06Z. The central tropical North Pacific has a large region of positive anomalies just north of the equator during 12Z that are largely balanced by negative anomalies during 18Z. Southeast Asia tends to have positive increments during 00Z and 18Z, with negative increments during the other times of the day.

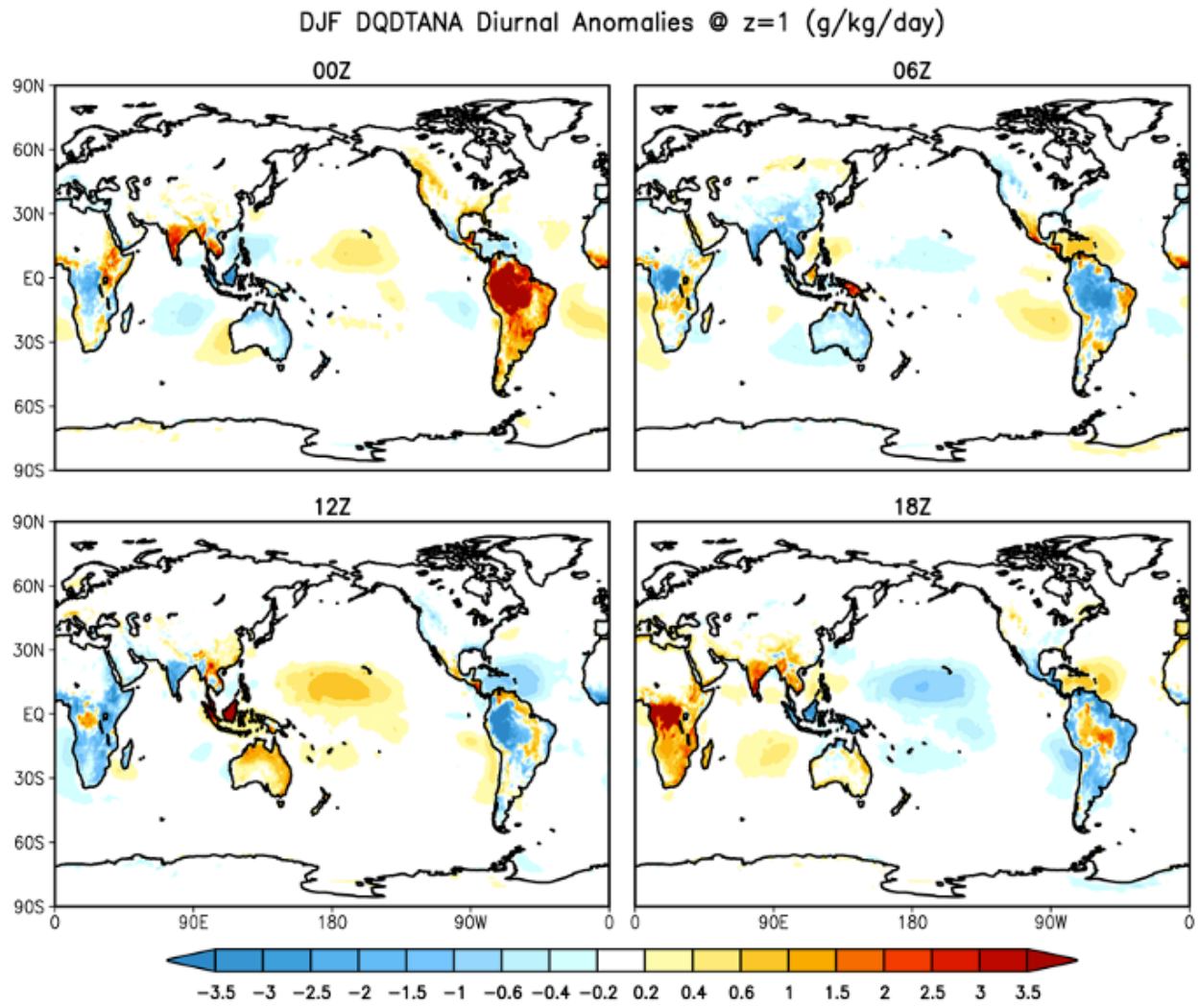

Figure 20: The model level 72 (approximately 992mb) DJF mean specific humidity increment anomalies (g/kg/day) for 00z, 06Z, 12Z and 18Z. The results are from the GEOS S2S V3 AOGCM replayed to MERRA-2 averaged over the time period 1981-2016.

Figure 21 shows that the diurnal cycle anomalies for the moisture increments at the lowest model level for JJA are substantially different from those for DJF (Fig. 20). Much of the Northern (summer) Hemisphere land now exhibits a substantial diurnal cycle in the increments (compared with essentially no diurnal cycle during DJF). Over North America, negative anomalies occur in the western half and positive anomalies occur in the eastern half during 00Z, with the reverse during

06Z. The diurnal anomalies over Eurasia show a somewhat complicated structure, with negative anomalies to the north and positive anomalies to the south during 00Z, and the reverse during 12Z. 06Z and 18Z also show a tendency for opposite anomalies over Eurasia. Over the Pacific Ocean, a pair of localized anomalies straddle the equator just east of the dateline during 00Z and 12Z, with corresponding negative anomalies during 06Z and 18Z.

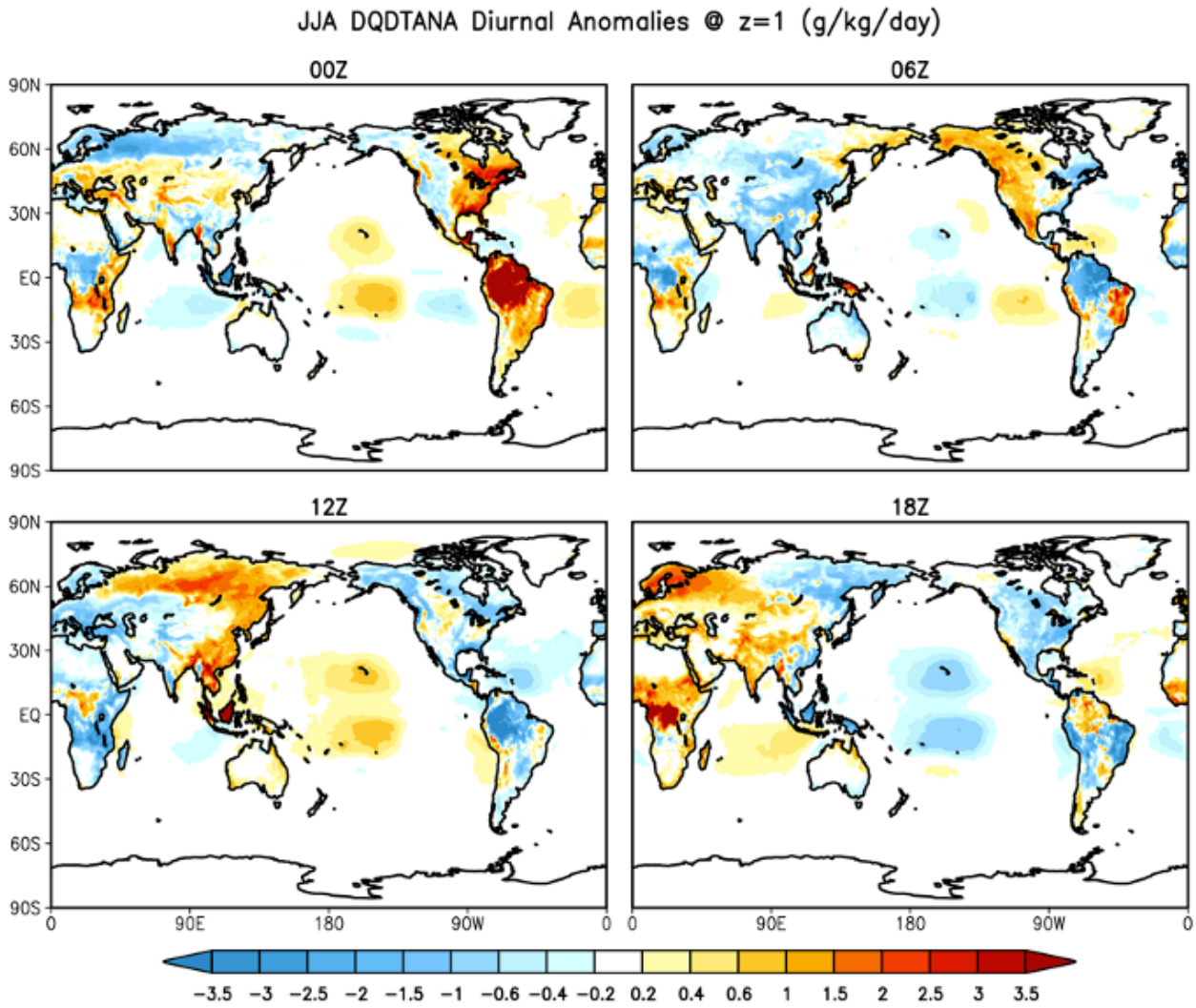

Figure 21: Same as Fig. 20, but for JJA.

The diurnal cycle anomalies of the winds over the oceans at the lowest model level are rather noisy, with no apparent large scale coherent structure (not shown). Over land, we are particularly interested in assessing the diurnal cycle of the JJA wind increments over the United States and their impacts on the nocturnal Great Plains low level jet (GPLLJ). Figure 22 shows cross sections at 35°N (the latitude close to the center of the largest frequency of northerly flow associated with the GPLLJ, e.g., Helfand and Schubert 1995) of the diurnal cycle of the v-wind increments, with the

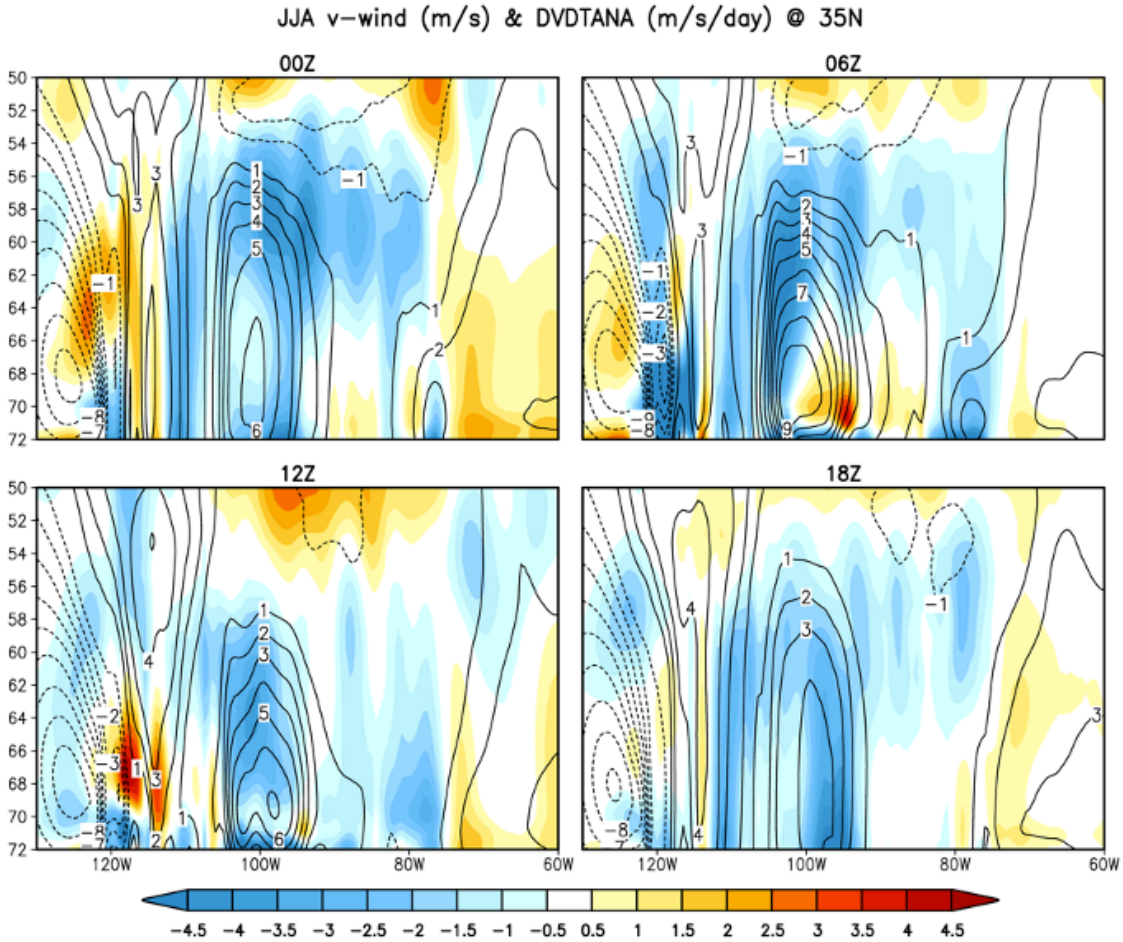

Figure 22: Vertical cross sections (130°W to 60°W, from about 992mb to 500mb) at 35°N of the JJA v-wind increments (shaded, m/s/day) and v-wind (contoured with dashed contours indicating negative values, m/s) for a) 00z, b) 06Z, c) 12Z and d) 18Z. The results are from the GEOS S2S V3 AOGCM replayed to MERRA-2 averaged over the time period 1981-2016.

climatological v-winds (contours) from replay superimposed for each time of day. Here we show the total diurnal increments (rather than the anomalies) to more clearly show the full impact they have on the GPLLJ. The GPLLJ (centered at about 100°W) is quite evident in the v-winds, which are strongest (> 9 m/sec) during the middle of the night (06Z), peaking at about 960mb (L=69) in the vertical. The increments are for the most part negative within the domain of the GPLLJ during all times of the day, indicating that the simulated jet of the free-running model is likely too strong. This is verified in Fig. 23, which shows that the differences between the GPLLJ in the free running model

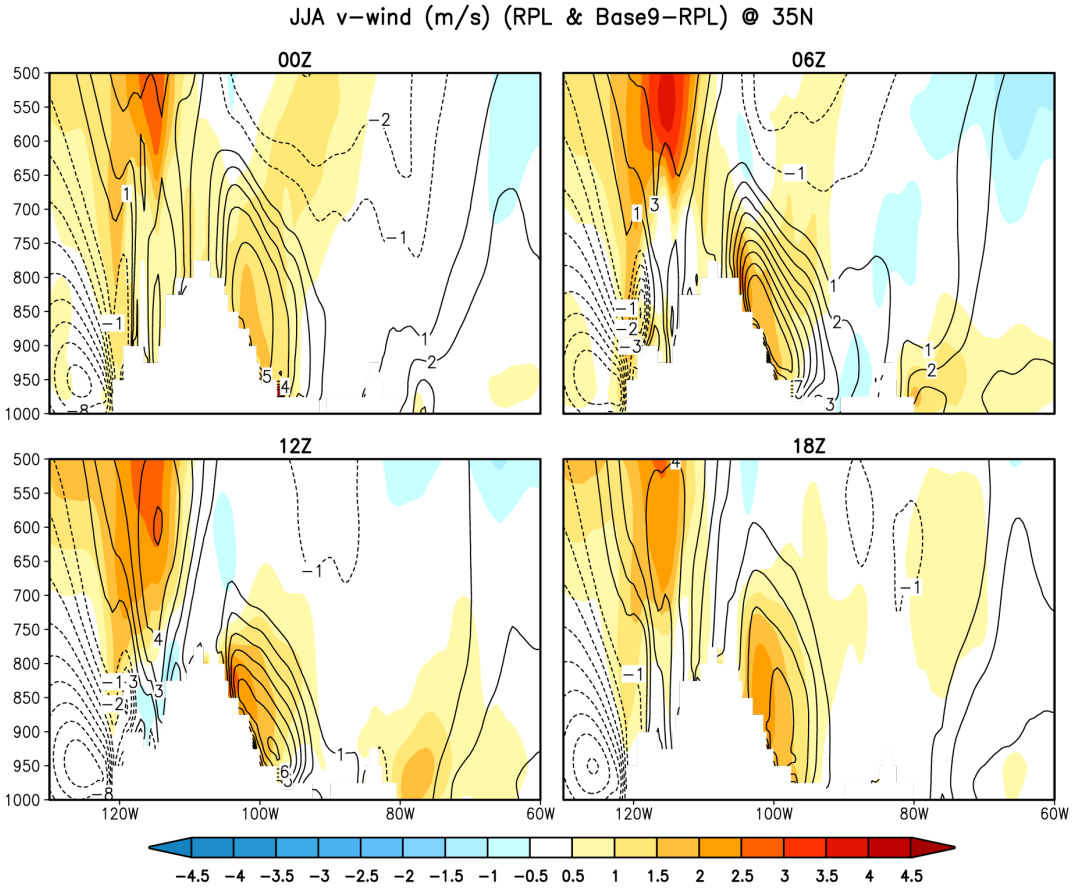

Figure 23: Vertical cross sections (130°W to 60°W, from 1000mb to 500mb, on pressure levels) at 35°N of the JJA v-wind differences (Base9 minus RPL; shaded, m/s/day) and RPL v-wind (contoured with dashed contours indicating negative values, m/s) for 00z, 06Z, 12Z and 18Z. The results are from the GEOS S2S V3 AOGCM replayed to MERRA-2 averaged over the time period 1981-2016.

(Base 9) and that from the replay run are indeed mostly positive in the jet region for all times of the day. It is only at night (06Z) that the increments act to accelerate the jet, but that occurs only in the lower right quadrant. This again is consistent with the GPLLJ biases in the free running model, which are negative in that region (Fig. 23, 06Z). It is worth noting that the negative increments underneath the jet maximum extend to the surface, suggesting that there may be insufficient surface friction in the model.

d) The wind increments viewed in terms of stream function and velocity potential

In order to better highlight the large-scale characteristics of the wind increments, we compute the stream function and velocity potential of the increments. These transformations effectively apply spatial filters (via the inverse Laplacian) to the increments allowing us to focus on their large-scale coherent aspects, in addition to assessing separately their rotational (stream function) and irrotational (velocity potential) components. We expect the rotational (non-divergent) component of the increments to be less sensitive to changes in the observing system.

Figure 24 shows the stream function of the seasonal mean wind increments near the surface (lowest model level), and Figure 25 shows corresponding results for the upper troposphere at 250mb. Comparing the results at these two levels, it is surprising that the rotational increments appear to exhibit much greater spatial coherence near the surface than at upper levels. In fact, the surface rotational increments show hemispheric wide coherence, with generally cyclonic circulation occurring in both hemispheres. A key exception is over the Tibetan Plateau where the increments force anticyclonic flow, especially during DJF (Fig. 24). Locally, northeastern South America and the Intra-Americas Sea regions both show pronounced maxima in cyclonic circulation especially

during DJF. At 250mb the increment stream function (Fig. 25) is noisier but does exhibit a tendency for anticyclonic circulation in both hemispheres (so opposite to what was found near the surface, Fig. 24), though this is more limited to the high latitudes. Notable exceptions are the regions of cyclonic circulation over northern Africa and the Intra-Americas Sea regions.

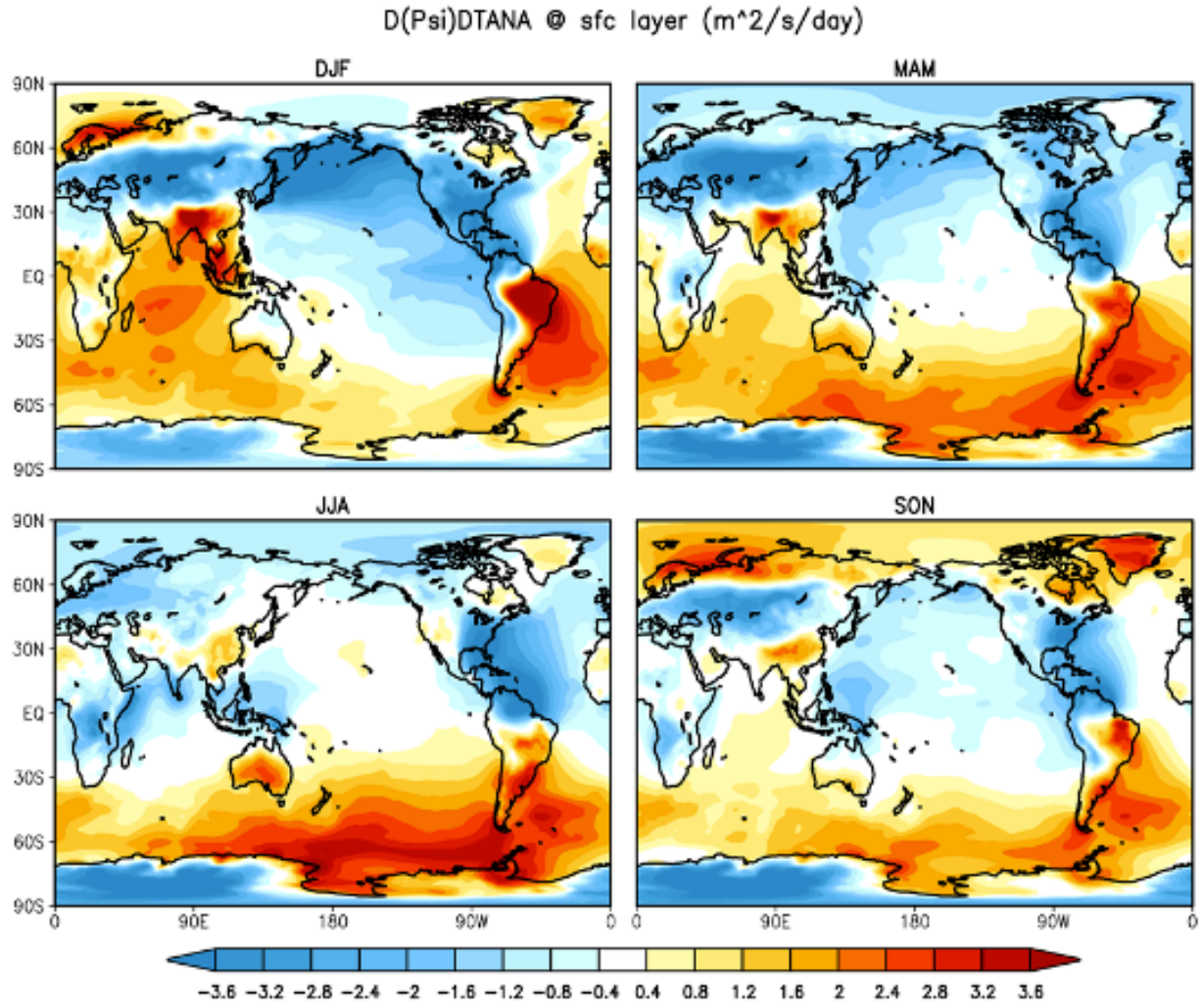

Figure 24: The model level 72 (approximately 992mb) seasonal mean stream function increments. The results are from the GEOS S2S V3 AOGCM replayed to MERRA-2 averaged over the time period 1981-2016. Units are 10^6 $m^2/s/day$.

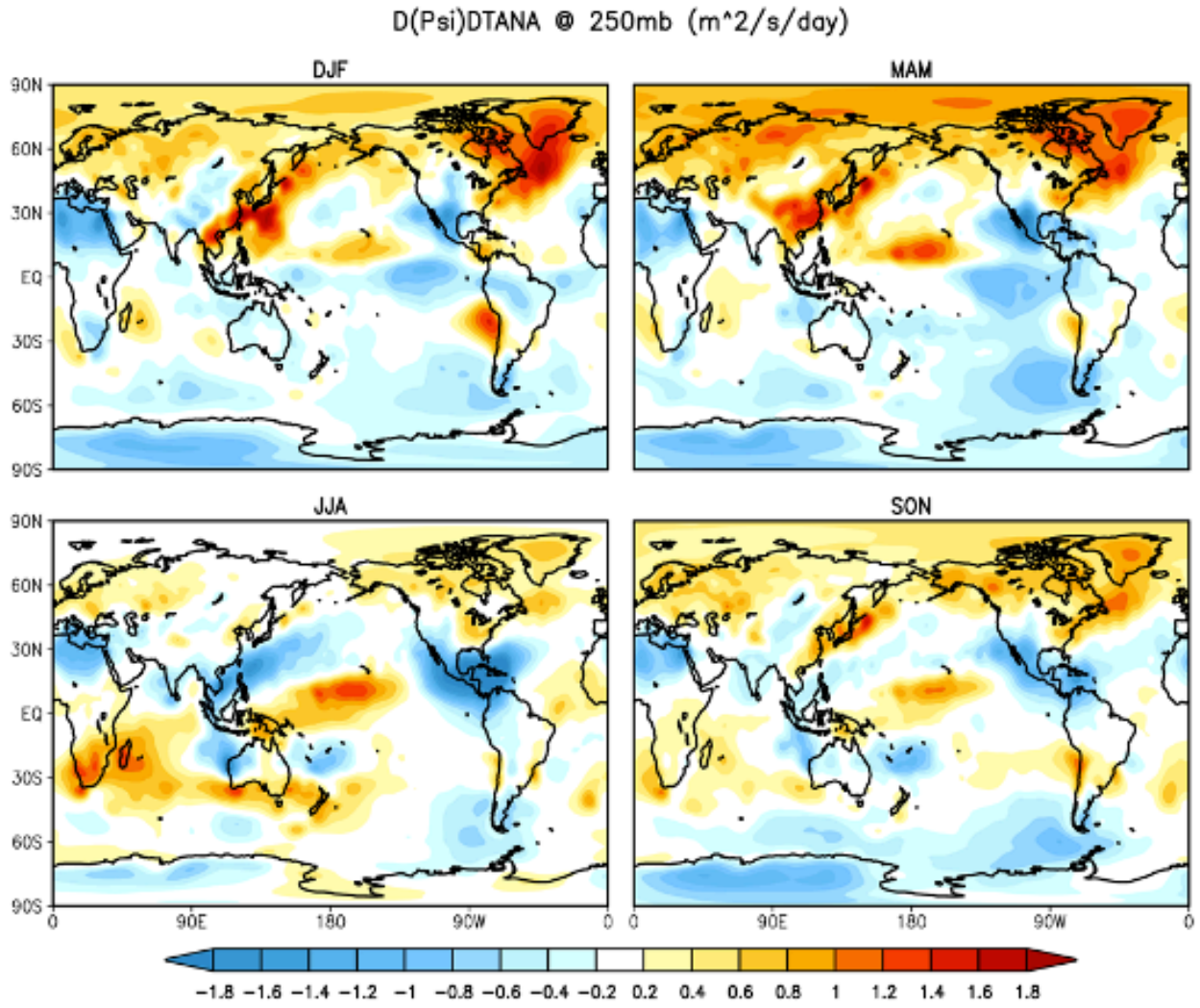

Figure 25: Same as Fig. 24, but for 250mb

Figure 26 shows the velocity potential of the seasonal mean wind increments near the surface (lowest model level), while Figure 27 shows corresponding results for 250mb. In general (during all seasons), the near surface velocity potential increments tend to have an east-west (roughly zonal wave number two) structure, while the upper-level fields have more of a north-south structure. As part of the wave number two structure, the near surface increments in the tropics and subtropics force divergence over the eastern Pacific, the Intra-Americas Seas, and northwestern South America, with a tendency for convergence to occur both to the west (much of the western Pacific) and to the

east (much of the Atlantic) of that. Over much of Eurasia, the maritime continent, and parts of Africa, the near surface increments produce a tendency for divergence.

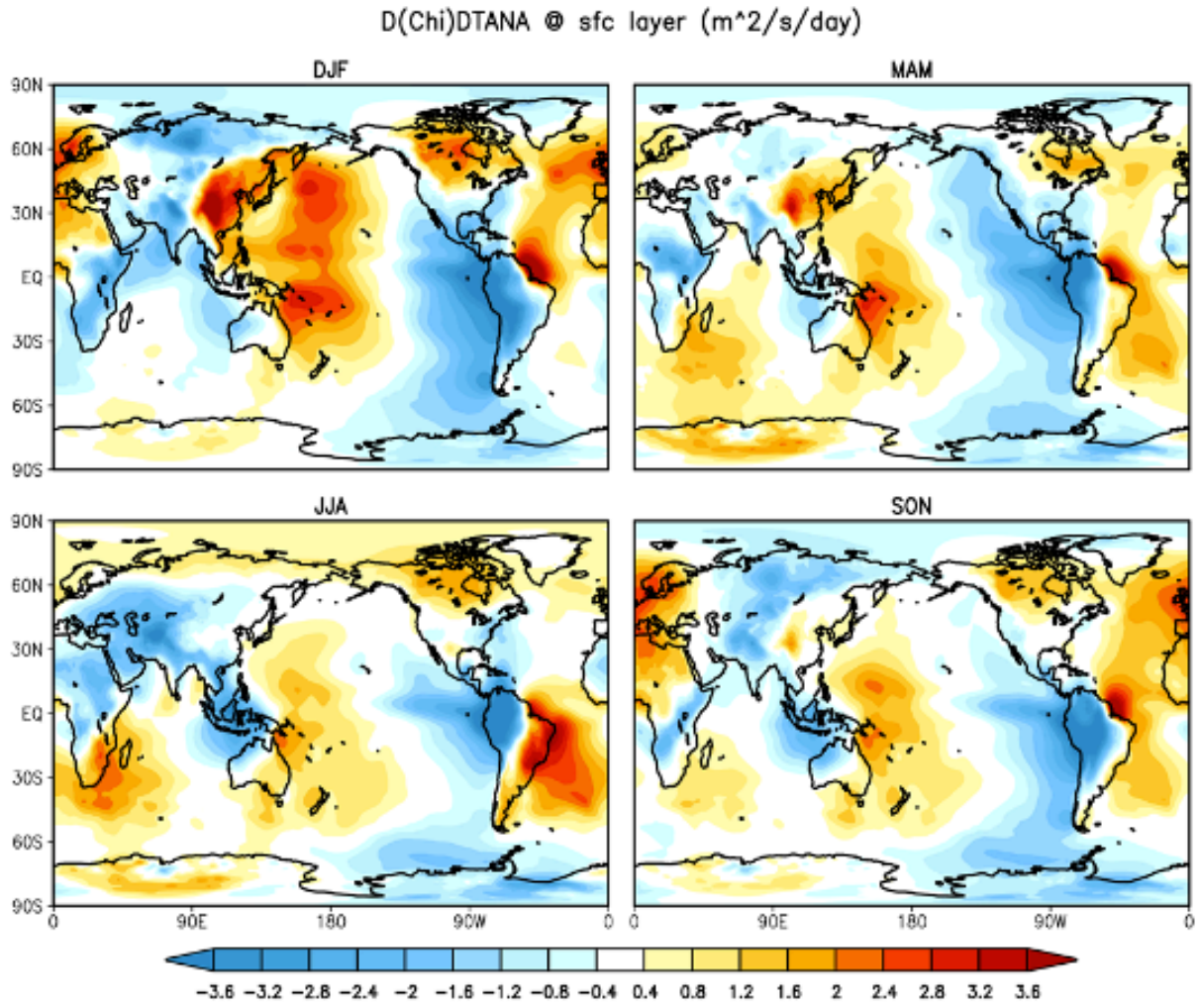

Figure 26: The model level 72 (approximately 992mb) seasonal mean velocity potential increments. The results are from the GEOS S2S V3 AOGCM replayed to MERRA-2 averaged over the time period 1981-2016. Units are 10^6 $m^2/s/day$.

At upper levels (Fig. 27), the increments produce a tendency for divergence over much of the tropics that is roughly coincident with the regions of maximum tropical rainfall during all seasons. This is consistent with the results shown earlier for the wind increments displayed as wind vectors (Fig. 12).

During JJA the regions of divergence extend northward to cover much of Eurasia and the United States. As such, the wind increments are presumably acting to reinforce the rainfall in these regions. In contrast, the increments produce a tendency for convergence in the extra-tropics of both hemispheres during all seasons, though this is most pronounced in the NH during DJF.

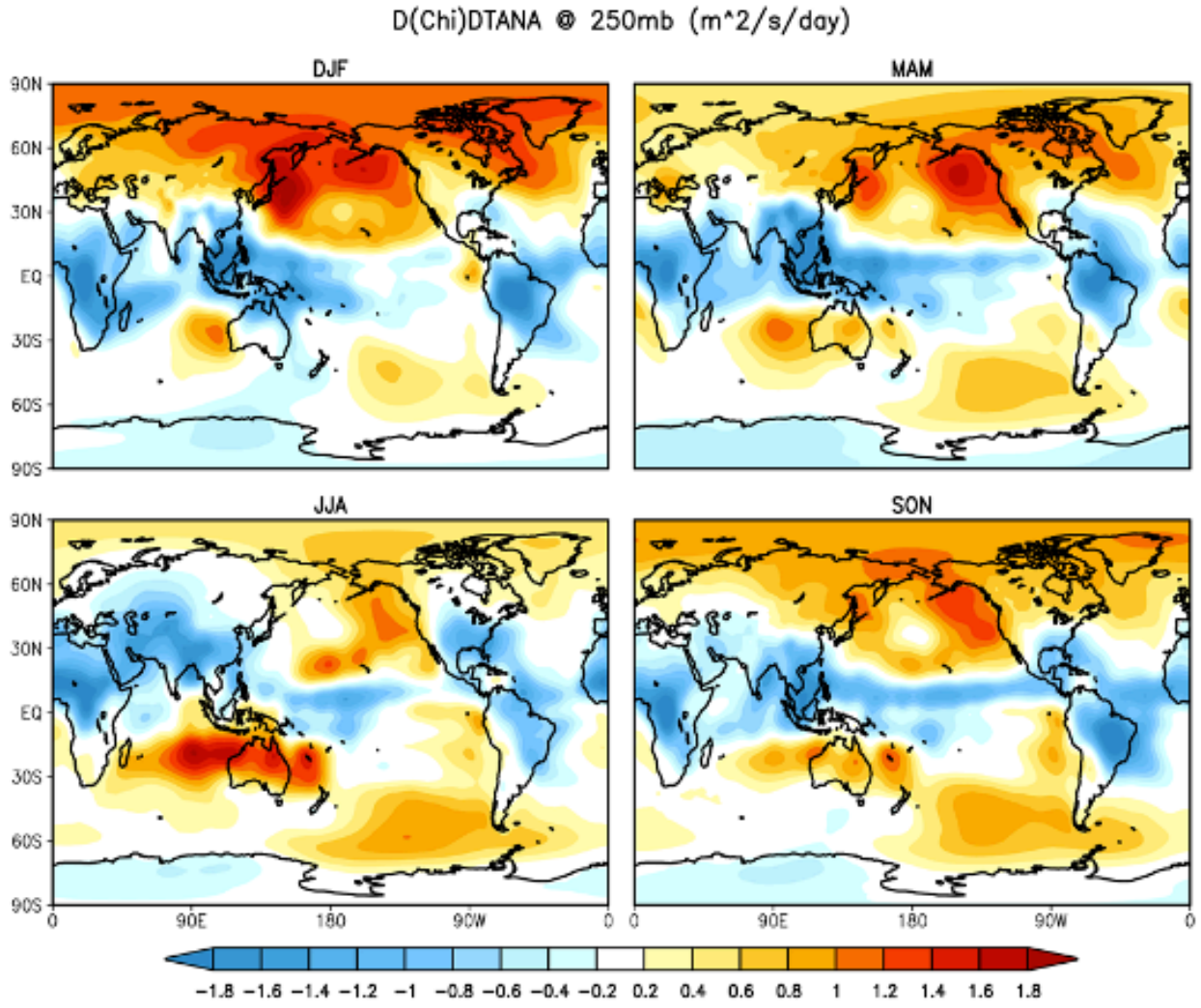

Figure 27: Same as Fig. 26 but for 250mb.

We next turn to an assessment of the variability of the wind, temperature and moisture increments.

3.2 Variability of the increments and impacts of observational inhomogeneities

Following the general approach of Robertson et al. (2011), we employ an empirical orthogonal function (EOF) analysis of the monthly mean increments to isolate the leading patterns of monthly variability (based on all months of the year for the time period 1981-2016). Our approach differs from Robertson et al. (2011) in that we employ a rotated EOF analysis (REOFs, Richman 1986), and the monthly means are computed separately for each time of the day (00Z, 06Z, 12Z, 18Z): the REOFs are computed after first removing the monthly climatologies separately for each time of day. Rotation helps to localize the patterns and removes the restriction of spatial orthogonality. Furthermore, we present a higher frequency version of the associated time series (the principal components or PCs) by projecting the 6 hourly increment anomalies onto those monthly REOFs. Here, the 6 hourly anomalies are computed by subtracting the 6 hourly climatologies. By computing the anomalies in this way, neither the REOFs nor the PCs contain any information about the systematic components of the variability (mean seasonal and diurnal cycles) discussed in Section 3.1.

We examine the time variability and spectral make-up of the 6 hourly PCs by employing a wavelet transform of the PCs (e.g., Meyers et al. 1993, Weng and Lau 1994, Schubert et. al. 1998). The algorithm employed here is that described in Weng and Lau (1994) and is based upon the complex Morlet wavelet:

$$\Psi_{a,b}(t) = a^{-1/2}\, exp\left(ih_\Psi \frac{t-b}{a}\right)\, exp\left(-\frac{1}{2}\left|\frac{t-b}{a}\right|^2\right), \qquad (4)$$

Where h_Ψ = 5.4. Here a (the dilation parameter), and b (the translation parameter) are real and $a >$ 0. As such, the Morlet transform isolates waves that are locally sinusoidal at time = b. In the

following, we present selected results of either the real part of the transform, which depicts the phase and intensity of the signal (so those cases where we think knowing the phase of the signal is helpful for the interpretation of the variability), or the modulus, which gives the energy density (so those cases where most of the useful information is in the amplitude of the signal).

The wavelet transform, by quantifying the time evolution of the spectral characteristics of the increments, also affords the opportunity to assess the potential impacts of observational inhomogeneities. Here we rely on the documentation of the observations assimilated in MERRA-2 provided by McCarty et al. (2016), as well as previous studies addressing the nature of long-term changes in the behavior of the MERRA-2 analysis increments (e.g., Robertson et al. 2011). We note several major changes to the observations going into MERRA-2 (McCarty et al. 2016). These include the introduction of the satellite radiances associated with AMSU A and B on 1 Nov. 1998, the introduction of AIRS in September of 2002, and the introduction of IASI on 17 September of 2008 (McCarty et al. 2016, Fig. 1). Perhaps the largest change in conventional data was the introduction and general increase in aircraft reports starting in the middle 1990s (with a sharp jump around 1997, McCarty et al. 2016, Fig. 2). Also, the amount of various atmospheric wind vector data showed a general increase starting about 1998 (McCarty et al. 2016, Fig. 3). Various surface wind data were introduced starting with SSM/I wind speeds in July 9, 1987 (McCarty et al. 2016, Fig. 4).

Keeping the above dates in mind, we begin in Section 3.2a with a focus on the variability of the wind increments formulated in terms of the stream function and velocity potential (see Section 3.1d). This is followed in Section 3.2b with a focus on the temperature and moisture increments.

a) The stream function and velocity potential

As already mentioned in Section 3.1d, the stream function and velocity potential transformations effectively apply spatial filters to the wind increments allowing us to focus on the large-scale coherent aspects of the increment variability. Furthermore, since we expect the rotational (non-divergent/stream function) component of the wind increments to be less sensitive to changes in the observing system, we will hopefully better isolate those aspects of the increment variability (via the stream function) that represent real physical dependencies (e.g., links to various physical phenomena, see Section 3.3) rather than artificial variability tied to the changing observation system, though as we shall see that is not always the case.

Figure 28 shows the five leading REOFs of the monthly mean stream function increments (and associated 6 hourly PCs) at the lowest model level. Recall that we combine all months of the year into the REOF calculation, though we do compute separate monthly means for each time of day. This is done for simplicity and assumes there is no seasonality in the spatial structures – something that is unlikely to be strictly true. As such, any seasonality is captured here only in terms of the time variability tied to the associated PCs. REOF 1 (Fig. 28a left panel) shows what is largely a NH high latitude zonally symmetric structure with the largest spatial loadings occurring northward of about 60°N, with weaker loading of opposite sign to the south of that between 0° and 100°E. It accounts for about 10% of the monthly variance. The associated PC 1 (Fig. 28a, right panel) shows

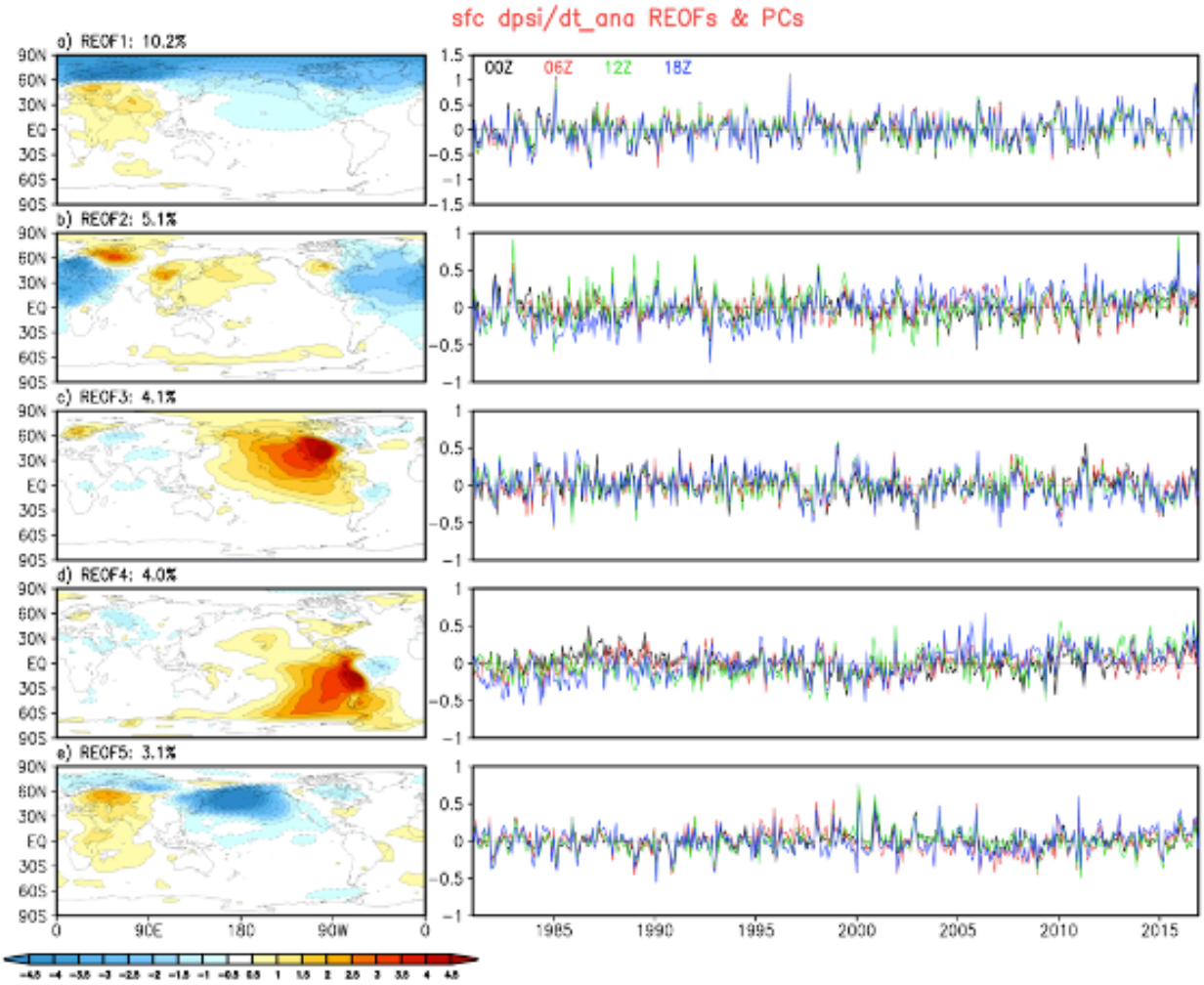

Figure 28: Left panels: the leading REOFs of the model level 72 (approximately 992mb) stream function increments. Right panels: the associated PCs plotted separately for each time of day. The REOFs were obtained from monthly anomalies that were computed separately for each time of day: 00z, 06z, 12z and 18z. The PCs were obtained by projecting the 6-hourly anomalies (obtained by removing separate 6-hourly climatologies for each time of day) onto the monthly REOFs (see text for details). The results are from the GEOS S2S V3 AOGCM replayed to MERRA-2 for 1981-2016.

little evidence of a trend or diurnal variability[1]. This is confirmed by the modulus of the wavelet decomposition of PC 1 (Fig. 29) which shows very little amplitude at diurnal frequencies, with the largest amplitudes occurring between synoptic and sub-seasonal time scales (4-64 days). There do

[1] Recall that we removed the long term mean diurnal cycle (the systematic part) as described above.

appear to be certain time periods when the increments achieve especially large amplitude (for example during the second half of 1996), though there seems to be no clear phase locking of those episodes with the annual cycle. We will look in more detail at that variability and possible links to various atmospheric modes of variability in Section 3.3.

The second REOF of the monthly mean stream function increments (Fig. 28b, left panel) accounts for about 5% of the monthly variance, is largely confined to the NH extratropics, and has a zonal wave number one structure. The associated PC 2 time series (Fig. 28b, right panel) shows some dependence of the variability on the time of day. For example, the 12Z values have a relatively large amplitude and a tendency for positive values prior to about the year 2000. After that they tend to be negative for about 5 years, after which they trend toward positive values again. The 18Z values show a long-term increase from generally negative values prior to about 2000, and positive values after that (roughly opposite to the behavior of the 12Z values). As mentioned above, there is a major change in the observations around that time (the year 2000) with the introduction of AMSU data on 1 November 1998 (McCarty et al. 2016). Also potentially relevant is the introduction of IASI in of September of 2008. The modulus the wavelets (Fig. 30) shows a clear signature of diurnal variability throughout the record as well as longer term variability, some of which is presumably linked to ENSO (e.g., 1982/83; 1997/98). Much of the variability, however, occurs at sub-seasonal (two week to two month) time scales. This is episodic but occurs most often during the NH cold season (e.g., winter of 2015/16).

The next three REOFs tend to have more localized spatial structures, with REOF 3 (Fig. 28c) focused on North America, REOF 4 (Fig. 28d) focused on western South America, and REOF 5 (Fig. 28e)

having much of the spatial loading concentrated over the North Pacific. We will discuss some of these modes later in the context of their similarity to the REOFs of the velocity potential increments

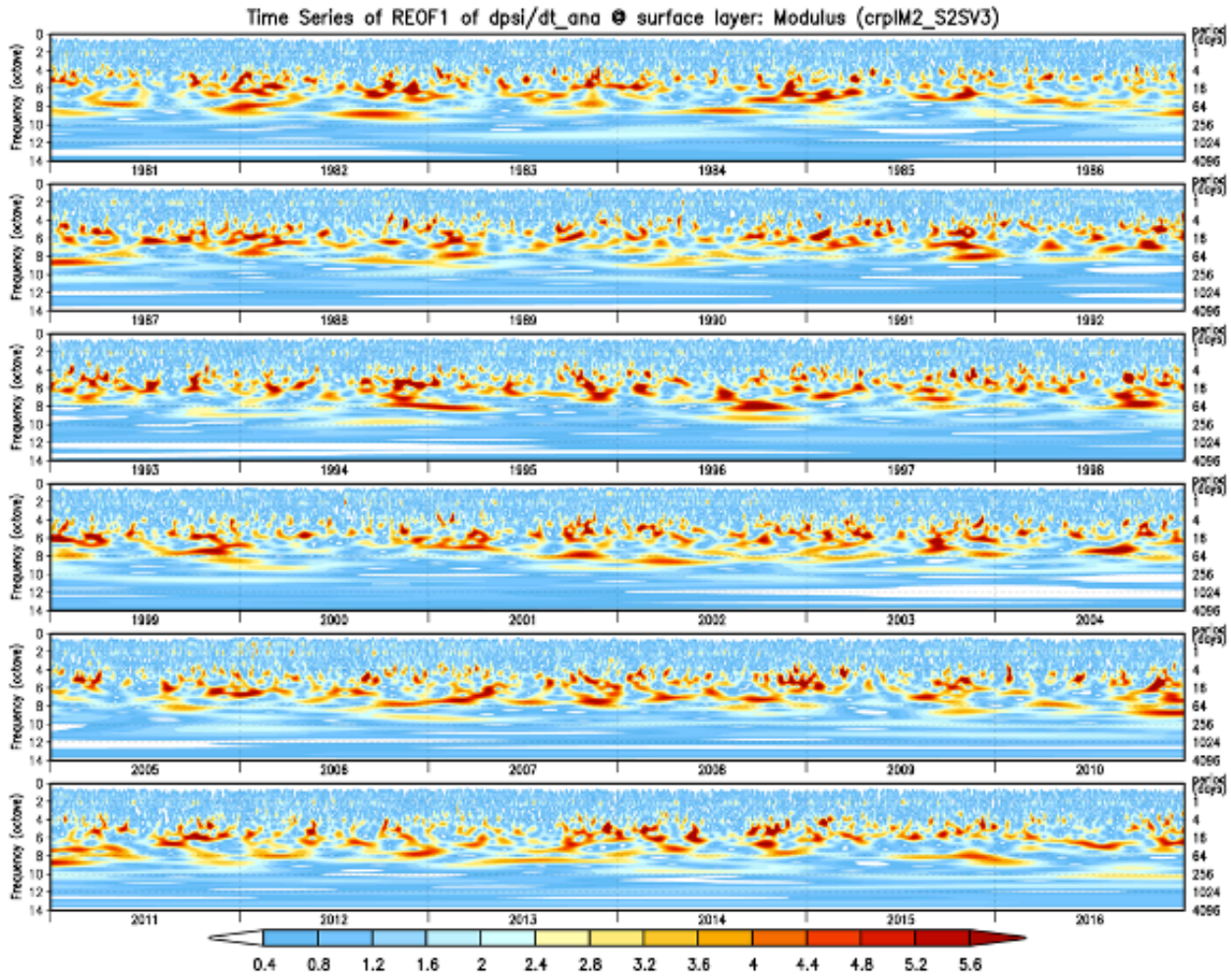

Figure 29: The time series of the modulus of the wavelet decomposition of PC 1 of the model level 72 (approximately 992mb) stream function increments (see text for details). The results are from the GEOS S2S V3 AOGCM replayed to MERRA-2 for 1981-2016.

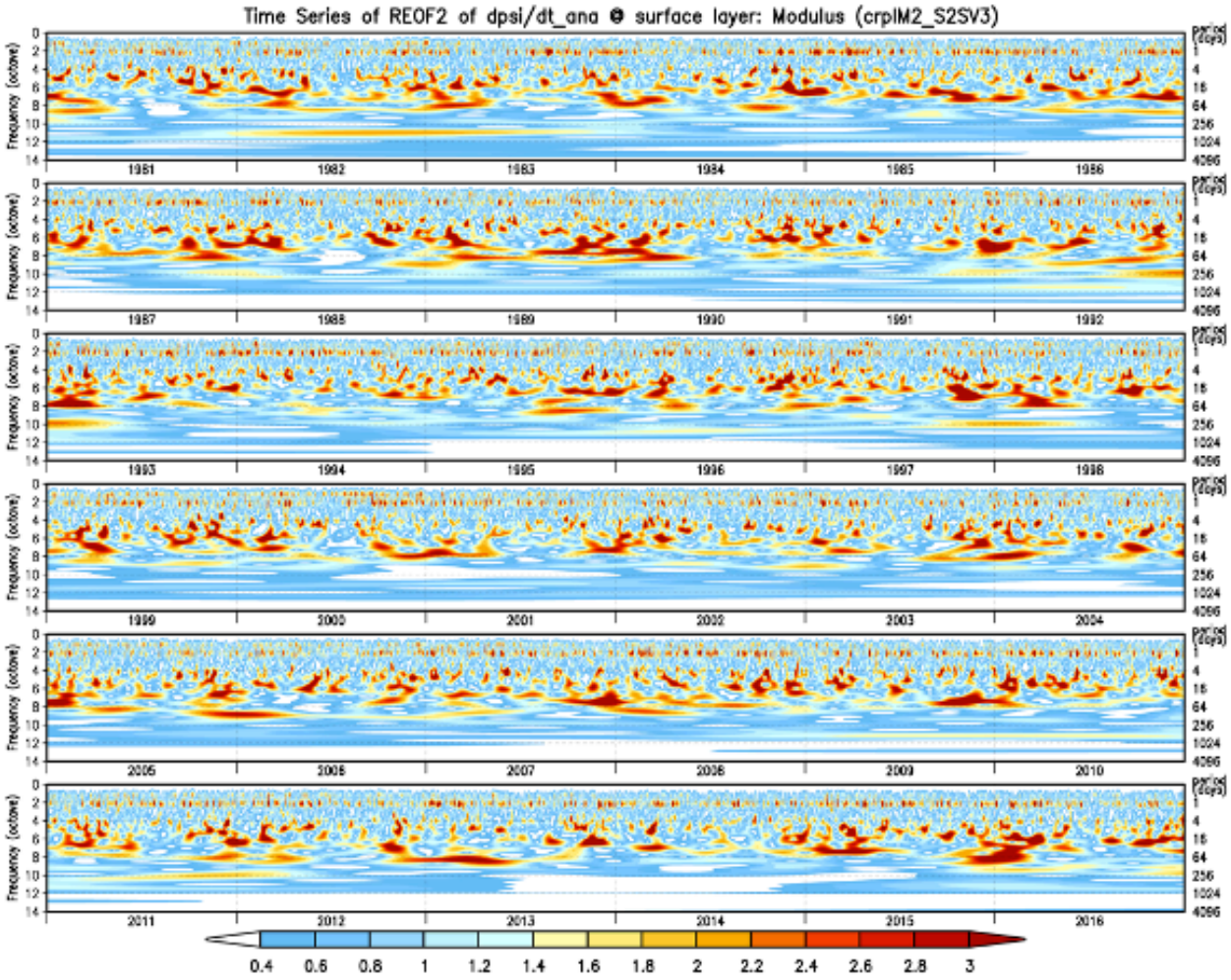

Figure 30: Same as Fig. 29, but for PC 2.

and their links to climate variability. We note in particular that REOF 5 has a substantial correlation with the PNA and that REOF 3 shows some correlation with ENSO (see Section 3.3).

Figure 31 shows the REOFs (left panels) of the monthly mean velocity potential increments at the model's lowest level. The corresponding 6 hourly PCs are shown in the right panels. In contrast

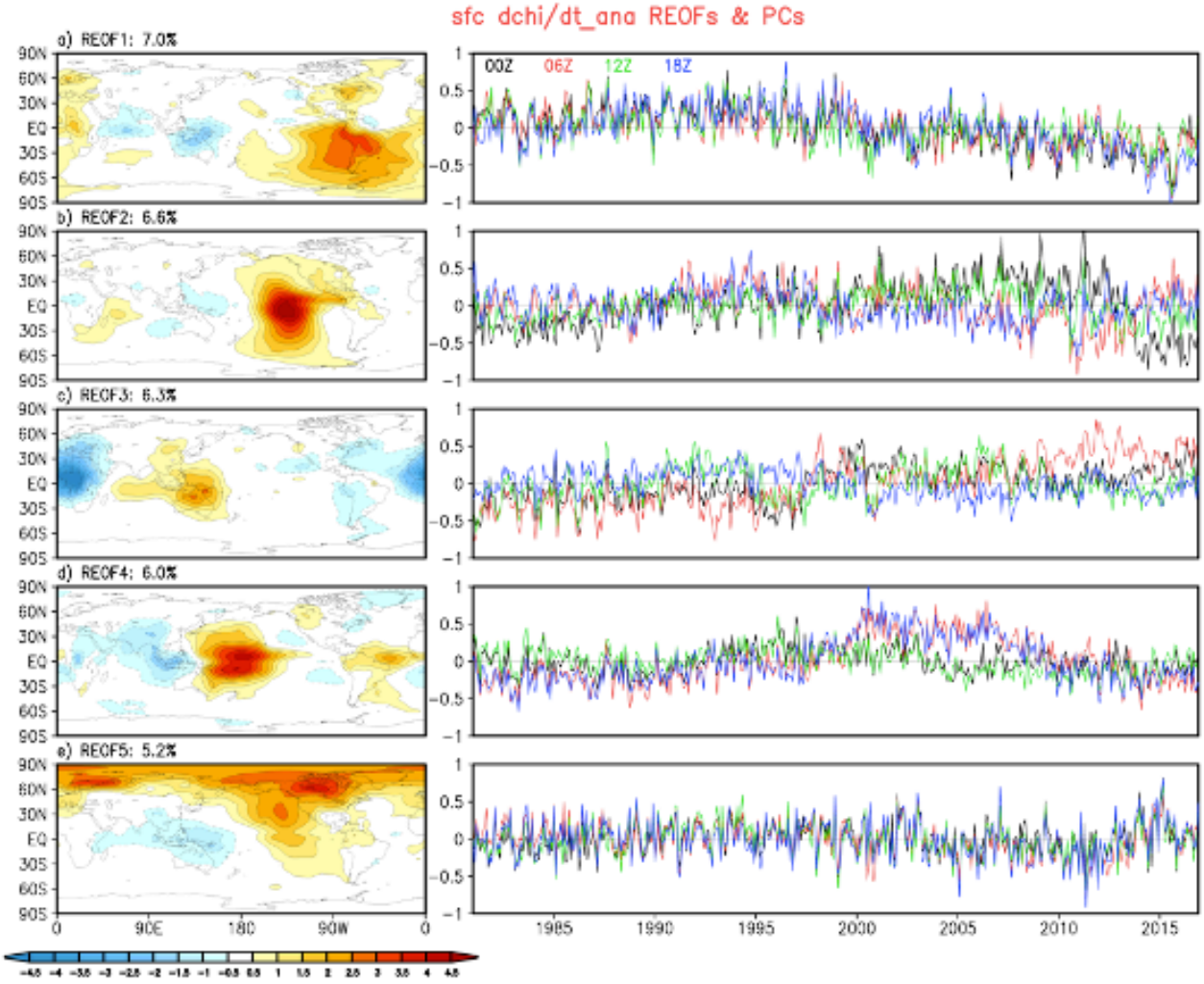

Figure 31: Left panels: the leading REOFs of the model level 72 (approximately 992mb) velocity potential increments. Right panels: the associated PCs plotted separately for each time of day. The REOFs were obtained from monthly anomalies that were computed separately for each time of day: 00z, 06z, 12z and 18z. The PCs were obtained by projecting the 6-hourly anomalies (obtained by removing separate 6-hourly climatologies for each time of day) onto the monthly REOFs (see text for details). The results are from the GEOS S2S V3 AOGCM replayed to MERRA-2 for 1981-2016.

with the stream function PCs (Fig 28), we see immediately that the PCs of the velocity potential generally show much greater long-term variability, including long term changes in the character of the diurnal variability. REOF 1 (Fig. 31a, left panel, 7% of the variance) is focused on South America and the neighboring areas of the Pacific and Atlantic Oceans. The corresponding PC has a rather abrupt change in character around the year 2000, with general positive values (indicating low

level convergence) prior to 2000, and a trend toward negative values (indicating low level divergence) beginning after that.

The wavelet modulus (Fig. 32) shows that PC 1 has considerable long term (annual and longer) variability, though again much of the variability occurs at subseasonal time scales. In addition, there is considerable diurnal and semi-diurnal variability that appears to have a longer-term envelope modulating its variability. For example, the second half of the year 2000 has especially strong diurnal and semi-diurnal variability. It is noteworthy that this REOF is for the most part spatially collocated with REOF 5 of the stream function (cf. Figs. 31a and 28d, left panels).

REOF 2 (Fig. 31b, left panel) is centered on the eastern equatorial Pacific just east of the dateline. The corresponding PC values (Fig. 31b, right panel) again exhibit substantially different behavior before and after the year 2000. In this case the amplitude of the diurnal variability shows a dramatic increase after 2000, with another rather abrupt change around 2012/2013 (e.g., the 00z and 12Z values shift from predominately positive values to negative values). These changes are reflected in the wavelet modulus (Fig. 33) which show a pronounced increase in the diurnal and semi-diurnal modulus over the 36 years.

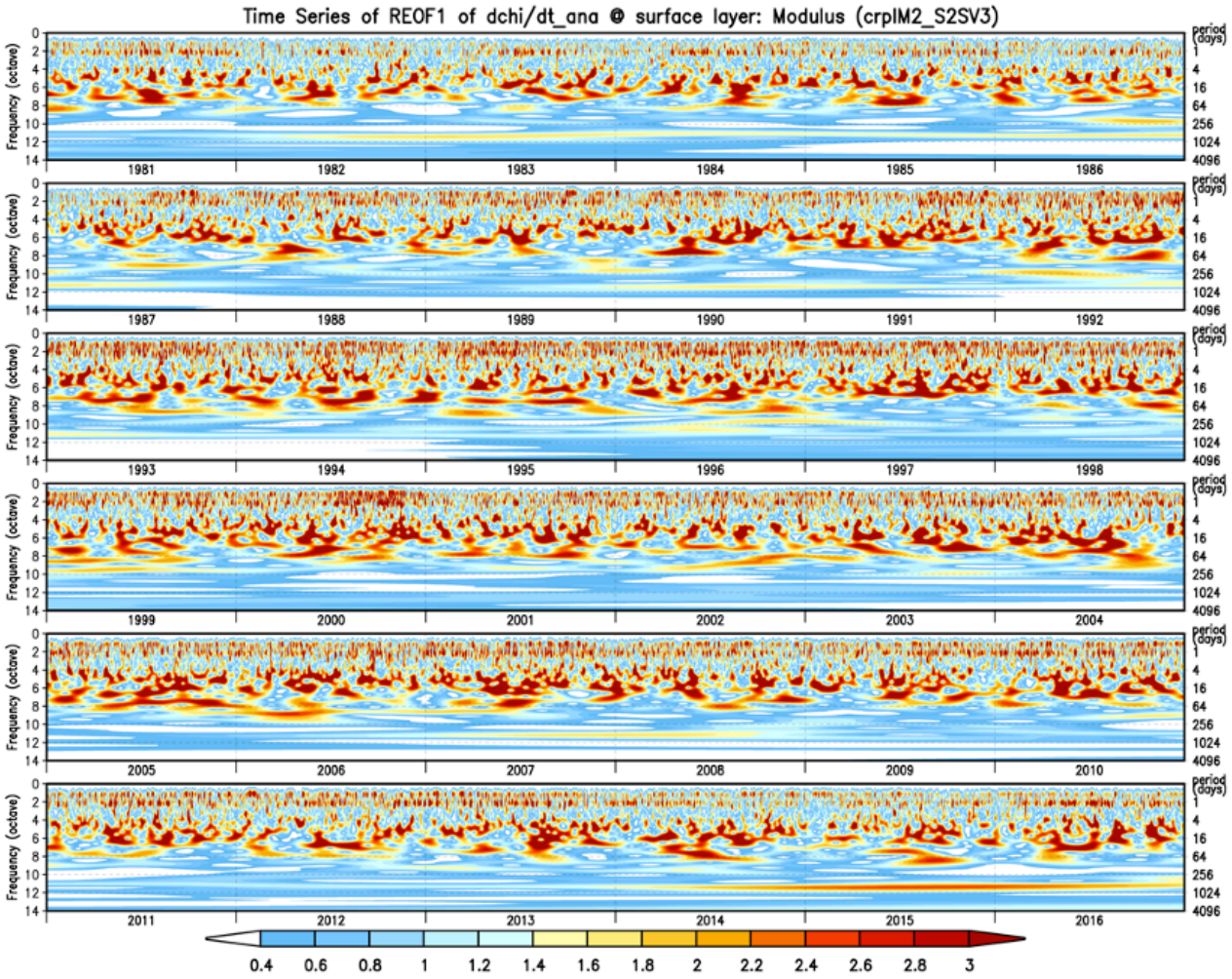

Figure 32: The time series of the modulus of the wavelet decomposition of PC 1 of the model level 72 (approximately 992mb) velocity potential increments (see text for details). The results are from the GEOS S2S V3 AOGCM replayed to MERRA-2 for 1981-2016.

REOF 3 (Fig. 31c, left panel) is characterized by a dipole spanning Africa and the maritime continent, while REOF 4 (Fig. 31d, left panel) straddles the equator (anticyclonic/cyclonic pair) over the warm pool. The corresponding PCs (right panels) again exhibit rather different behaviors before and after 2000. PC 4 in particular shows rather different values for 00Z/12Z and 06Z/18Z between the years 2000 and 2008 – a period roughly bookended by the introduction AMSU (Nov 1998) and IASI (Sep 2008). Also, PC 3 shows a peculiar positive trend that appears to be primarily associated with the 6Z values. In contrast, REOF 5 (a largely zonal structure north of about 60N) exhibits a

fairly stable time evolution, though it does transition to predominately negative values between 2003 and 2012. Here it is noteworthy that this REOF is for the most part spatially collocated with REOF 1 of the stream function (cf. Figs. 31e and 28a, left panels). We shall see that this structure reappears in several different variables.

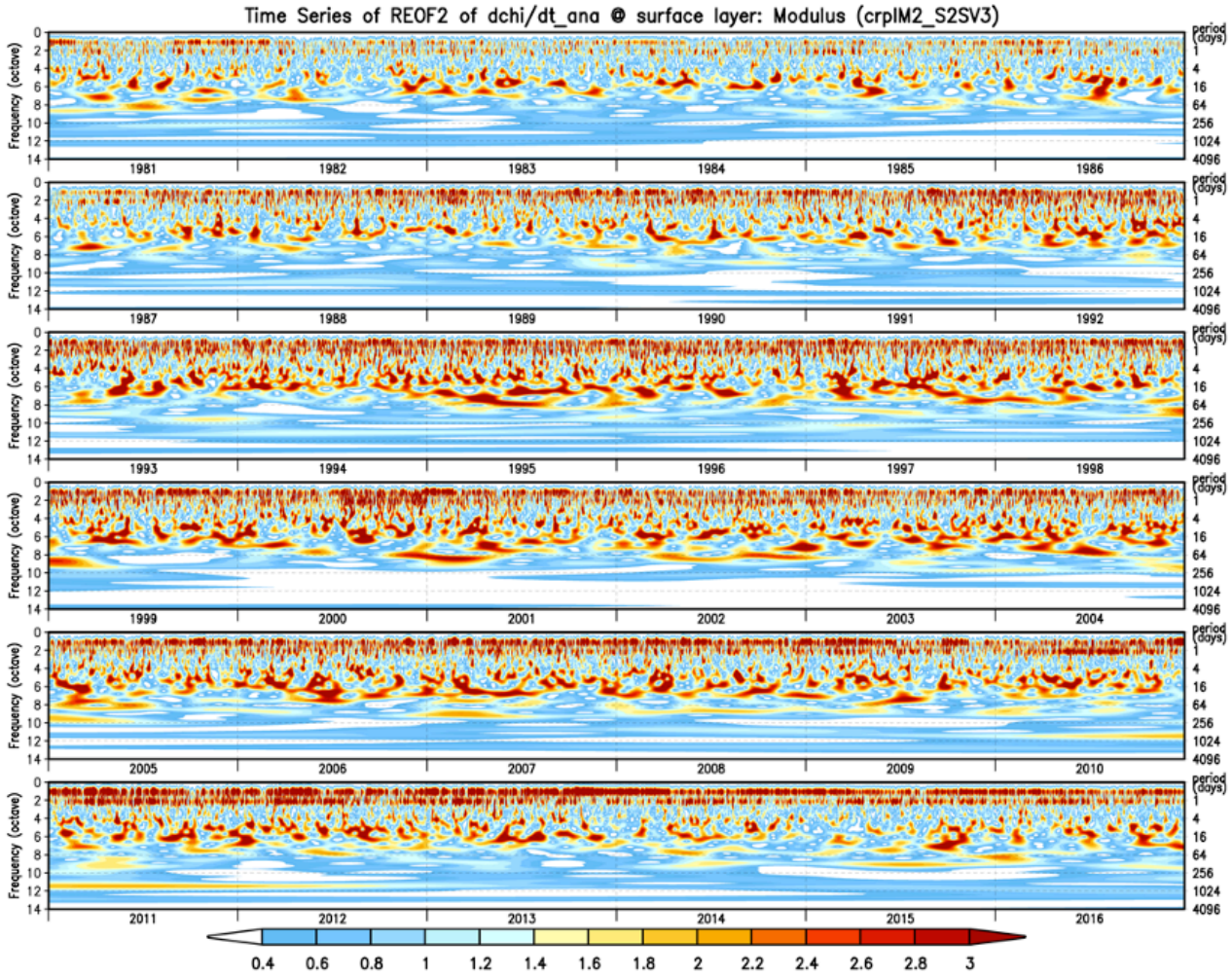

Figure 33: Same as Fig. 32 except for PC 2.

Overall, the above results show that the leading REOFs of the velocity potential increments at the lowest model level (with the exception of REOF 5) appear to be substantially impacted by the changes in the observing system, with the introduction of AMSU A and B (Nov. 1998) and AIRS (Sep. 2002) again likely playing a key role.

Figure 34 shows the five leading REOFs of the monthly mean stream function increments (and associated 6 hourly PCs) at 250mb. With the exception of REOF 3, which has a zonally-symmetric structure in the north polar region (north of about 60°N) that we've already seen several times before, the leading modes tend to be fairly localized (REOF 1 in the extratropical South Pacific, Fig 34a; REOF 2 in the North Atlantic, Fig. 34b; REOF 4 in the extratropical South Atlantic, Fig. 34d; REOF 5 in the North Pacific, Fig. 34e). All 5 PC time series (RHS of Fig.34) show substantially different behaviors for the 4 times of the day. This is shown more clearly in Fig 35 for PC 1, which has the largest values of the modulus at the semi-diurnal and diurnal time scales, although the strength of that signal undergoes a gradual transition toward smaller values over the course of the record. The time series of PC 1 (Fig. 34a, right panel) in fact shows a rather complicated and episodic behavior, with the late 1980s and the late 1990s showing especially large diurnal signals (see also Fig. 35). Fig 36 shows that the modulus of PC 2 is also primarily at the semi-diurnal and diurnal time scales, and there is again a gradual trend toward smaller values at those time scales. PC 3, while again having variability primarily at the semi-diurnal and diurnal time scales (wavelet modulus not shown), undergoes a low frequency oscillation of the amplitudes between about 1980 and 1995 with the 00Z/12Z and the 06/18Z values tending to oppose each other (Fig. 34c, right panel). PC 5 also shows a reduction in the wavelet modulus of the diurnal cycle after about 2002 (not shown), something that is readily apparent from Fig. 34e (right panel).

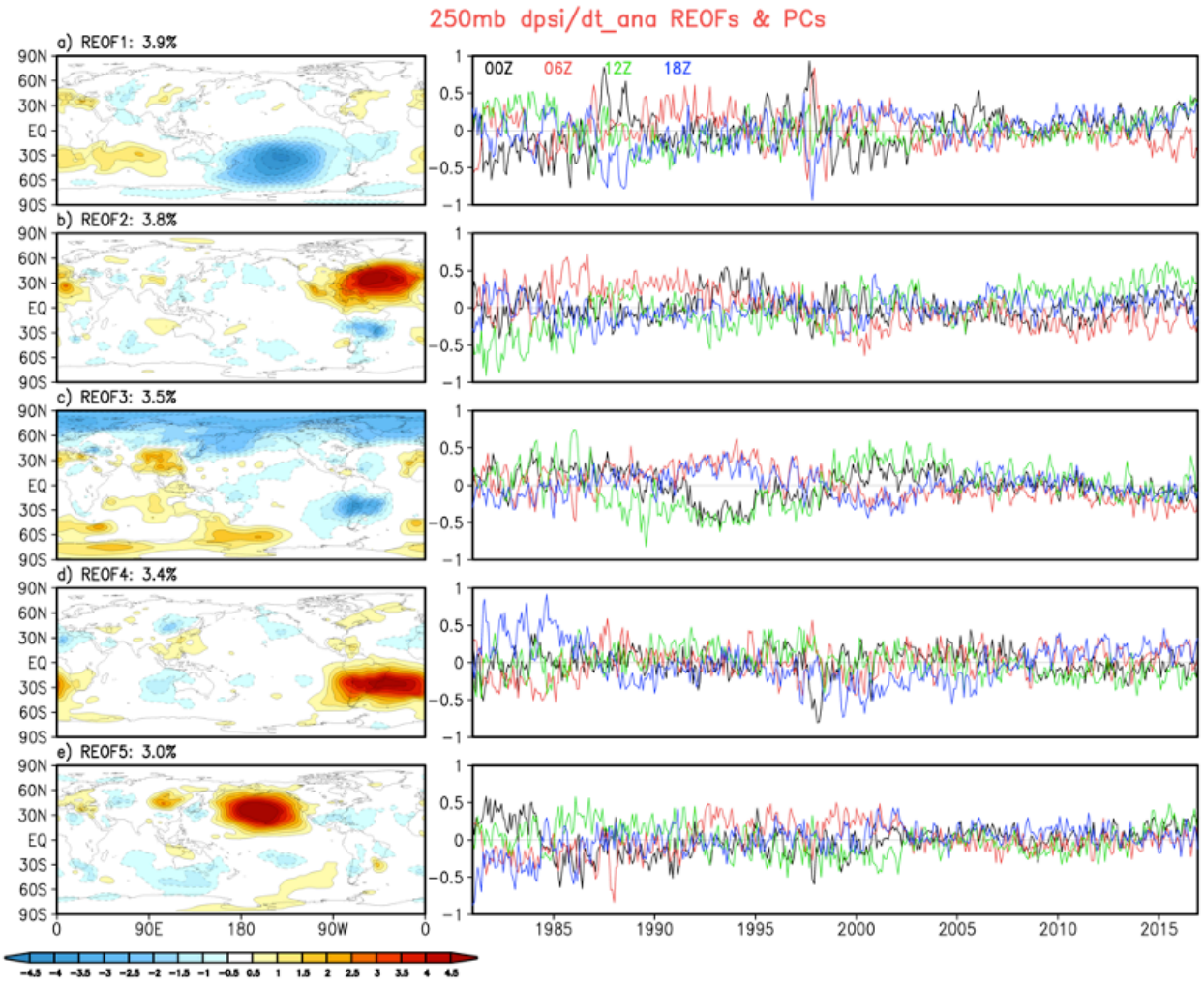

Figure 34: Left panels: the leading REOFs of the 250mb stream function increments. Right panels: the associated PCs plotted separately for each time of day. The REOFs were obtained from monthly anomalies that were computed separately for each time of day: 00z, 06z, 12z and 18z. The PCs were obtained by projecting the 6-hourly anomalies (obtained by removing separate 6-hourly climatologies for each time of day) onto the monthly REOFs (see text for details). The results are from the GEOS S2S V3 AOGCM replayed to MERRA-2 for 1981-2016.

The above results show that the behavior of the 5 leading 250mb stream function PCs (Fig. 34, right panels) is rather complicated with a less clear signature of any abrupt changes in character occurring around 2000, though there is a general tendency for the differences between the different times of the day (which are quite pronounced during the first 2 decades) to become smaller during the last 2 decades or so. PC 5 shows for example an abrupt change to greater agreement in the

values for the different times of day after around 2002: something that could be tied to the introduction of AIRS data. It is also possible that the smaller differences between the different times of day in the more recent decades is linked to changes in the amount of aircraft data going into MERRA-2 (McCarty et al 2016, Fig. 2), though that certainly requires further investigation.

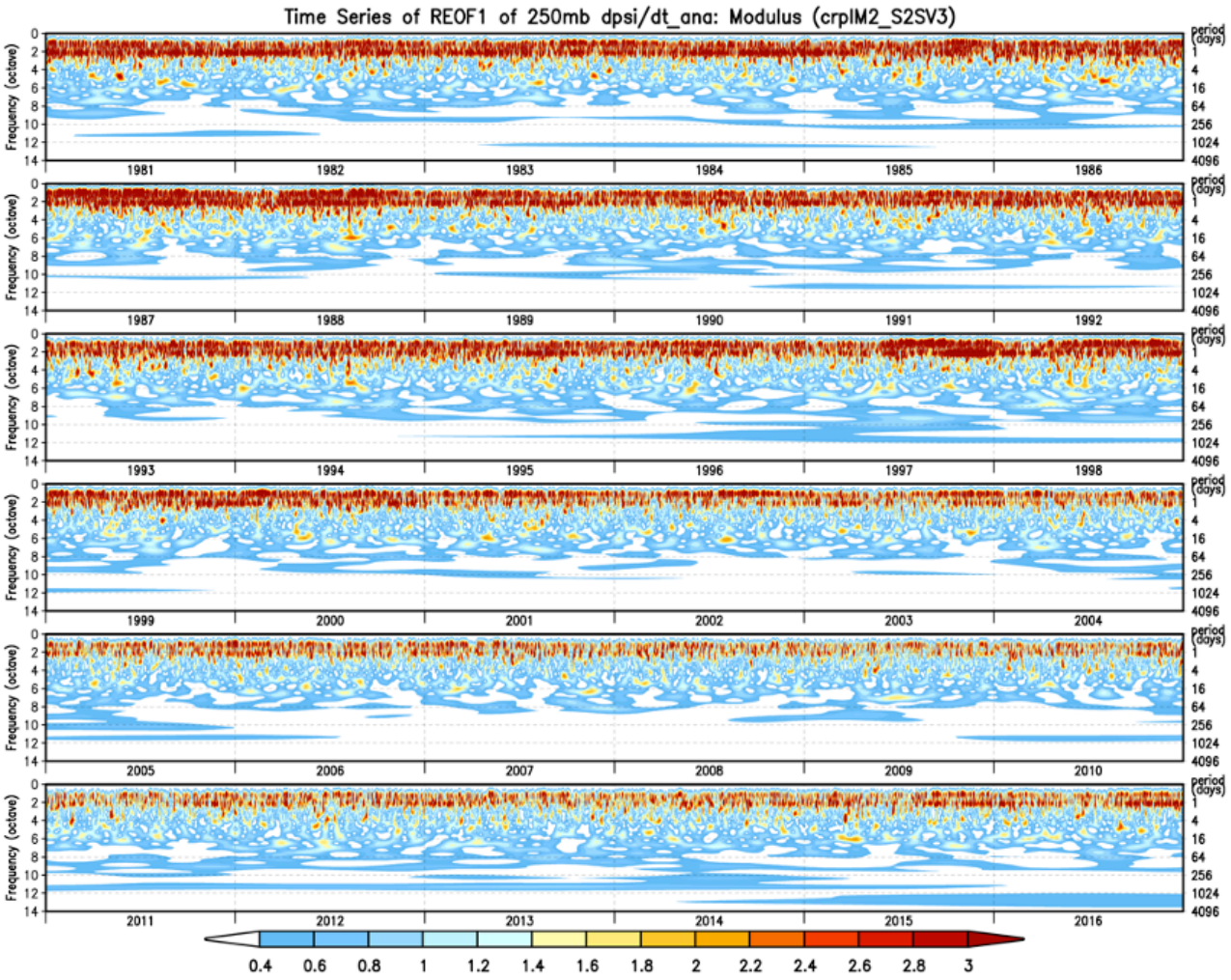

Figure 35: The time series of the modulus of the wavelet decomposition of PC 1 of the 250mb stream function increments (see text for details). The results are from the GEOS S2S V3 AOGCM replayed to MERRA-2 for 1981-2016.

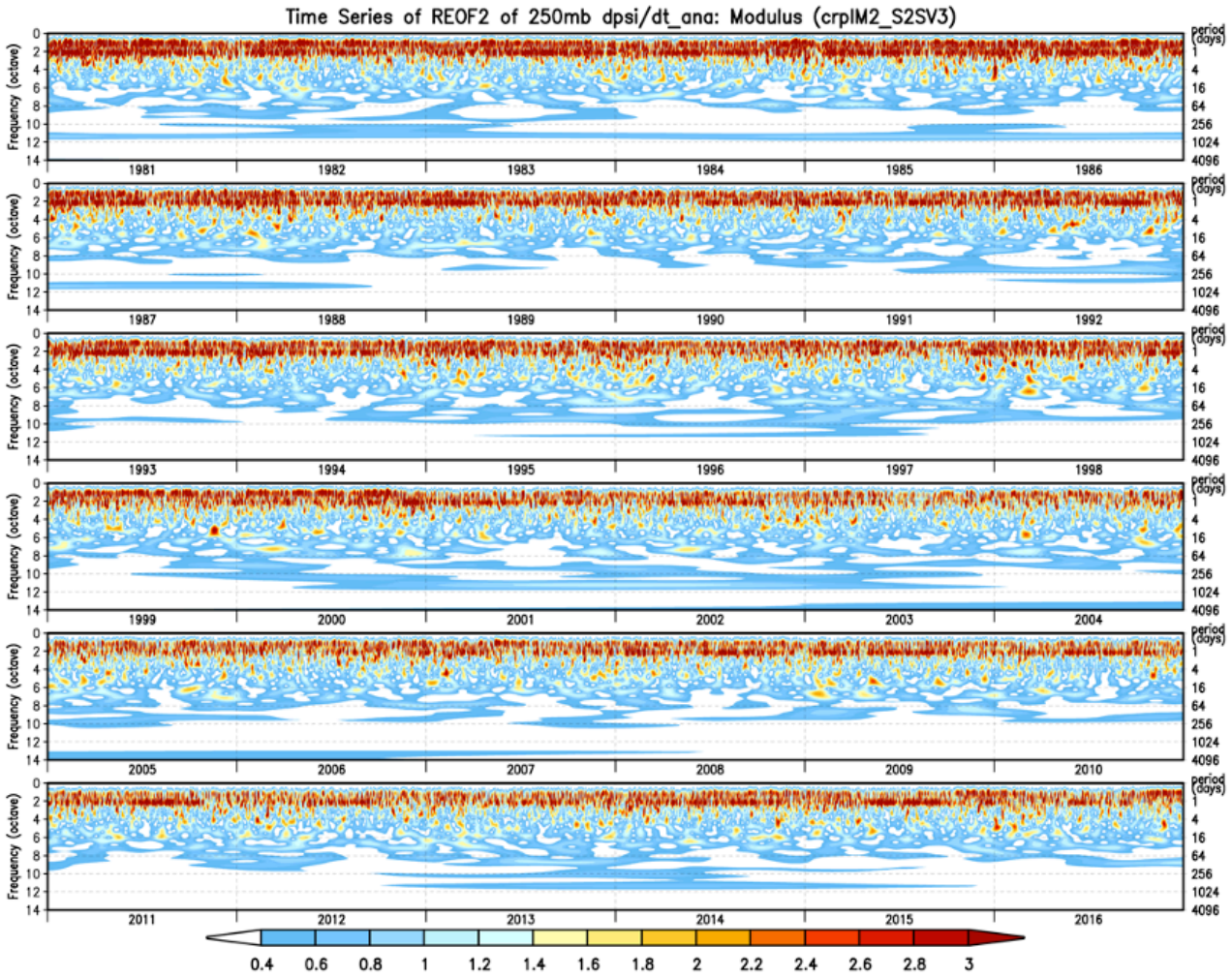

Figure 36: Same as Fig. 34 except for PC 2.

Figure 37 (left panels) shows the five leading REOFs of the monthly mean velocity potential increments (and associated 6 hourly PCs) at 250mb. REOF 1 has a zonal wave two structure spanning southeast Asia, the maritime continent, and the Pacific Ocean, where it splits into two anomalies: one in the North Pacific, and one in the South Pacific. REOF 2 has a zonally symmetric component north of about 60°N similar in structure to what we've seen in several previous leading REOFs (cf. REOF 5 of surface velocity potential, Fig. 31e; REOF 1 of surface stream function, Fig. 28a; REOF 3 of 250 stream function, Fig. 34c) together with an anomaly of opposite sign over the

Pacific warm pool. REOFs 3-5 (Figs 37c-e, left panels) all have dipole structures spanning various regions of the eastern hemisphere between 30°E and 180°E. All five PCs (Fig. 37, right panels) show some evidence of low frequency variations along with episodes of pronounced interannual variability, especially after 2010, with PC 1 (Fig. 37a, right panel) and PC 3 (Fig. 37c, right panel) also showing large interannual variations during the 1990s. The modulus of the wavelet of PC 1

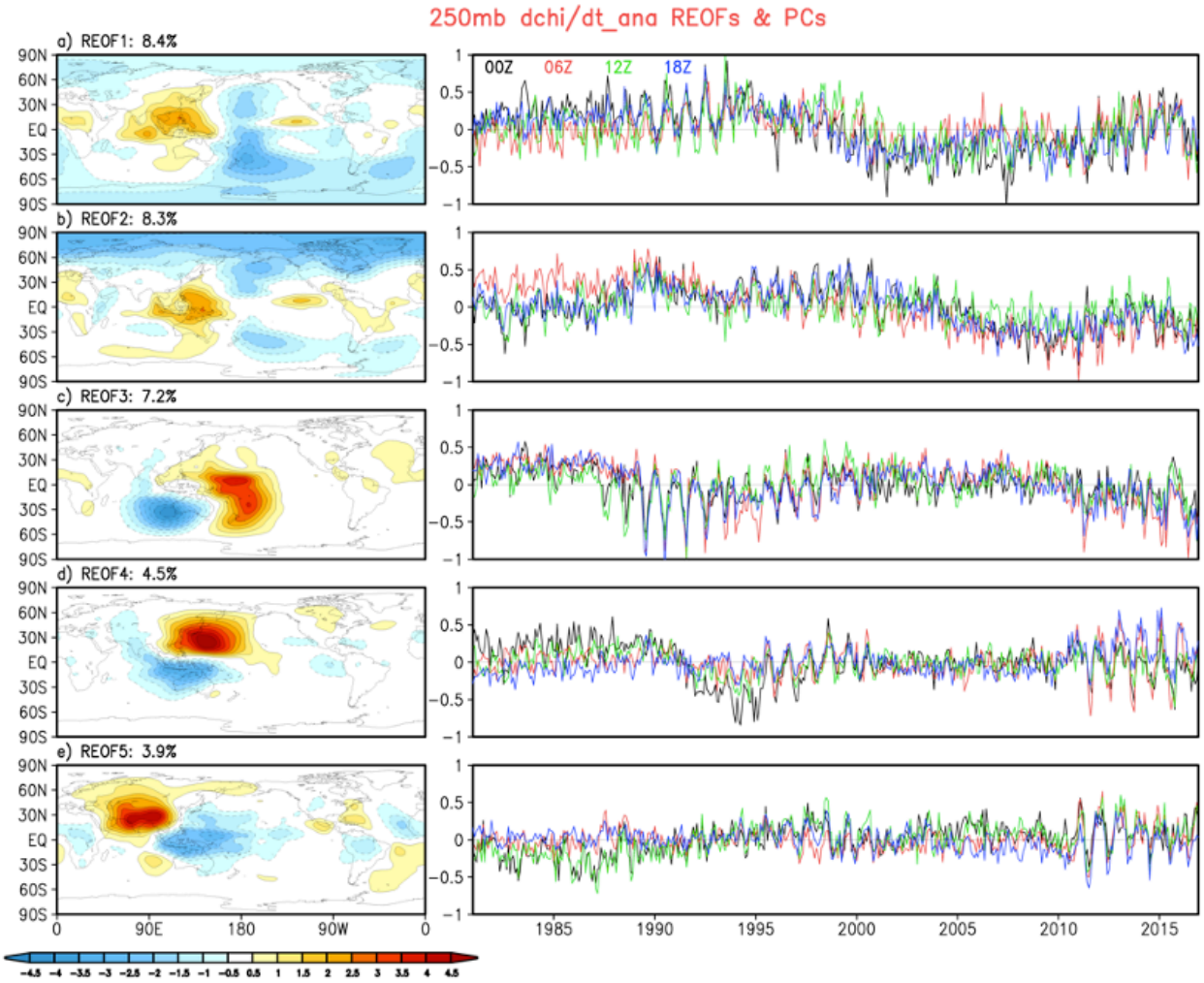

Figure 37: Left panels: the leading REOFs of the 250mb velocity potential increments. Right panels: the associated PCs plotted separately for each time of day. The REOFs were obtained from monthly anomalies that were computed separately for each time of day: 00z, 06z, 12z and 18z. The PCs were obtained by projecting the 6-hourly anomalies (obtained by removing separate 6-hourly climatologies for each time of day) onto the monthly REOFs (see text for details). The results are from the GEOS S2S V3 AOGCM replayed to MERRA-2 for 1981-2016.

(Fig. 38) and that of PC 2 (Fig. 39) show pronounced semi-diurnal and diurnal variability throughout the record together with more episodic periods of variability at synoptic and subseasonal time scales. PC 3 stands out as exhibiting especially large annual variability, which is most pronounced during 1988-1993 and again (though somewhat weaker) throughout the second half of the 1990s (Fig. 40). Here we show the real part of the wavelet transform to highlight the phase change in PC 3's annual cycle that occurs between these two time periods.

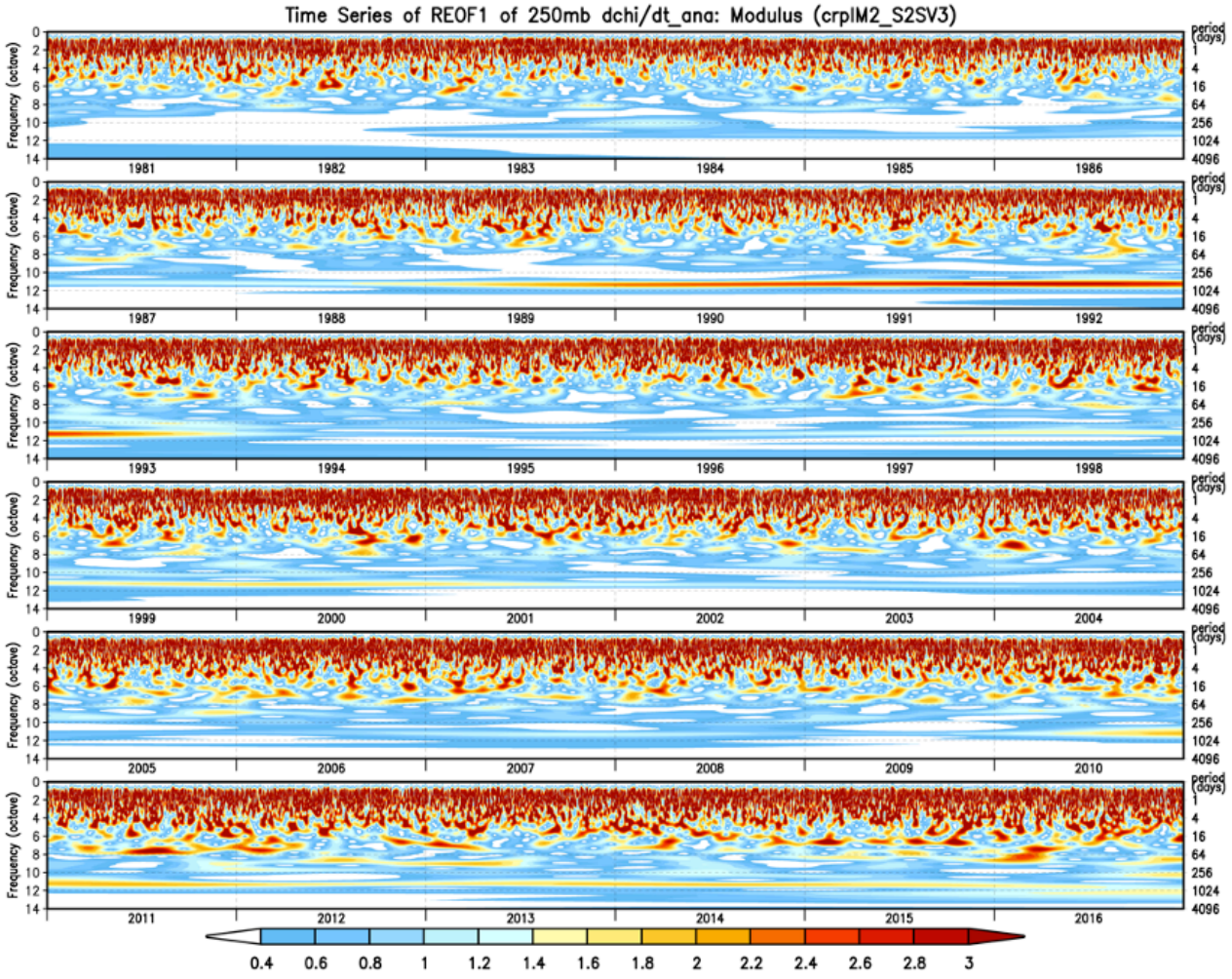

Figure 38: The time series of the modulus of the wavelet decomposition of PC 1 of the 250mb velocity potential increments (see text for details). The results are from the GEOS S2S V3 AOGCM replayed to MERRA-2 for 1981-2016.

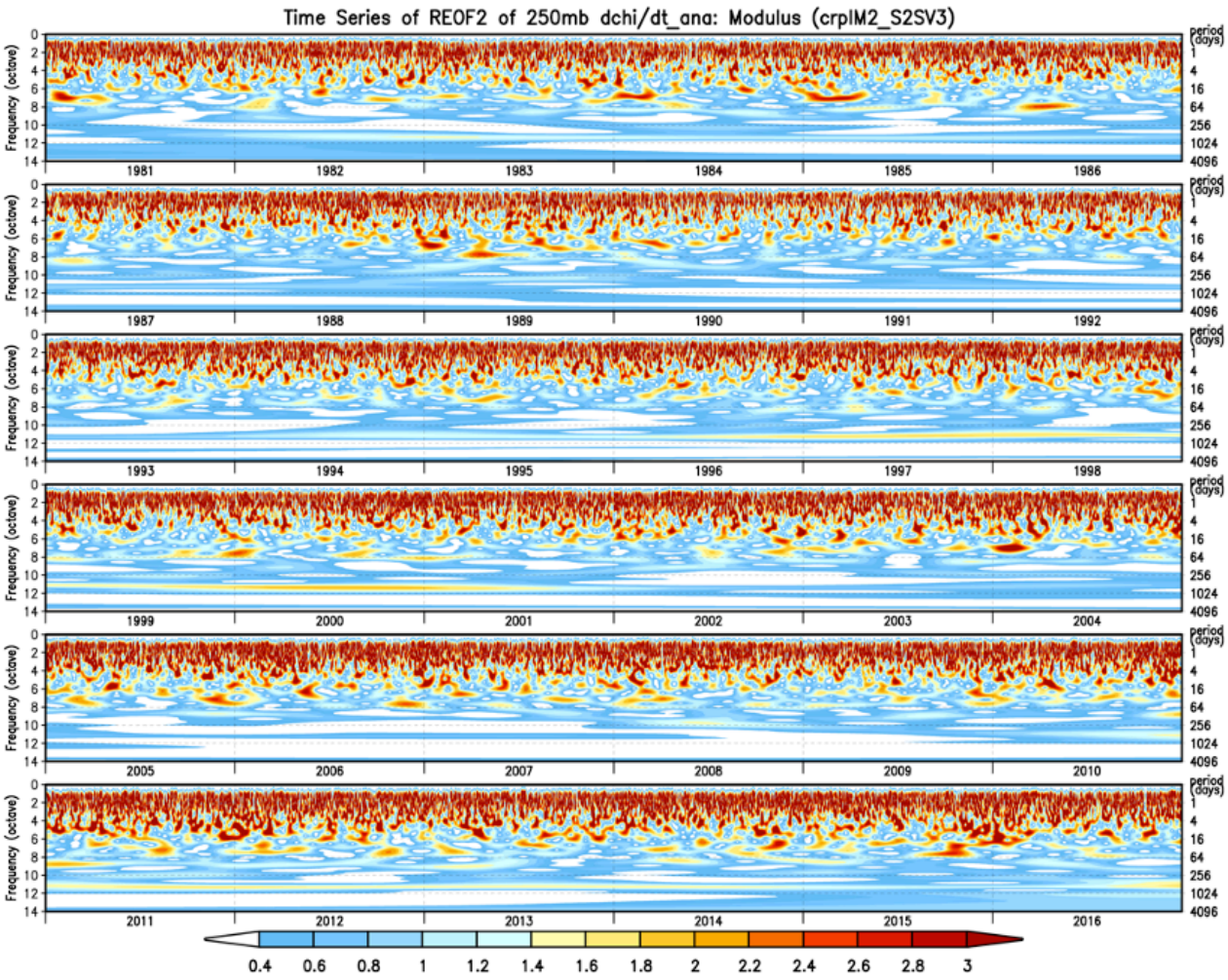

Figure 39: Same as Fig. 38 except for PC 2.

All 5 leading 250mb velocity potential PCs (Fig. 37, right panels) show what appear to be changes in their behavior occurring around 2000, presumably again reflecting the introduction of AMSU and AIRS data around that time. In the case of PC 1 (Fig. 37a) that year marks the node of what appears to be a long-term sinusoidal variation in which the values transition from positive to negative. For PC 2 (Fig. 37b), 2000 marks the beginning of a trend toward more negative values, while for PCs 3 - 5 (Fig. 37c-e), 2000 marks the beginning of a roughly 10-year period of substantially reduced variability in the increments followed by (at around 2011) much increased annual variability. The

much-enhanced annual variability during the late 1980s and early 1990s of PC 3 mentioned above coincides with the period of early NOAA 11 (28 Sep 1988- 04 Dec 1994) MSU/SSU data, though whether this is connected to the enhanced annual variability remains to be confirmed.

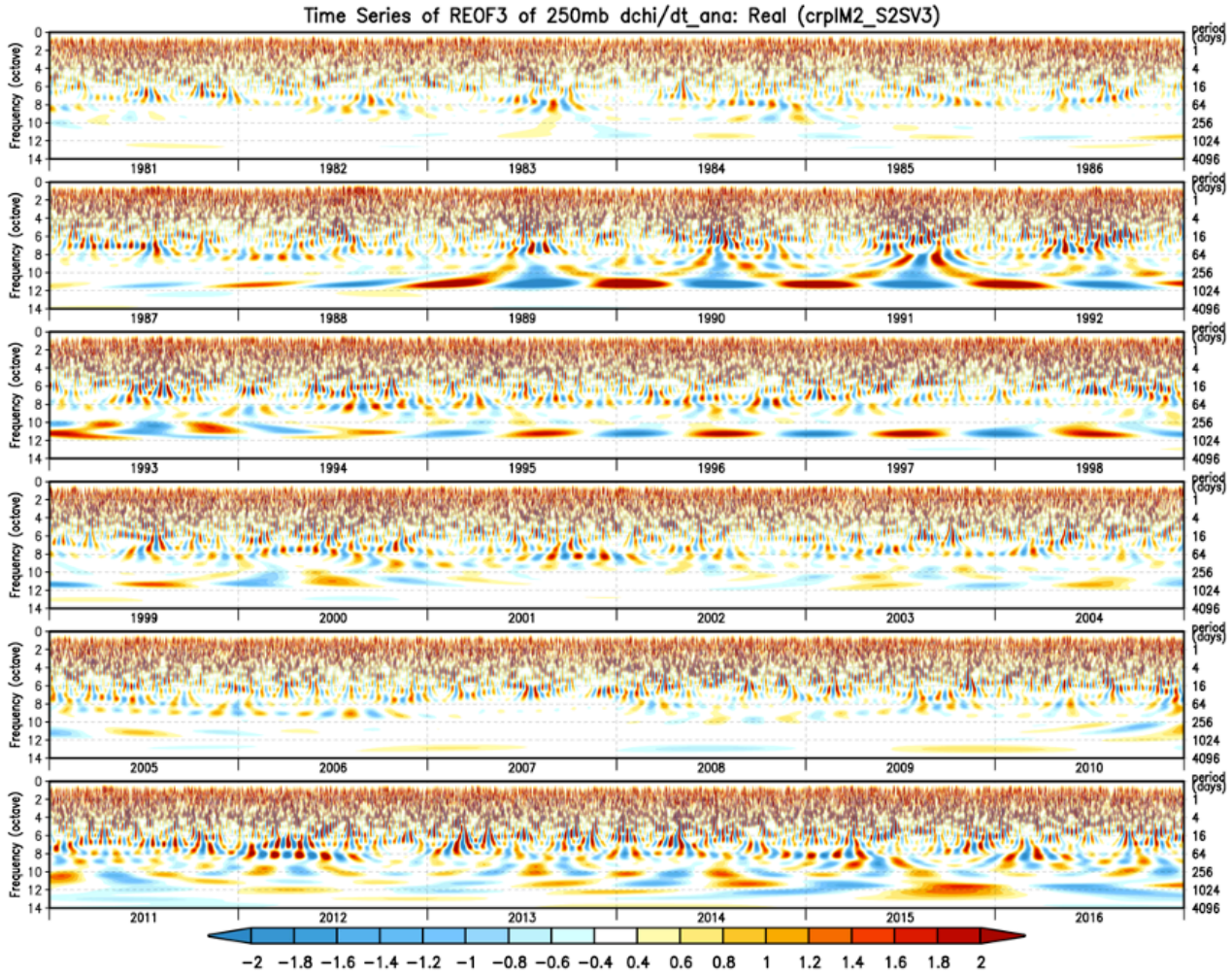

Figure 40: The time series of the real part of the wavelet decomposition of PC 3 of the 250mb velocity potential increments (see text for details). The results are from the GEOS S2S V3 AOGCM replayed to MERRA-2 for 1981-2016.

b) The temperature and moisture

The three leading REOFs of the temperature increments at the lowest model level all tend to have the largest spatial loadings at high latitudes and near land/sea ice boundaries (Fig.41 a-c). REOF 1, characterized by a dipole structure, has the largest loadings over the Ross and Weddell Seas and

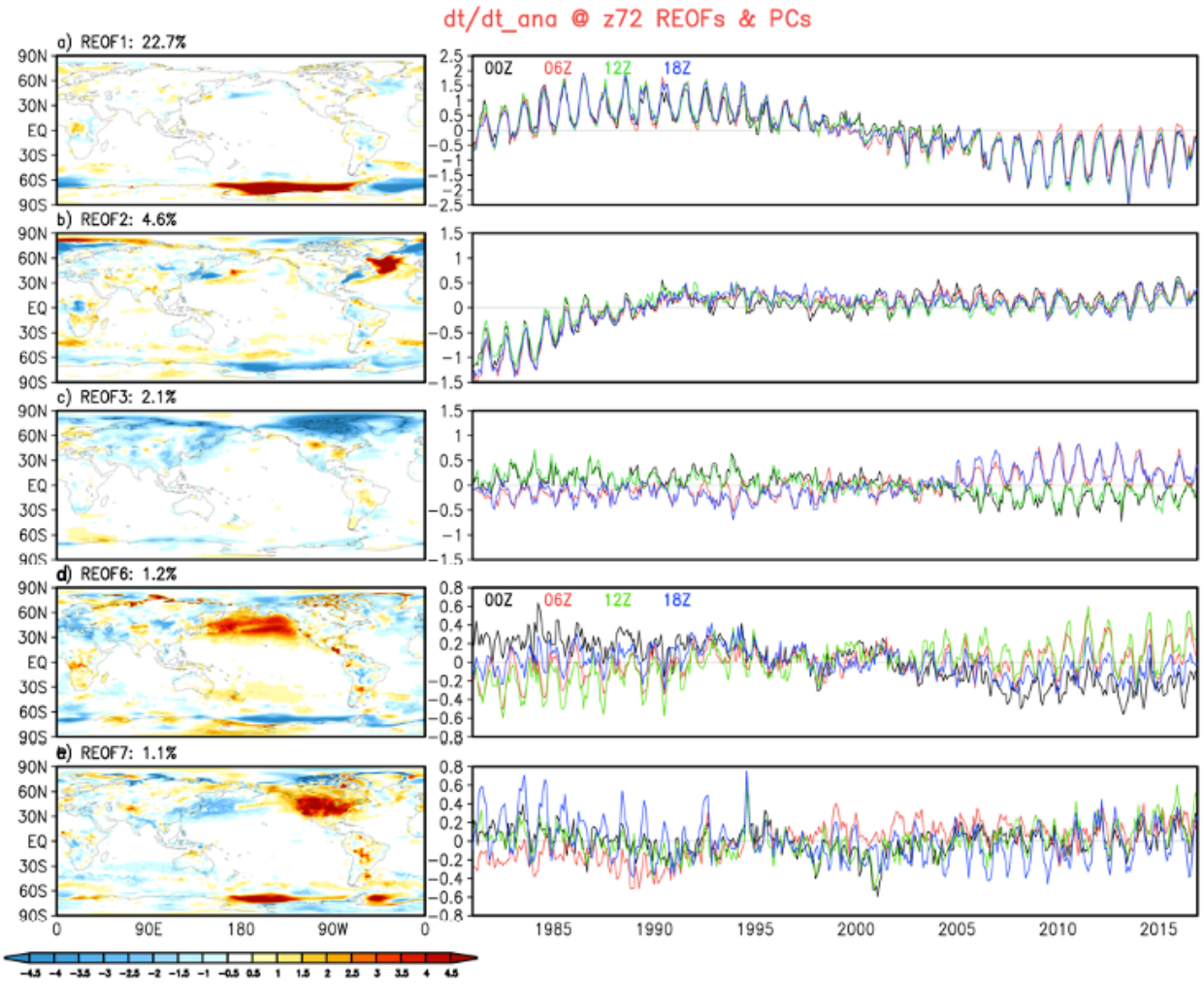

Figure 41: Left panels: the REOFs of the model level 72 (approximately 992mb) temperature increments. Right panels: the associated PCs plotted separately for each time of day. The REOFs were obtained from monthly anomalies that were computed separately for each time of day: 00z, 06z, 12z and 18z. The PCs were obtained by projecting the 6-hourly anomalies (obtained by removing separate 6-hourly climatologies for each time of day) onto the monthly REOFs (see text for details). The results are from the GEOS S2S V3 AOGCM replayed to MERRA-2 for 1981-2016.

accounts for 23% of the monthly variance. The associated PC 1 (Fig. 41a, right panel) shows a pronounced long-term change in both the mean and variance, reflecting to a large extent a 180° phase shift in the annual cycle that occurs in the early 2000's (see the real part of the wavelet transform in Fig. 42), at the same time that there is a minimum in the annual cycle variance.

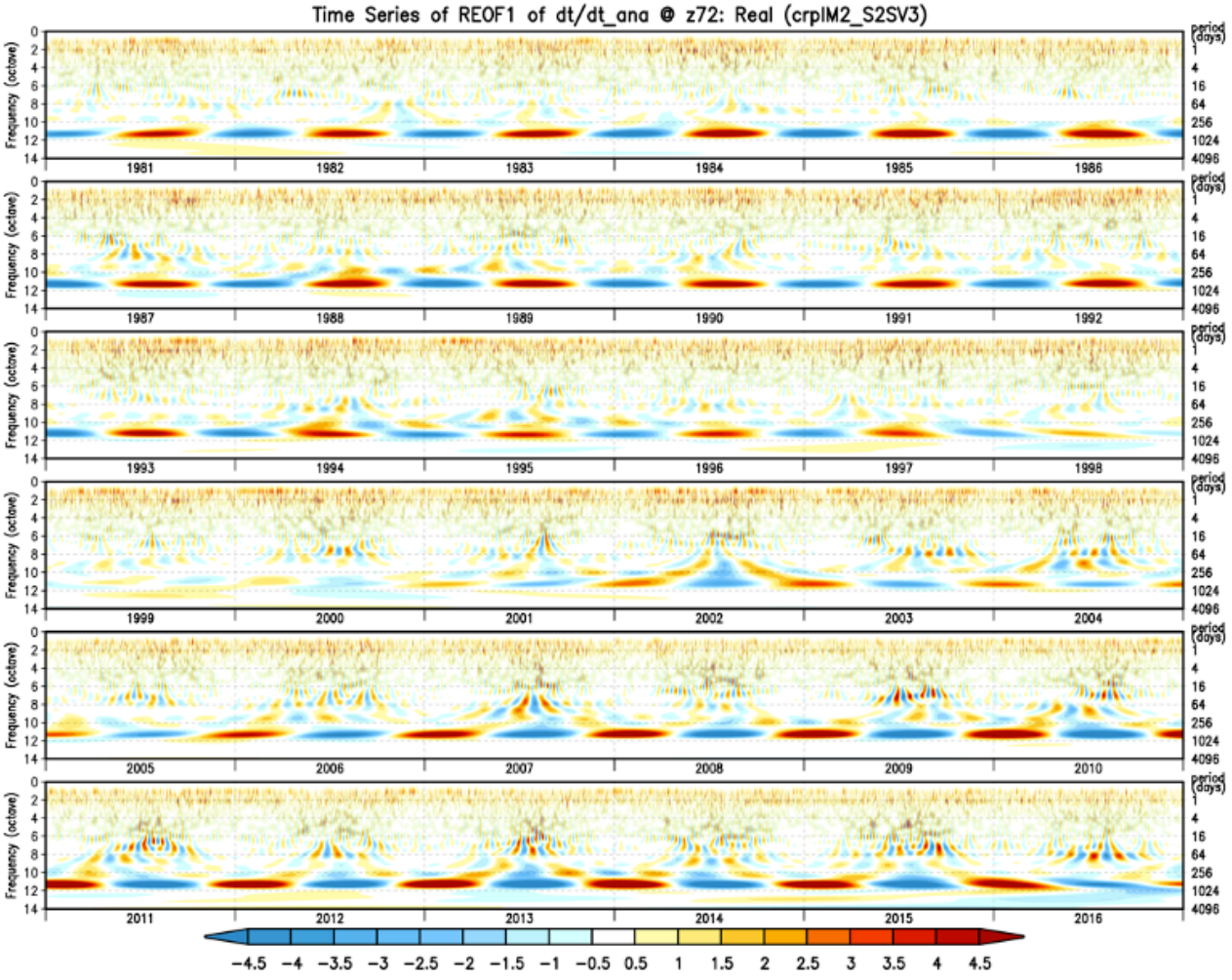

Figure 42: The time series of the real part of the wavelet decomposition of PC 1 of the model level 72 (approximately 992mb) temperature increments (see text for details). The results are from the GEOS S2S V3 AOGCM replayed to MERRA-2 for 1981-2016.

The second REOF (Fig. 40b, left panel) has most of the spatial loading located in the middle and high latitude North Atlantic, encompassing regions that include parts of the Gulf Stream, the North Atlantic subpolar gyre, and the Greenland Sea. The associated PC 2 (Fig. 40b, right panel) shows a gradual increase (starting from relatively large magnitude negative values) to generally small positive values starting at about 1990. This slow change is modulated by an annual cycle which is largest during the early 1980s, almost disappearing around the year 2000, and then increasing again after that. These changes in the annual cycle are reflected in the real part of the wavelet decomposition (Fig. 43) which shows the annual cycle goes through a transition in both intensity and phase during the mid-1990s.

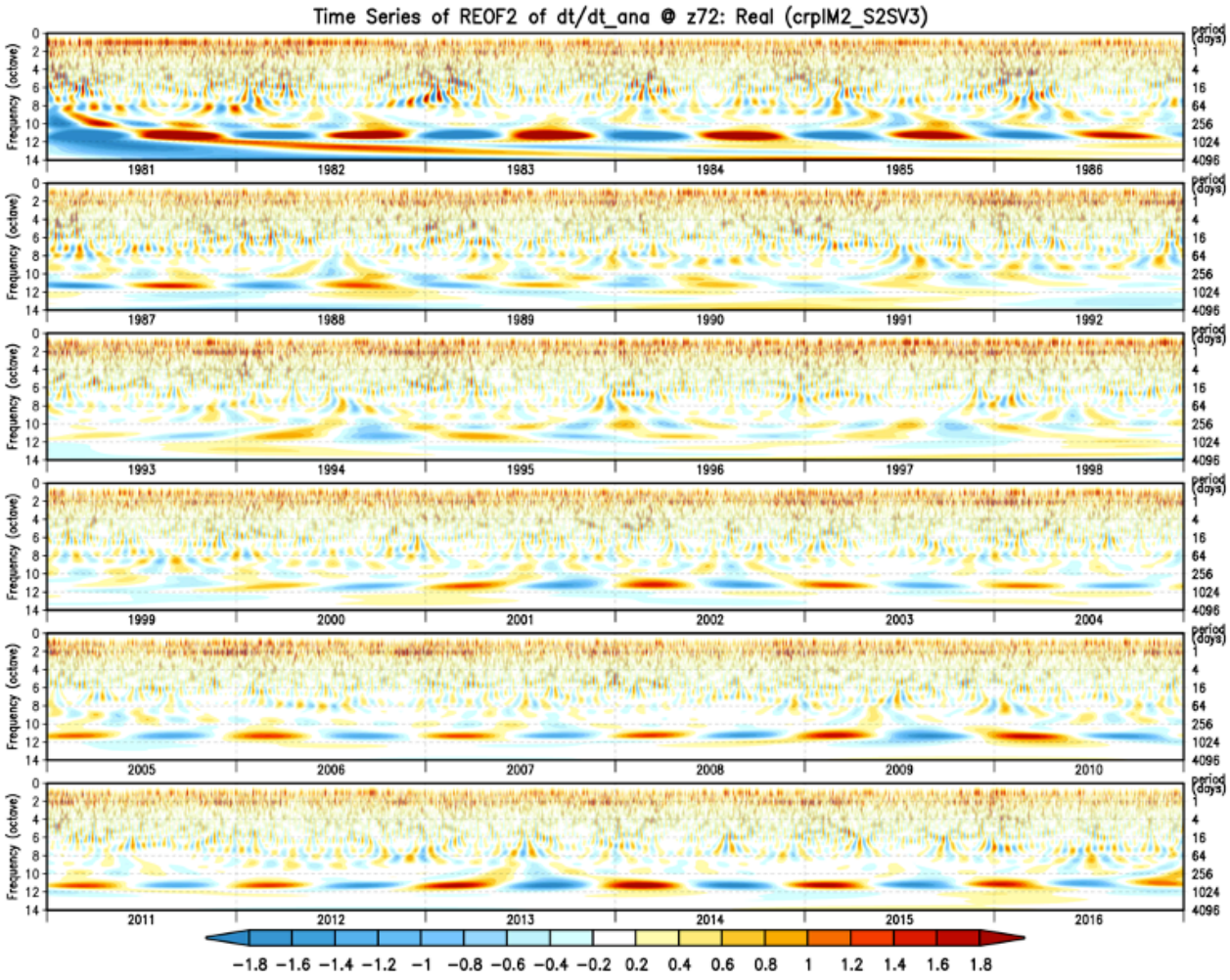

Figure 43: Same as Fig. 42 except for PC 2.

The third REOF (Fig. 41c, left panel) has the largest loadings over the Arctic region. The associated PC (Fig. 41c, right panel) undergoes a rather pronounced transition around the early 2000s. In the earlier period, 00z and 12Z tend to be positive and 06Z and 18Z tend to be negative, while the reverse is true during the later period. These differences in the 00Z/12Z and 06Z/18Z values are reflected in the modulus of the wavelet decomposition as a pronounced semi-diurnal cycle (Fig. 44) that tends to have maximum values during the winter season. REOFs 4 and 5 show large loadings confined to the SH high latitudes along the coast of Antarctica (not shown). Of more interest are REOF 6 (Fig.

41d), which has maximum loadings over the North Pacific, and REOF 7 (Fig. 41e), which has large loadings over North America. The former (PC 6) undergoes a transition in the early 2000s and is especially interesting in that the 00Z and 12Z values tend to be of opposite sign, with the 06Z and 18Z values tending to be somewhere in between. PC 7, rather unexpectedly, has large differences between the 18Z and 06Z values (and these are in turn different from the 00Z and 12Z values), suggesting that the temperature observations over North America during those times of day have substantially different (and inconsistent) values. Exactly why that is the case is unclear since MERRA-2 does not assimilate 2-m temperature from surface stations over land. Nor does it assimilate AIRS/AMSU-A TS data (e.g., Hearty et al. 2018).

The long-term behavior of PC 1 (in particular the reduction in amplitude of the annual cycle) again appears to reflect the introduction of AMSU data in Nov 1998 (McCarty et al. 2016), while the recovery of the annual cycle (though with opposite sign) coincides with the introduction of the NOAA MHS (follow-on to AMSU-B) on 1 Nov 2005, though those channels are primarily sensitive to moisture. Also potentially relevant are the changes in SST and sea ice products used in MERRA-2 on 1 January 2003 and on 1 April 2006 (Gelaro et. al. 2017, Table 3). The long-term behavior of PC 2 appears to reflect differences in the observing system during the first 10 years or so, when the annual cycle is large and the values are primarily negative. The change after the first decade or so coincides with the introduction of NOAA 11 (MSU) data on 08 Nov 1988. The 00Z/12Z values of PC 7 (main loadings over North America, Fig. 41d) show little evidence of any pronounced long-term changes in character. There are, however, pronounced differences in the behavior of the 06Z and 18Z values, in that both appear to undergo a change in predominant sign at about 1995, with the 06Z values tending to oppose (be of opposite sign to) the 18Z values

throughout the record. It is noteworthy that 1995 marks the beginning of the introduction of NOAA 14 (MSU and HIRS-2) data.

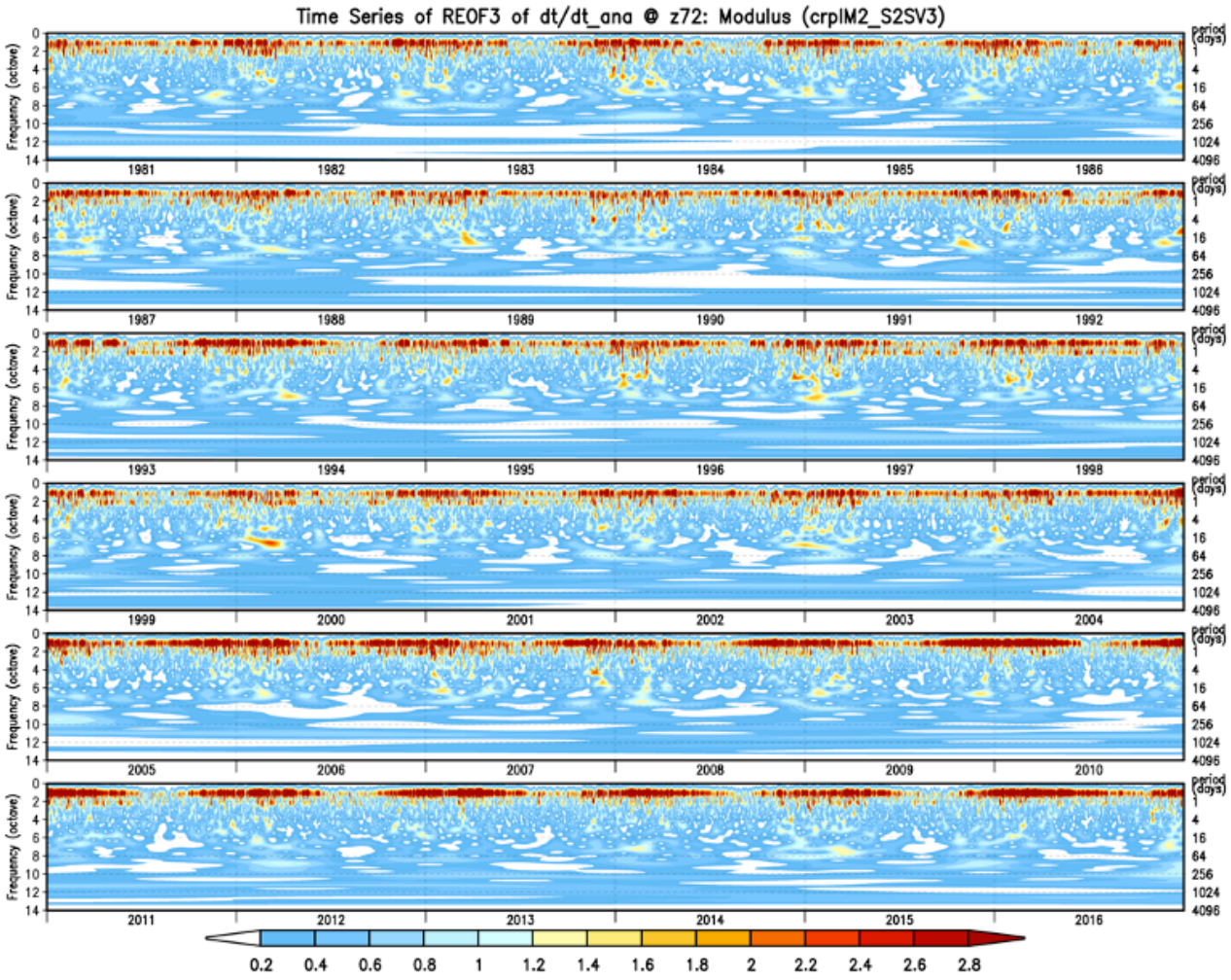

Figure 44: The time series of the modulus of the wavelet decomposition of PC 3 of the model level 72 (approximately 992mb) temperature increments (see text for details). The results are from the GEOS S2S V3 AOGCM replayed to MERRA-2 for 1981-2016.

Figure 45 (left panels) shows the five leading REOFs of the 250mb temperature increments. These consist of patterns localized over northeastern Eurasia/Arctic (REOF 1), over North America (REOF 2), over the SH just south of Africa (REOF 3), over the middle and high latitude South Pacific (REOF 4), and over the high latitude South Atlantic/Antarctica (REOF 5). All five again show periods of

pronounced differences in the PC values for the different times of the day during the early period (roughly prior to and including the year 2000, right panels of Fig 45). For example, the PC 1 values show especially large differences during the different times of the day during the 1990s (Fig. 45a, right panel), which are reflected in the wavelet modulus as pronounced semi-diurnal and diurnal

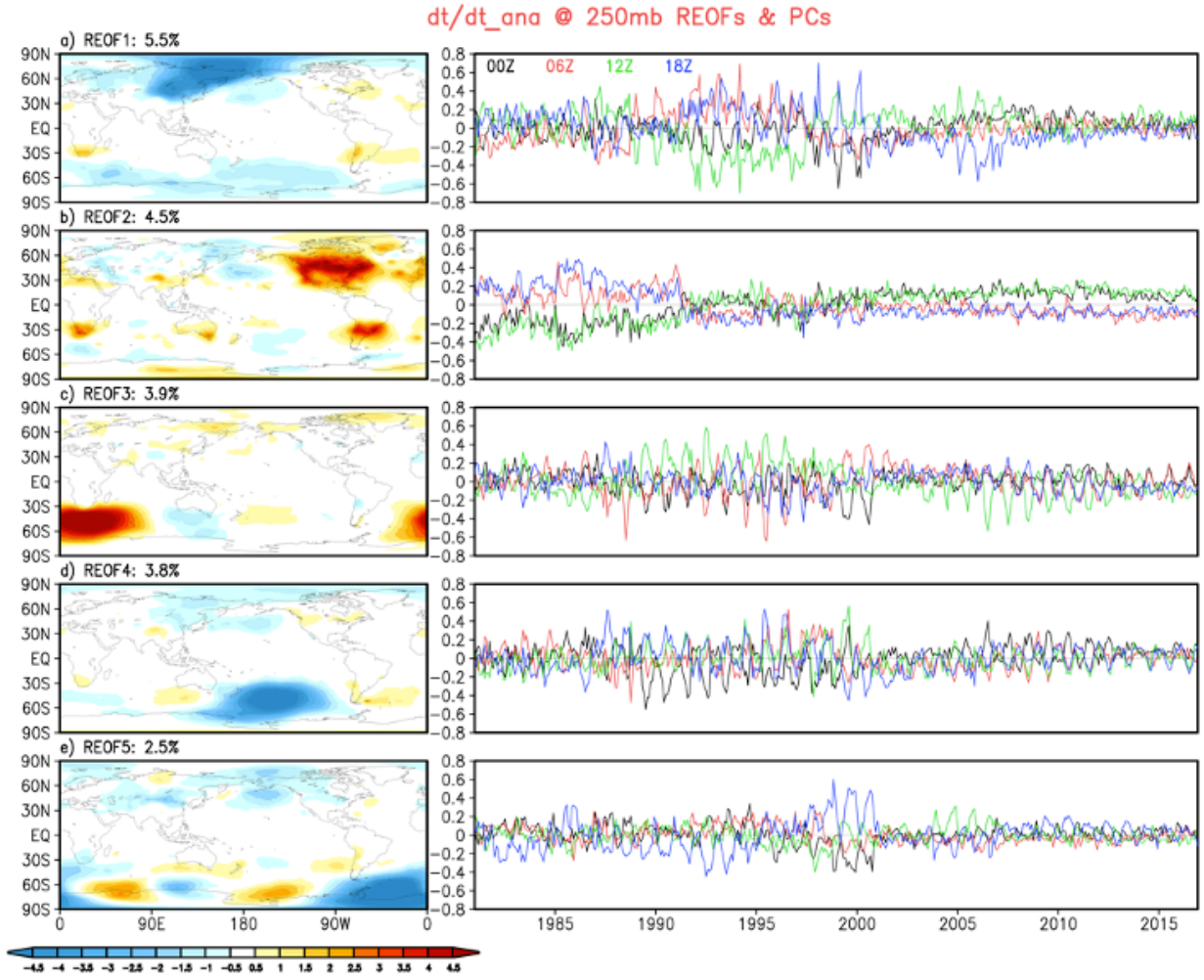

Figure 45: Left panels: the REOFs of the 250mb temperature increments. Right panels: the associated PCs plotted separately for each time of day. The REOFs were obtained from monthly anomalies that were computed separately for each time of day: 00z, 06z, 12z and 18z. The PCs were obtained by projecting the 6-hourly anomalies (obtained by removing separate 6-hourly climatologies for each time of day) onto the monthly REOFs (see text for details). The results are from the GEOS S2S V3 AOGCM replayed to MERRA-2 for 1981-2016.

cycles during that time (Fig. 46). In the case of PC 2, the differences are largest through about 1991 (the 00Z/12Z values tend to be negative, and the 06Z/18Z values tend to be positive), after which the 00Z/12Z values tend to be relatively small but positive, while the 06Z/18Z values tend to be small but negative, especially after about the year 2000. This is reflected in the wavelet modulus (Fig. 47) as a pronounced semi-diurnal signal during the 1980s and early 1990s. PC 3 is interesting in that the semi-diurnal and diurnal cycles tend to be largest during the SH winter (Fig. 48), and it has an annual cycle (especially in the 12Z values, Fig. 45c right panel) that switches sign at about 2000 (real part of the wavelet, not shown). Similarly, PC 4 (wavelet transform not shown) also has semi-diurnal and diurnal cycles that tend to be largest during the SH winter.

In summary, all five leading PCs of the 250mb temperature increments show a distinct change in character at about 2001/02, characterized by generally large annual cycles and sharply different behavior between the 00Z/12Z and 06Z/18Z values in the early period, followed by much reduced variability during the later period. This transition again roughly corresponds with the introduction of NASA EOS AMSU-A and AIRS radiance data in September 2002. In the case of PC 2 (Fig. 45b), the pronounced change that occurs at about 1992 appears to coincide with the introduction of NOAA 12 radiances in 18 August 1991.

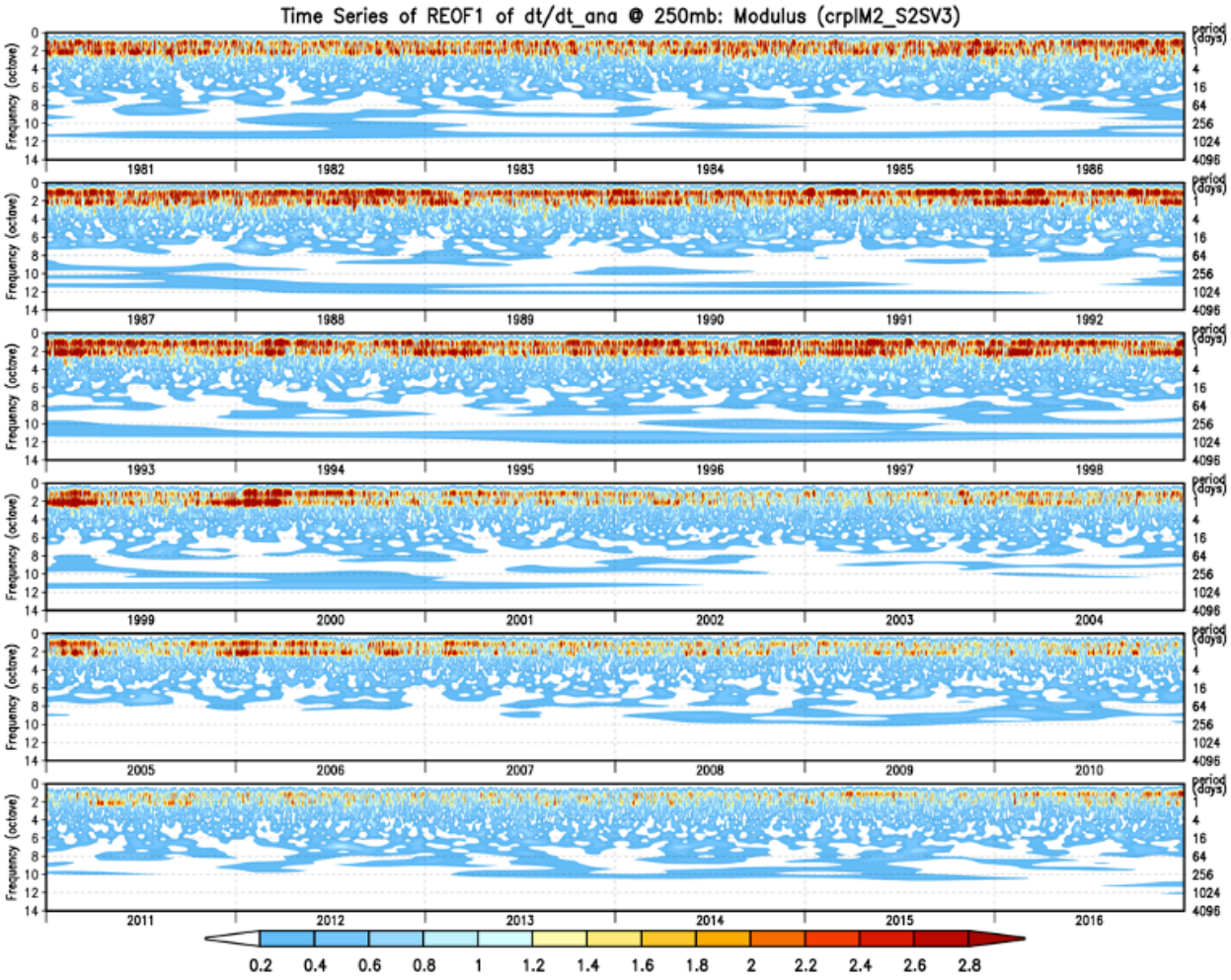

Figure 46: The time series of the modulus of the wavelet decomposition of PC 1 of the 250mb temperature increments (see text for details). The results are from the GEOS S2S V3 AOGCM replayed to MERRA-2 for 1981-2016.

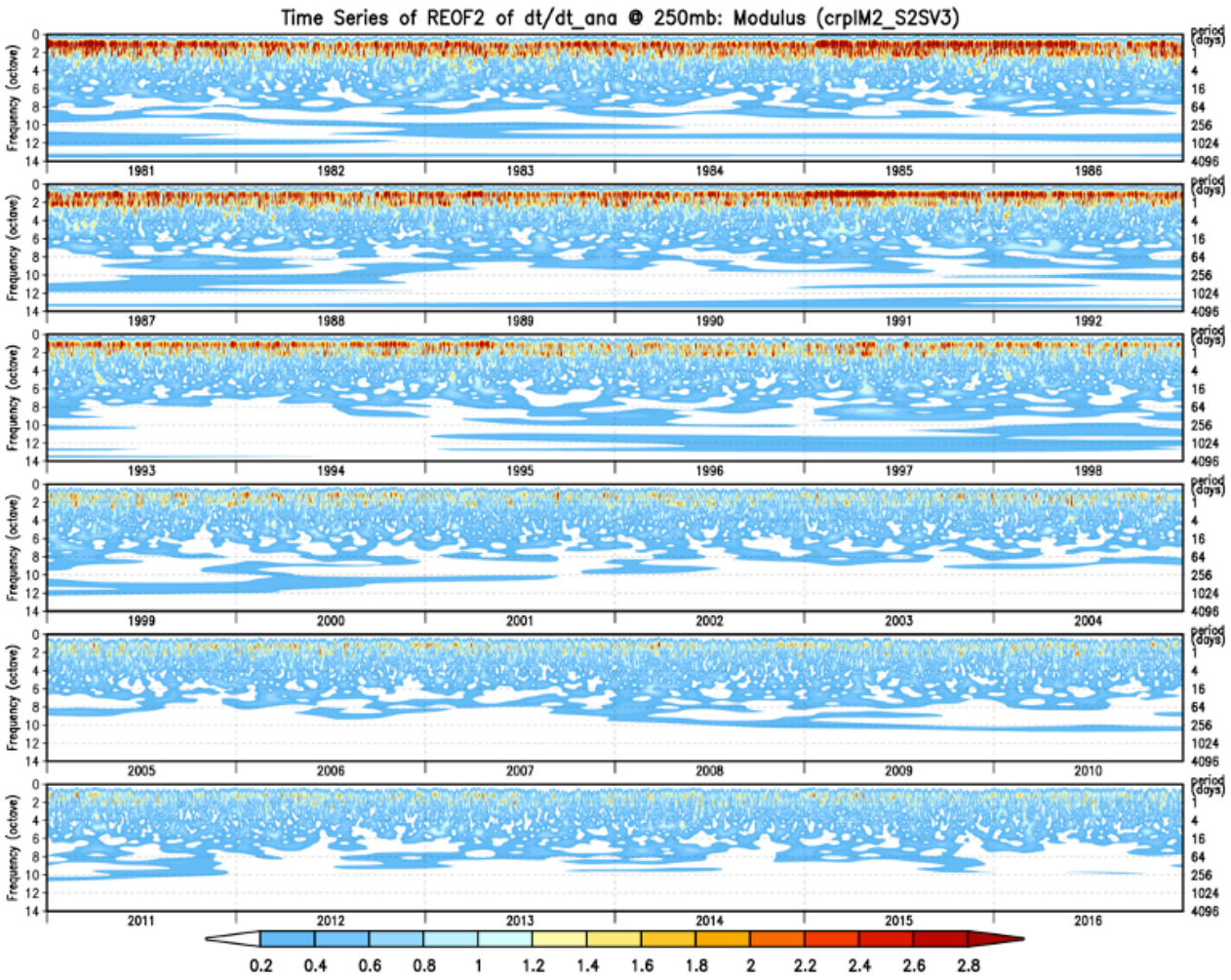

Figure 47: Same as Fig. 46 except for PC2.

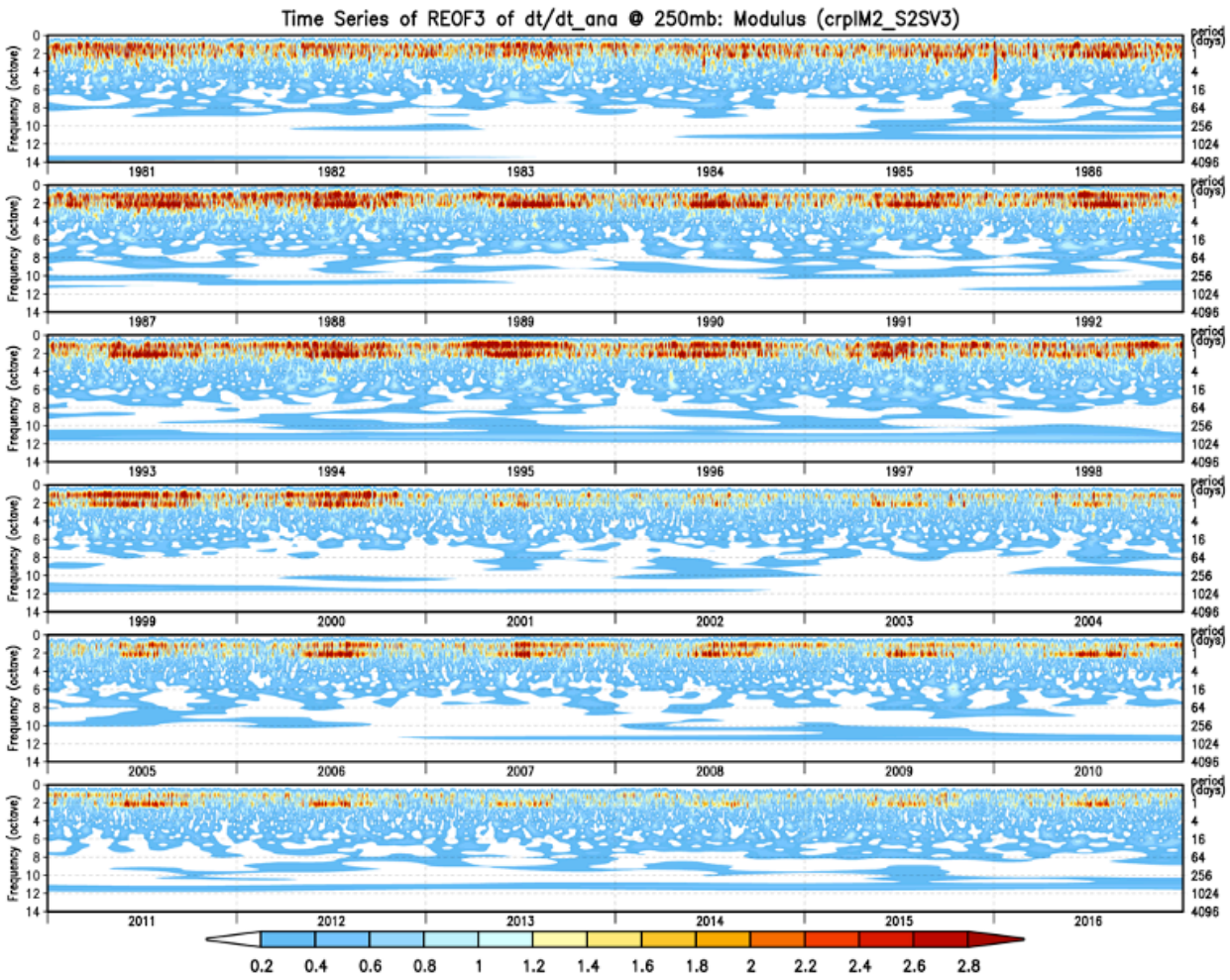

Figure 48: Same as Fig. 46 except for PC 3.

The five leading PCs of the near surface moisture increments (Fig. 49) all show substantial long-term and, in some cases, abrupt changes in behavior. PC 1 (Fig. 49a) has the same long-term behavior that we already saw for the PC 1 of the near surface temperature (a 180° phase shift in the annual cycle over the Ross and Weddell Seas beginning around 2000, see Fig. 50). As we already noted, the reduction in amplitude appears to coincide with the introduction of AMSU data in Nov 1998 (McCarty et al. 2016), while the recovery of the annual cycle (though with opposite sign) coincides with the introduction of the NOAA MHS in Nov 2005. Also, again potentially relevant, are the

changes in SST and sea ice products used in MERRA-2 on 1 January 2003 and on 1 April 2006 (Gelaro et. al. 2017, Table 3). PC 2 (Fig. 49b, central tropical Pacific dipole straddling the equator)

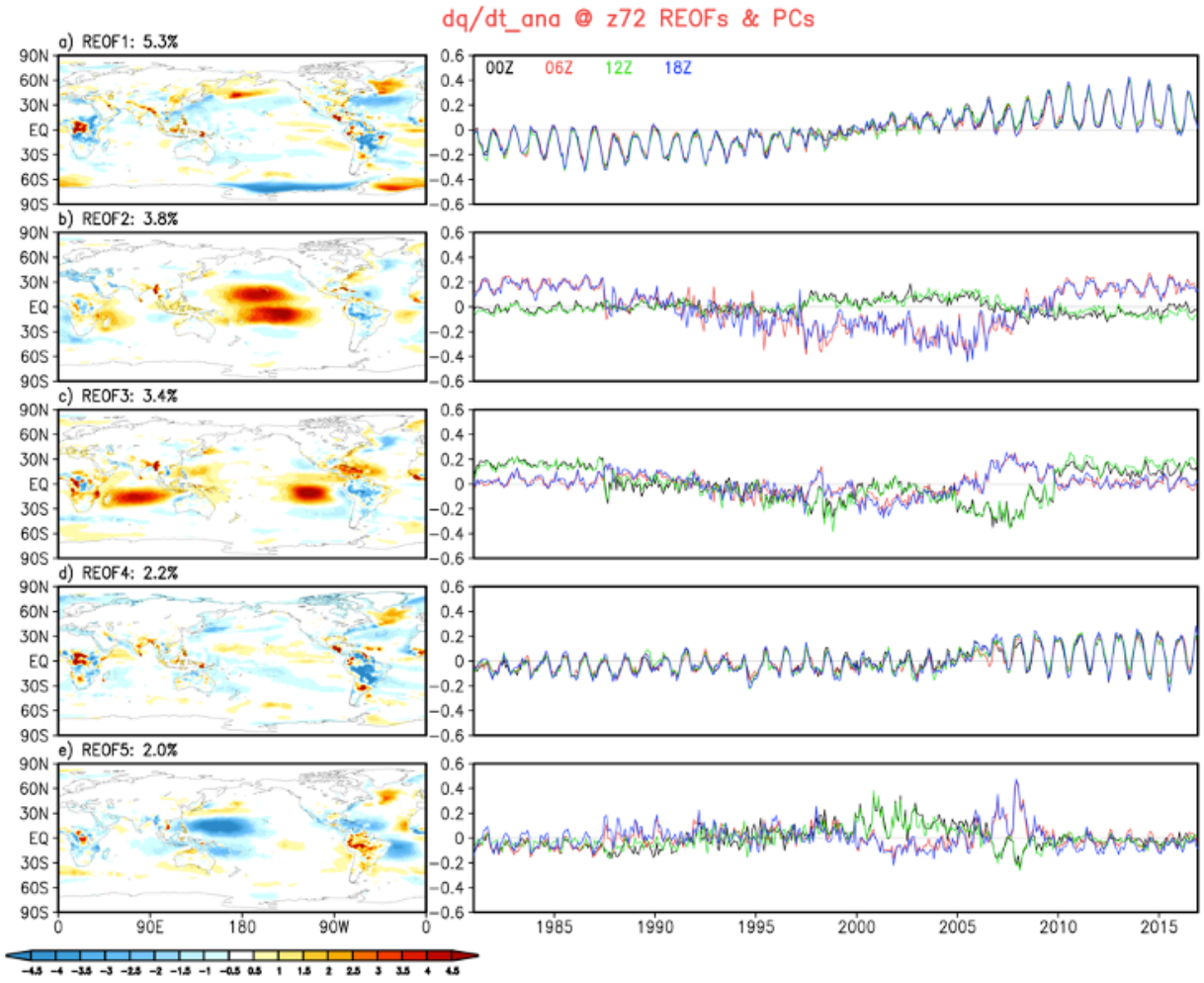

Figure 49: Left panels: the REOFs of the model level 72 (approximately 992mb) specific humidity increments. Right panels: the associated PCs plotted separately for each time of day. The REOFs were obtained from monthly anomalies that were computed separately for each time of day: 00z, 06z, 12z and 18z. The PCs were obtained by projecting the 6-hourly anomalies (obtained by removing separate 6-hourly climatologies for each time of day) onto the monthly REOFs (see text for details). The results are from the GEOS S2S V3 AOGCM replayed to MERRA-2 for 1981-2016.

has long term changes as a result of the changes in the 06Z/18Z values (see the semi-diurnal and diurnal cycles, Fig. 51). That PC has a similar behavior before 1988 and after 2010 with generally positive values for 06Z/18Z and essentially zero (or slightly negative) values for 00Z/12Z. Possible

relevant changes in the observations include the introduction of NOAA 11 on 28 Sep 1988 and the use of SSM/I wind speed during 9 July 1987 – 29 Oct 2013. Between 1997 and 2007 the behavior of PC 2 is opposite to that of the other periods in that 06Z/18Z values are negative, with slightly positive values for 00Z/12Z. PC 3 (Fig. 49c, largest loadings in the SH tropical Indian Ocean and eastern Pacific) exhibits somewhat similar behavior to PC 2 but with opposite sign. PC 4 (Fig. 49d, largest loadings over South America) exhibits an increase in the annual cycle after about 2007 (here

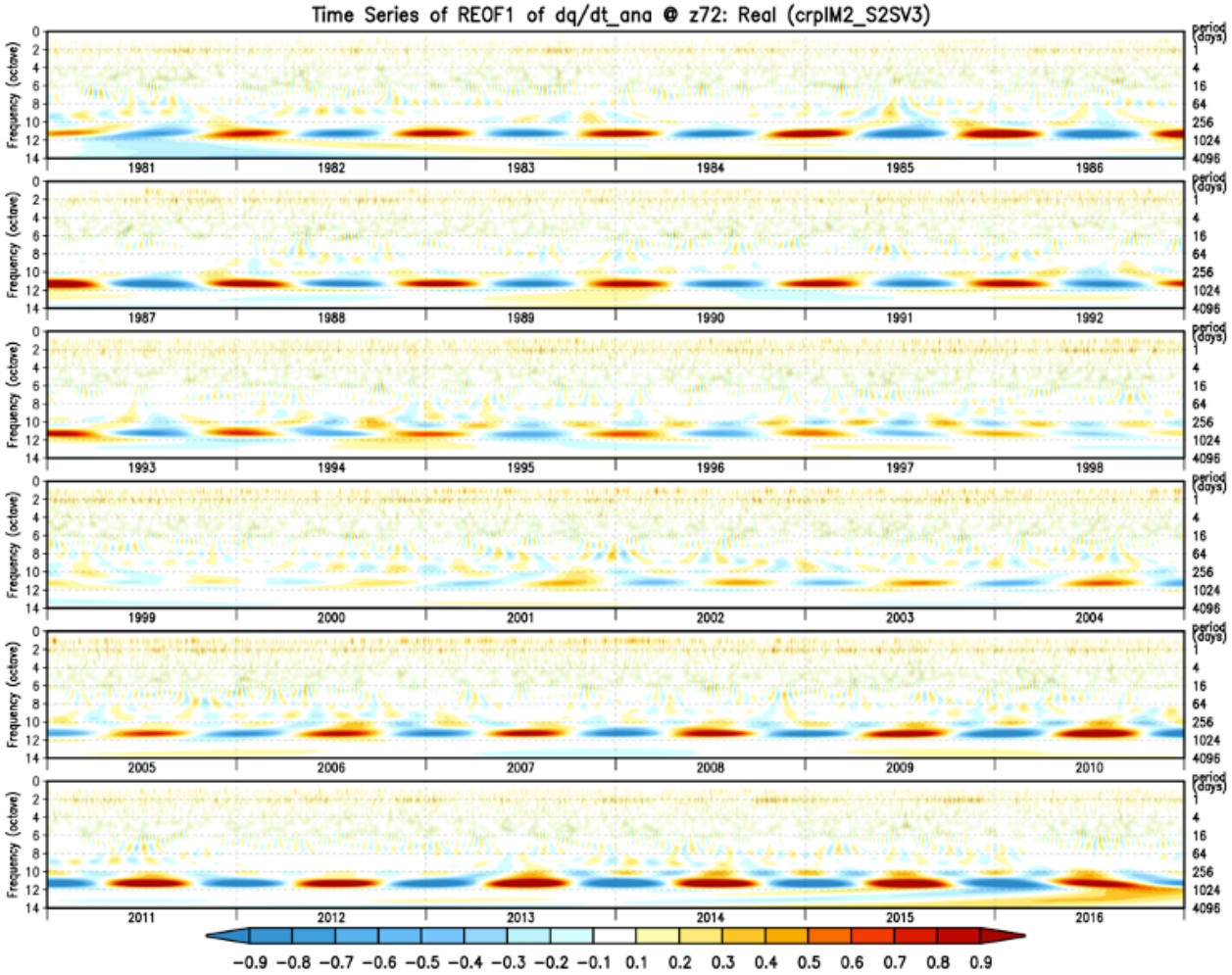

Figure 50: The time series of the real part of the wavelet decomposition of PC 1 of the model level 72 (approximately 992mb) specific humidity increments (see text for details). The results are from the GEOS S2S V3 AOGCM replayed to MERRA-2 for 1981-2016.

we note the introduction of Metop-A data on 21 May 2007). PC 5 (Fig. 49e, with largest loadings in the western subtropical regions of the Pacific and Atlantic Oceans) shows the largest differences between 06Z/18Z and the 00Z/12Z values between about 2000 and 2008.

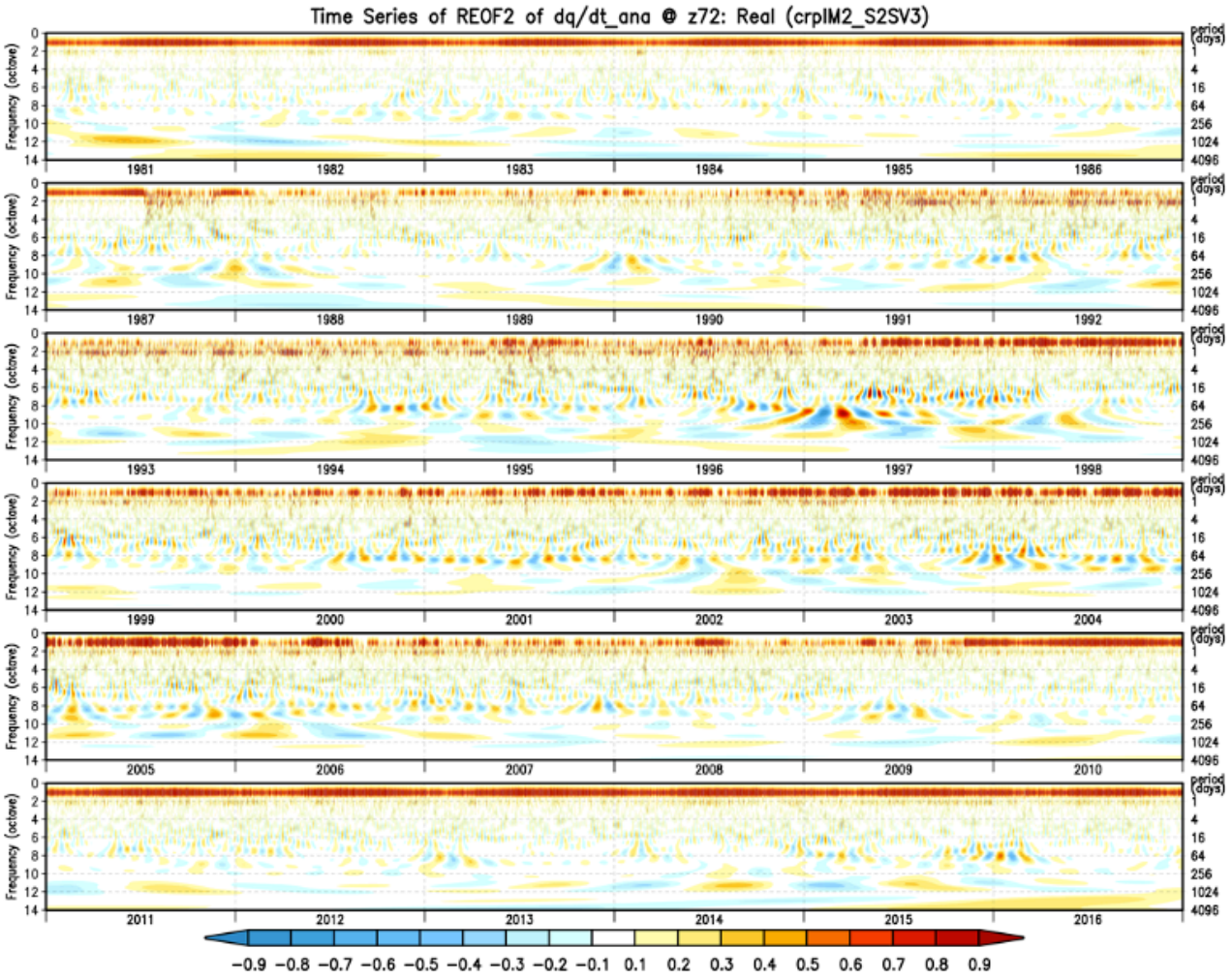

Figure 51: Same as Fig. 50 except for PC 2.

Figure 52 shows the five leading REOFs of the moisture increments at model level 63. REOF 1 (left panel of Fig. 52a), with maximum loading in the central tropical Pacific, appears to have pronounced variability on a wide range of time scales (right panel of Fig. 52a), with little evidence for a substantial impact on the variability of the associated PC from changes in the observing system. This is clearly

evident from the real part of the wavelet decomposition in Fig. 53. In fact, as we shall see, PC 1 has a substantial negative correlation with Niño3.4 (see Fig. 64h). Similarly, REOF 4, with maximum loading just to the east of REOF 1, also has pronounced variability at subseasonal and longer time scales (right panel of Fig. 52d, and Fig. 54). In this case (PC 4), it turns out that the largest (negative) correlations are with the PDO (see Fig. 64h).

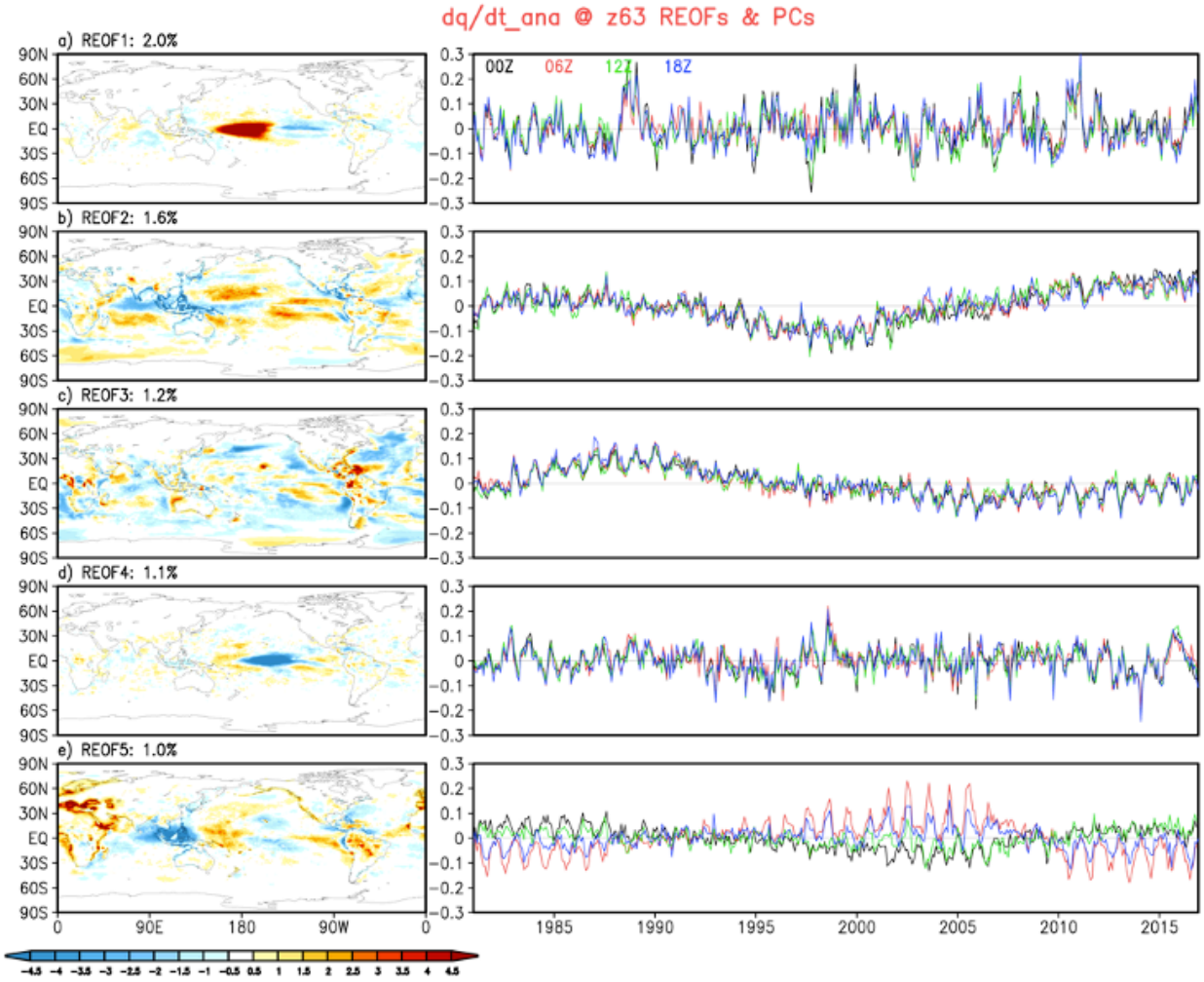

Figure 52: Left panels: the REOFs of the model level 63 (approximately 857mb) specific humidity increments. Right panels: the associated PCs plotted separately for each time of day. The REOFs were1 obtained from monthly anomalies that were computed separately for each time of day: 00z, 06z, 12z and 18z. The PCs were obtained by projecting the 6-hourly anomalies (obtained by removing separate 6-hourly climatologies for each time of day) onto the monthly REOFs (see text for details). The results are from the GEOS S2S V3 AOGCM replayed to MERRA-2 for 1981-2016.

In contrast, both REOFs 2 (Fig. 52 b) and 3 (Fig. 52 c) show very low frequency changes that are likely the result of long-term changes in the observing system. Also, the fact that the variability of REOF 5 (Fig. 52e) is dominated by the differences between the 06/18Z and the 00Z/12Z values is almost certainly a reflection of the differences in the observations for the different times of the day.

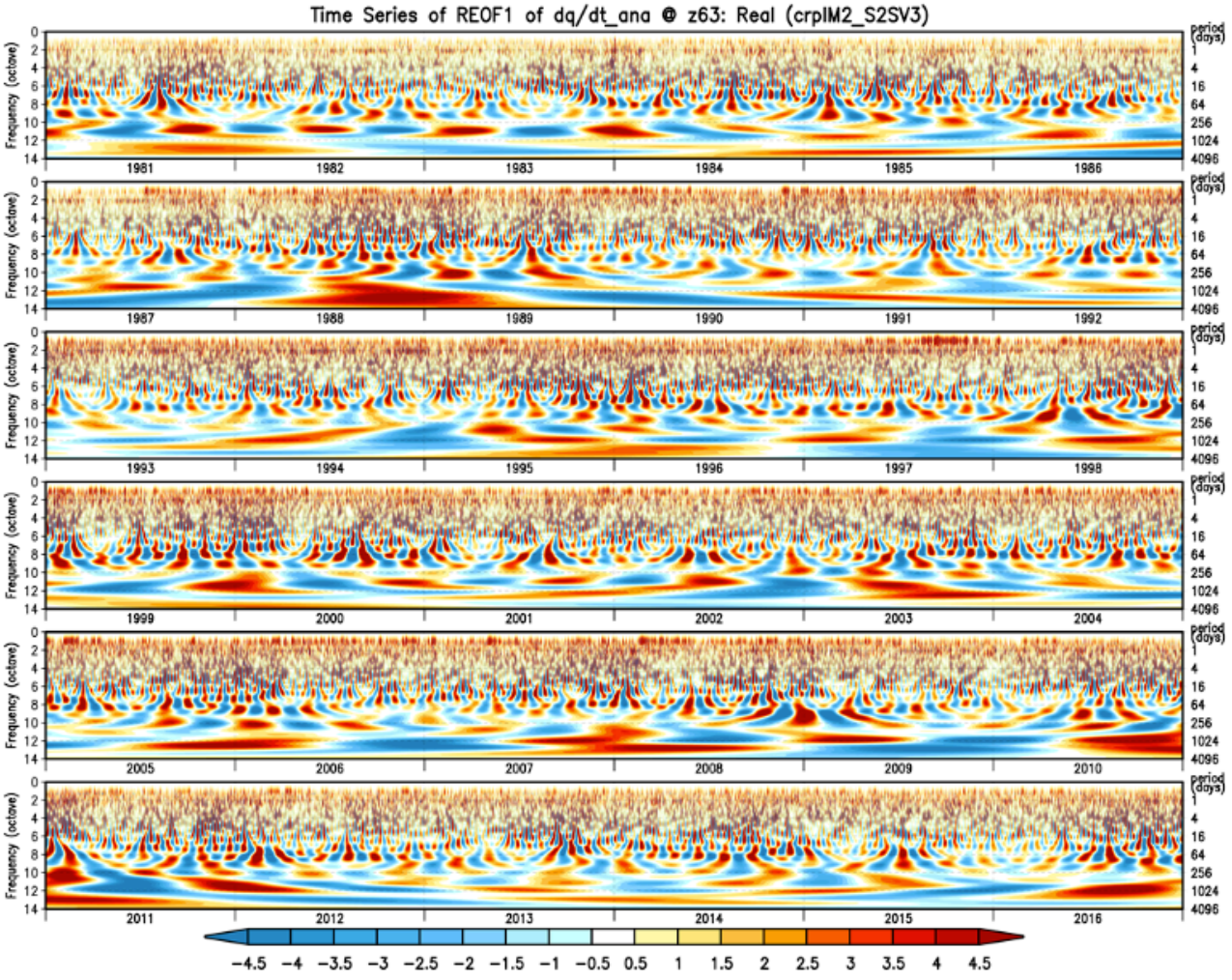

Figure 53: The time series of the real part of the wavelet decomposition of PC 1 of the model level 63 (approximately 857mb) specific humidity increments (see text for details). The results are from the GEOS S2S V3 AOGCM replayed to MERRA-2 for 1981-2016.

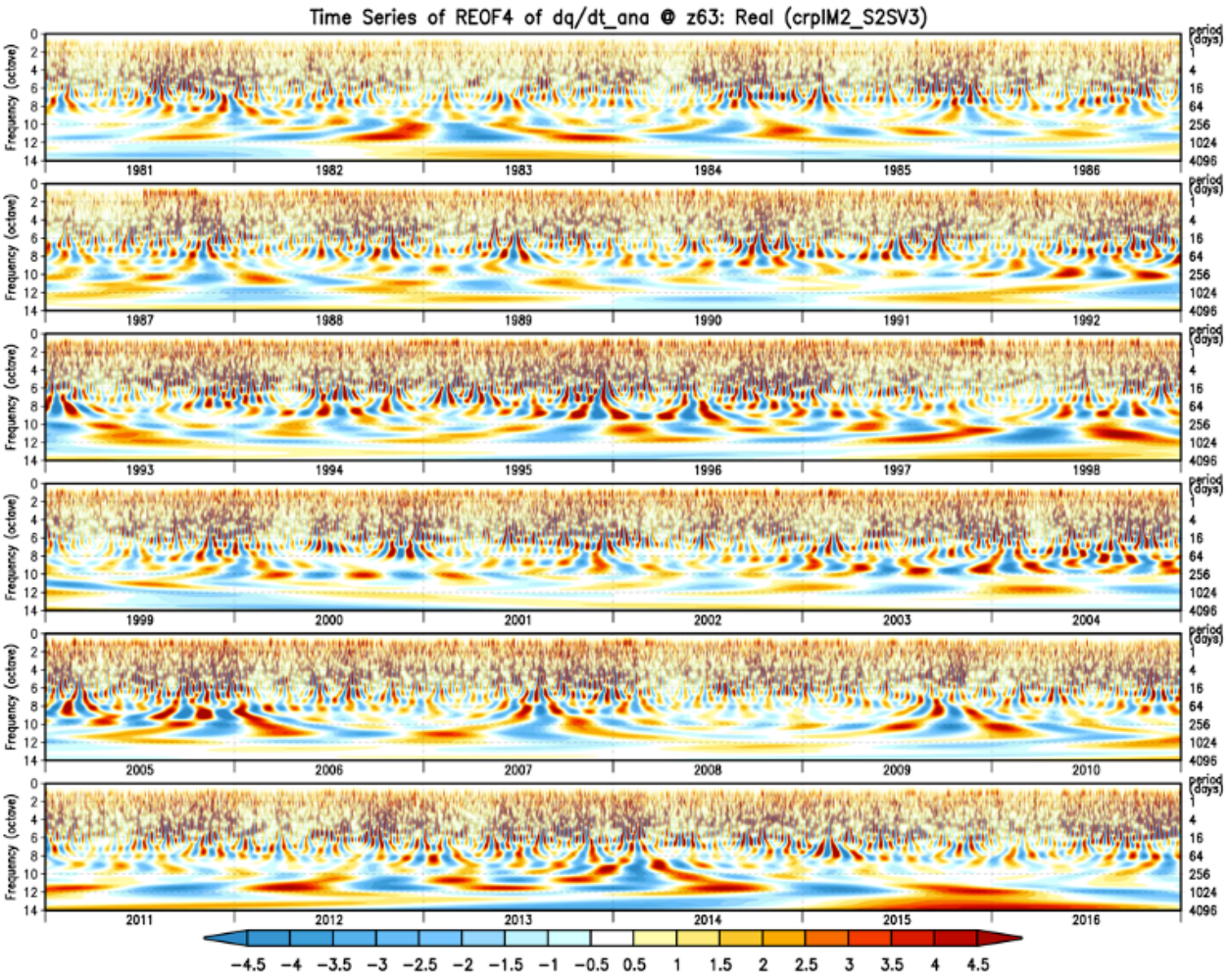

Figure 54: Same as Fig. 53 except for PC 4.

3.3 Correlations with atmospheric/oceanic phenomena

In assessing these correlations, we remind the reader that one of our key goals is to extend the TBC methodology of Chang et al. (2019) by including some type of state-dependence to the correction terms. This could be done simply, for example, by compositing the increments on specific climate phenomena (e.g., ENSO) or, more generally, by modeling the time variability of the increments to include a linear dependence on the state variables (e.g., Chang et al. 2021). In any event, in order to

justify doing this, we need to be able to show that the increments do indeed have some dependence on the climate state. To do that we focus next on determining whether the increments show any dependencies on some of the leading modes of atmospheric and ocean (SST) variability on monthly time scales.

In particular, we examine the correlations between the monthly mean analysis increments and the Antarctic Oscillation (AAO), the Arctic Oscillation (AO), the North Atlantic Oscillation (NAO), the Pacific North American (PNA) pattern, the Pacific Decadal Oscillation (PDO), and the El Niño/Southern Oscillation (ENSO; here we use the Niño3.4 index). The atmospheric indices (AAO, AO, NAO and PNA) were obtained as the leading REOFs of atmospheric height variability based on monthly ERA5 data from 1981-2016 (the choice of height levels used to compute the REOFs varies, but it is consistent with those used by NOAA/CPC[2], see Figure captions). The PDO was obtained using the monthly NOAA Extended Reconstructed Sea Surface Temperature (ERSST) data for the period 1981-2016, and for ENSO, we take NOAA's monthly Niño3.4 index[3].

We take two different approaches to computing the correlations. First, we simply correlate the above climate indices with the monthly mean analysis increments over the entire globe to produce spatial maps of correlations. Second, we produce tables of the correlations between these climate indices and the leading REOFs of the analysis increments examined previously. The second approach, by focusing on the leading modes of the analysis increments, is more likely to show little or no linkages with the climate modes since, as we have seen in the previous section, many of those leading modes of variability in the analysis increments appear to be linked to changes in the observing system. The

[2] https://www.cpc.ncep.noaa.gov/products/precip/CWlink/daily_ao_index/history/method.shtml
[3] https://www.cpc.ncep.noaa.gov/data/indices/sstoi.indices

first approach effectively isolates that part of the increment variability linked to those climate modes, and we can interpret the square of the correlation as the fraction of the monthly mean variability of the increments explained by the climate modes. In both of the above approaches, we remove the monthly mean annual cycle before computing the correlations, and we include all months of the year in computing the correlations. While we have not detrended the increment time series, we shall see in Figures 55-60 that none of the climate indices show evidence of a trend, and so the correlations with those indices will not be contaminated by a trend.

We also examine whether the increments show any dependence on the phase of the MJO (Figs. 61-63). The MJO is isolated using EOFs based on daily MERRA-2 data for the period 1980-2018 and, in order to more efficiently represent traveling disturbances, they are computed as complex EOFs (they are also rotated and are hereafter referred to as RCEOFs). Chang et al. (2001) provide details about the complex EOF calculation. Also, rather than correlations, we employ a compositing approach (based on the magnitudes of the RCEOFs for period 1981-2016) to quantify the dependence of the increments on the phase of the MJO.

Figure 55 shows the results for the AAO, which turns out to be the leading REOF of the monthly 700mb height field in the SH (the middle panels show the REOF and the time series of the associated principal component, or PC, for the period 1981-2016). The top left panels of Fig. 55 show substantial correlations (absolute values greater than 0.3) with the velocity potential increments south of about 60°S at both the surface (positive values) and 250mb (negative values). Considering the implications for state-dependent model error, these results indicate that during the positive phase of the AAO, the model tends to overestimate the 250mb velocity potential anomalies

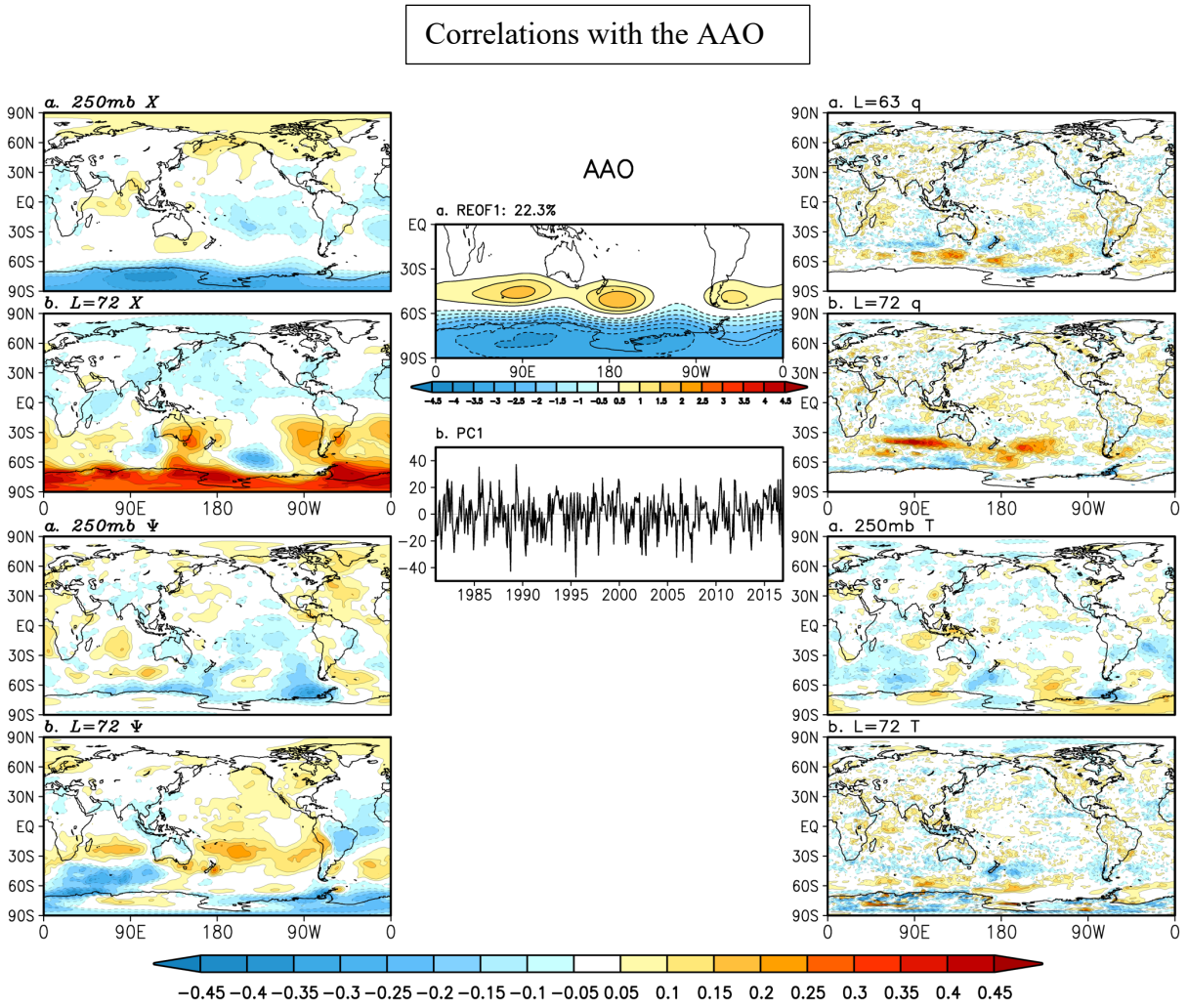

Figure 55: Middle panels: (a) The Antarctic Oscillation (AAO) determined here as the first REOF (22% explained variance) of the SH 700mb mean height using monthly ERA5 data for the period 1981-2016, and (b) the associated PC time series. Top left panels: the correlations between the AAO and a) the 250mb velocity potential increments, and b) the model level 72 (approximately 992mb) velocity potential increments. Bottom left panels: the correlations between the AAO and a) the 250mb stream function increments, and b) the model level 72 (approximately 992mb) stream function increments. Top right panels: the correlations between the AAO and a) the model level 63 (approximately 992mb) specific humidity increments, and b) the model level 72 (approximately 992mb) specific increments. Bottom right panels: the correlations between the AAO and a) the 250mb temperature increments, and b) the model level 72 (approximately 992mb) temperature increments.

south of about 60°S, while near the surface the anomalies tend to be underestimated. Somewhat weaker correlations also occur with the stream function especially near the surface (bottom left panel b) extending into the middle latitudes of the SH. Correlations with the q and T increments tend to be

noisy and weak, with some locally larger positive correlations occurring for q near the surface in the middle latitudes of the SH (Fig. 55, top right panel b).

Figure 56 shows the results for the AO, which shows up clearly as the leading REOF of the monthly 1000mb height field in the NH (middle panels again show the REOF and the associated PC). Relatively large correlations (absolute values greater than 0.3) are found in the NH for both the

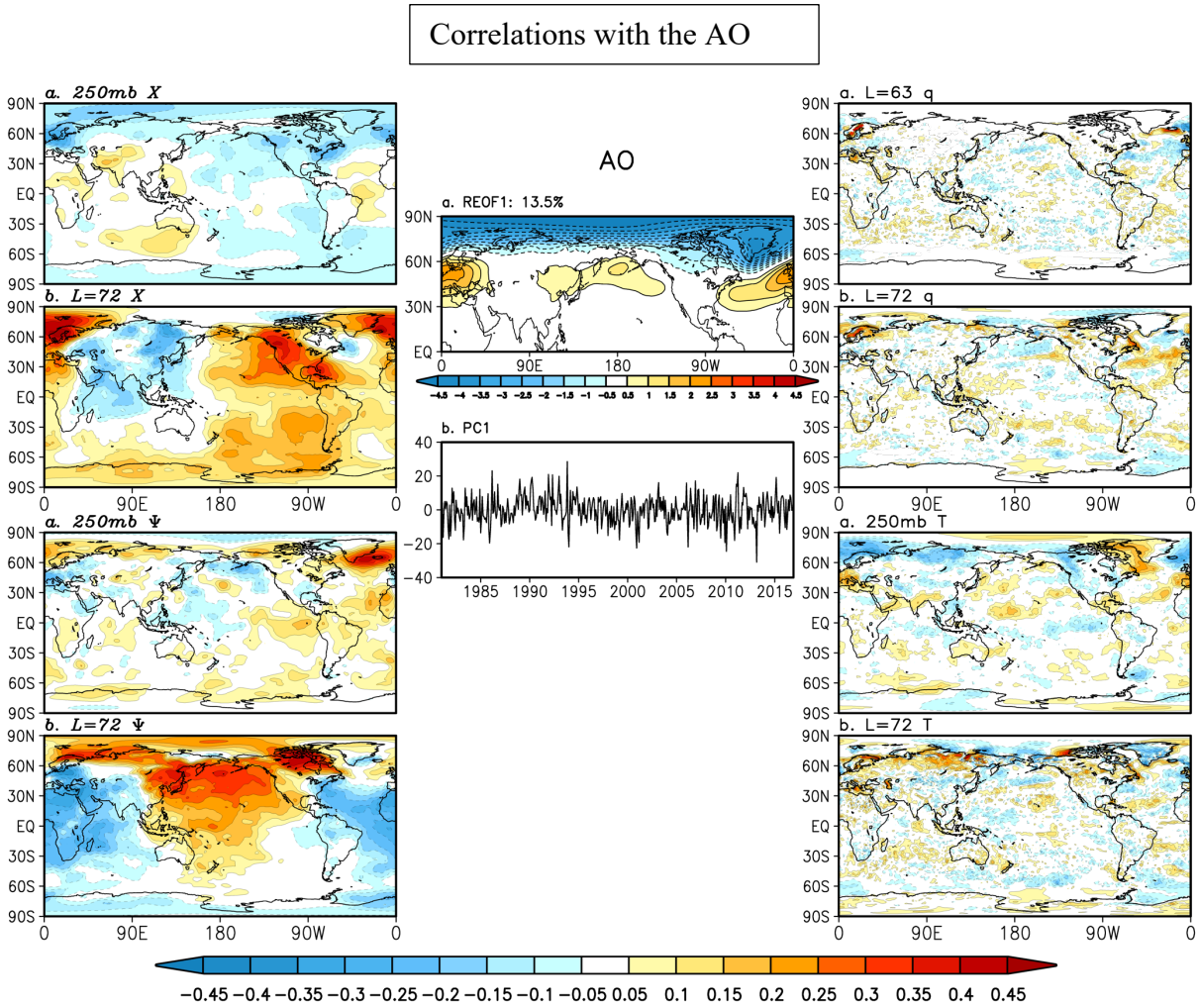

Figure 56: Same as Fig. 55 except for the Arctic Oscillation (AO). The AO is determined here as the first REOF (13.5% explained variance) of the NH 1000mb monthly ERA5 height data for the period 1981-2016.

velocity potential and stream function near the surface (left panels). In fact, the near surface correlations show global coherence (extending into the SH) and have zonal wave one structures that are approximately in quadrature. The correlations with the q and T increments are again weaker and spatially noisy (right panels of Fig. 56), with the temperature correlations showing some evidence of coherent correlations north of about 60°N at both the surface and 250mb (lower right panels).

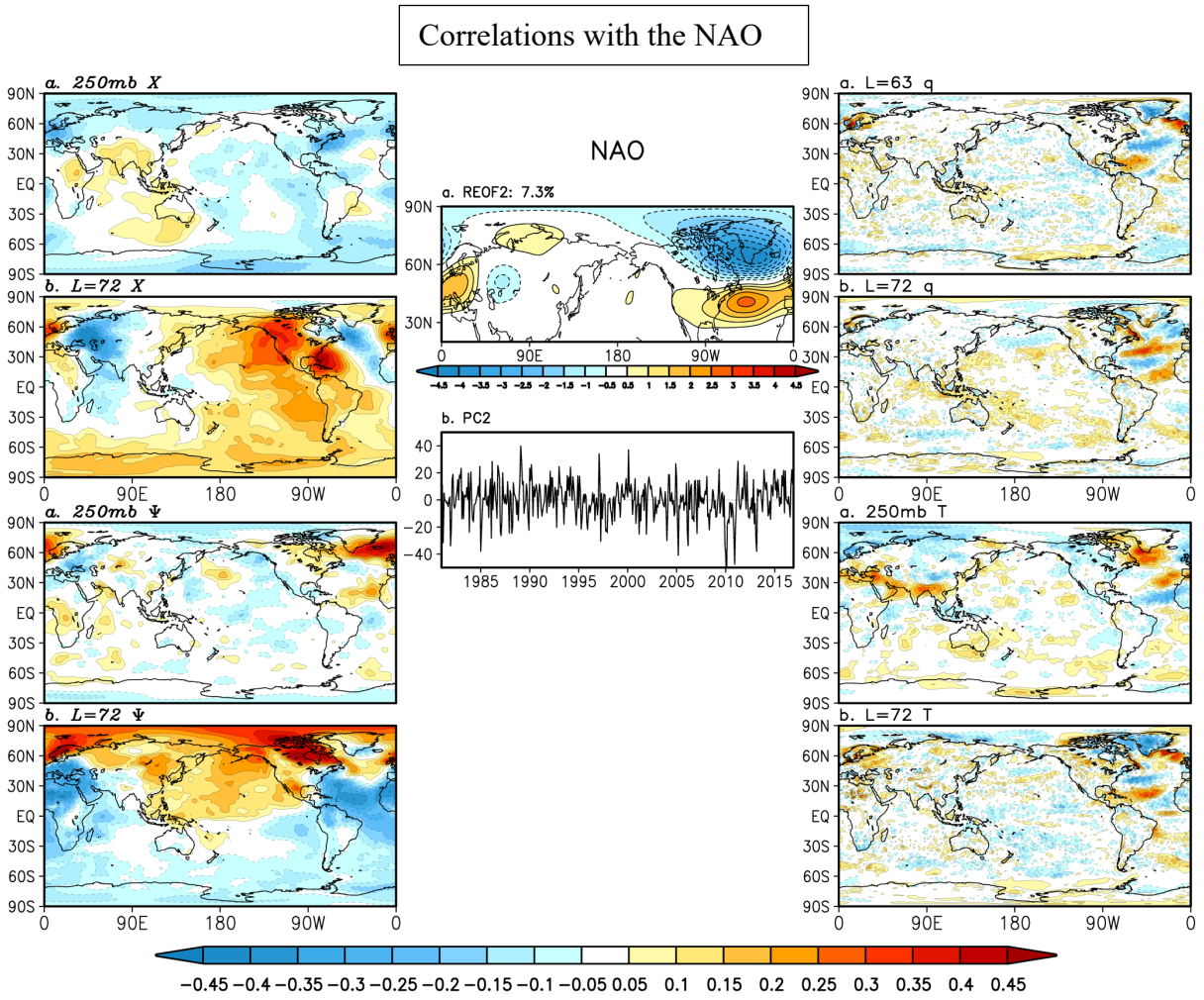

Figure 57: Same as Fig. 55 except for the North Atlantic Oscillation (NAO). The NAO is determined here as the second REOF (7.3% explained variance) of the NH 500mb monthly ERA5 height data for the period 1981-2016.

The NAO is the second leading REOF of the 500mb height field (Figure 57, middle panels) and shows (not surprisingly) very similar correlations to those for the AO for both the velocity potential and stream function increments (cf. left panels of Fig. 56 and Fig. 57). Locally the NAO is, however, more strongly correlated with the T and q increments over the North Atlantic region compared with those of the AO (right panels of Fig. 57) reflecting the longitudinally more local nature of the NAO compared with the AO. Those correlations tend to have a north/south structure and be out of phase between the surface and 250mb for both the temperature and moisture.

We also find substantial correlations between the PNA (Fig. 58, the fourth REOF of the 500mb height) and both the velocity potential and stream function increments (left panels). The largest and spatially most coherent correlations again tend to be with the near surface increments, and in this case occur over the North Pacific. For the moisture increments, the largest correlations occur near the surface over the North Pacific (showing a banded north/south structure), while for the temperature increments the 250mb level shows generally positive correlations throughout the North Pacific with weaker positive correlations extending into the tropics.

Turning next to the possible connections with ENSO, we show in Figure 59 the correlations of the increments with the monthly Niño3.4 index. In order to aid in the interpretation of those results, we show in the center panel the correlation of Niño3.4 with SST everywhere. Those show the well-known structure of ENSO SST variability in the Pacific, as well as the global reach of ENSO (via atmospheric teleconnections) into the other ocean basins. The upper left panels of Fig. 59 show what

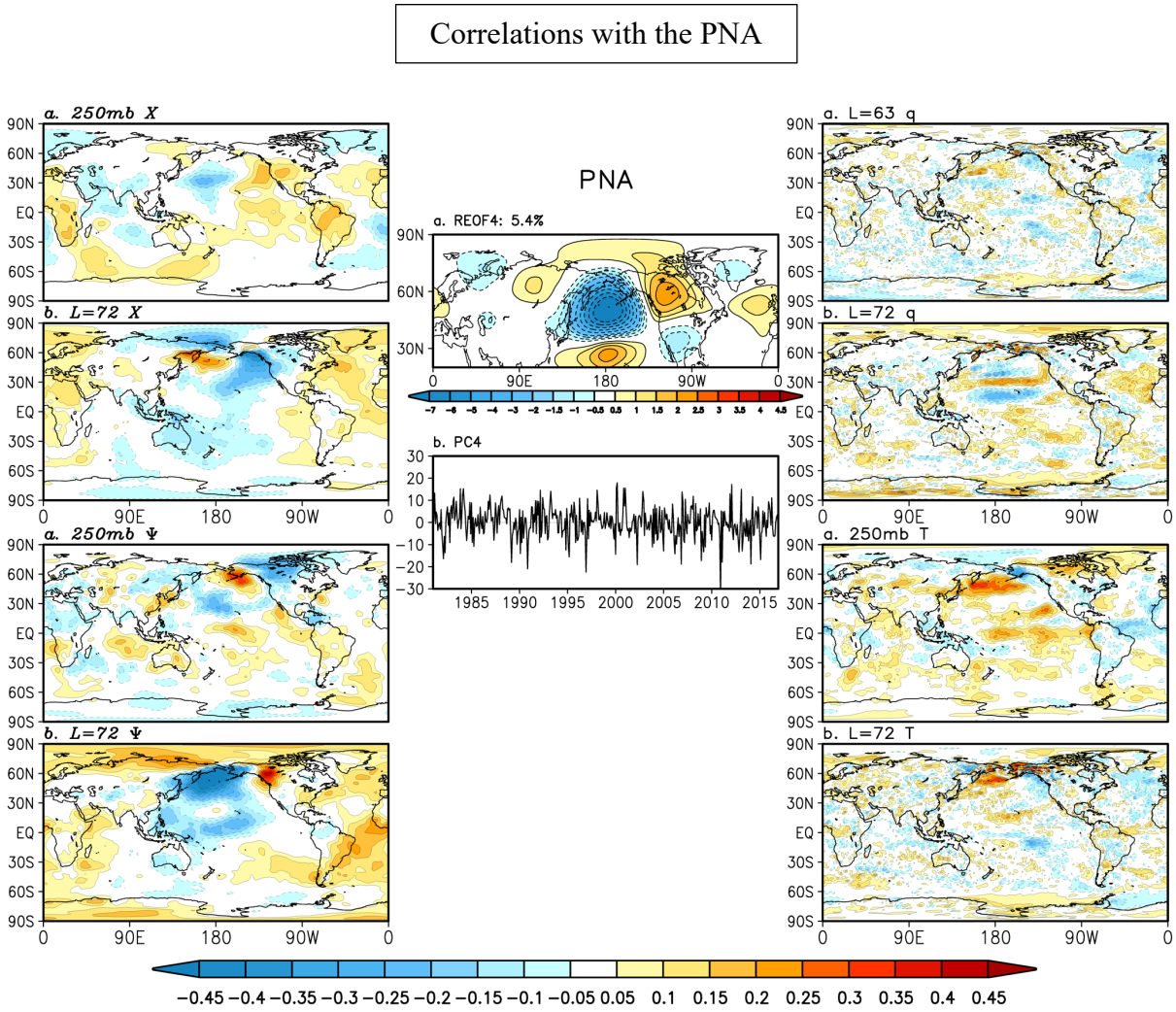

Figure 58: Same as Fig. 55 except for the Pacific/North American (PNA) pattern. The PNA is determined here as the fourth REOF (5.4% explained variance) of the NH 500mb monthly ERA5 height data for the period 1981-2016.

appear to be coherent global wave-like structures in the increment velocity potential field correlations suggesting that they are contributing to the model's global ENSO response. The connections with the increment stream function are especially coherent at the surface (lower left panel of Fig. 59) showing generally positive correlations in the SH and negative correlations in the NH – these are especially pronounced over Indonesia, the tropical eastern Pacific, and over northern South America suggestive of local stream function responses to forcing in those regions. The correlations with

moisture and temperature (right panels) show some of the strongest correlations we've seen so far (compared with the other modes), especially over the tropical Pacific (note that here we've changed the contour interval to accommodate that). In the case of moisture (upper right panels), the correlations are out of phase between the surface and L=63 (roughly 857 mb) throughout much of the tropics. At the surface the correlations with the moisture increments are the largest positive at the transition between the ENSO cold and warm anomalies just west of the dateline, while at L=63 they are the most negative slightly to the east of the dateline. The correlations with the temperature increments (lower right panels) show that the increments at 250mb are largely in phase with the SST variations, with the largest positive correlations in the tropics situated over the largest positive SST correlations (cf. middle panel with panel a of lower right). At the surface (panel b of lower right), the tropical temperature correlations are largely out of phase with those of the surface moisture increments (panel b of top right). The fact that the temperature correlations near the surface (panel b of lower right) tend to be negative throughout much of the central tropical Pacific suggests that the model may be overestimating the SST anomalies associated with ENSO.

Correlations with the Niño3.4

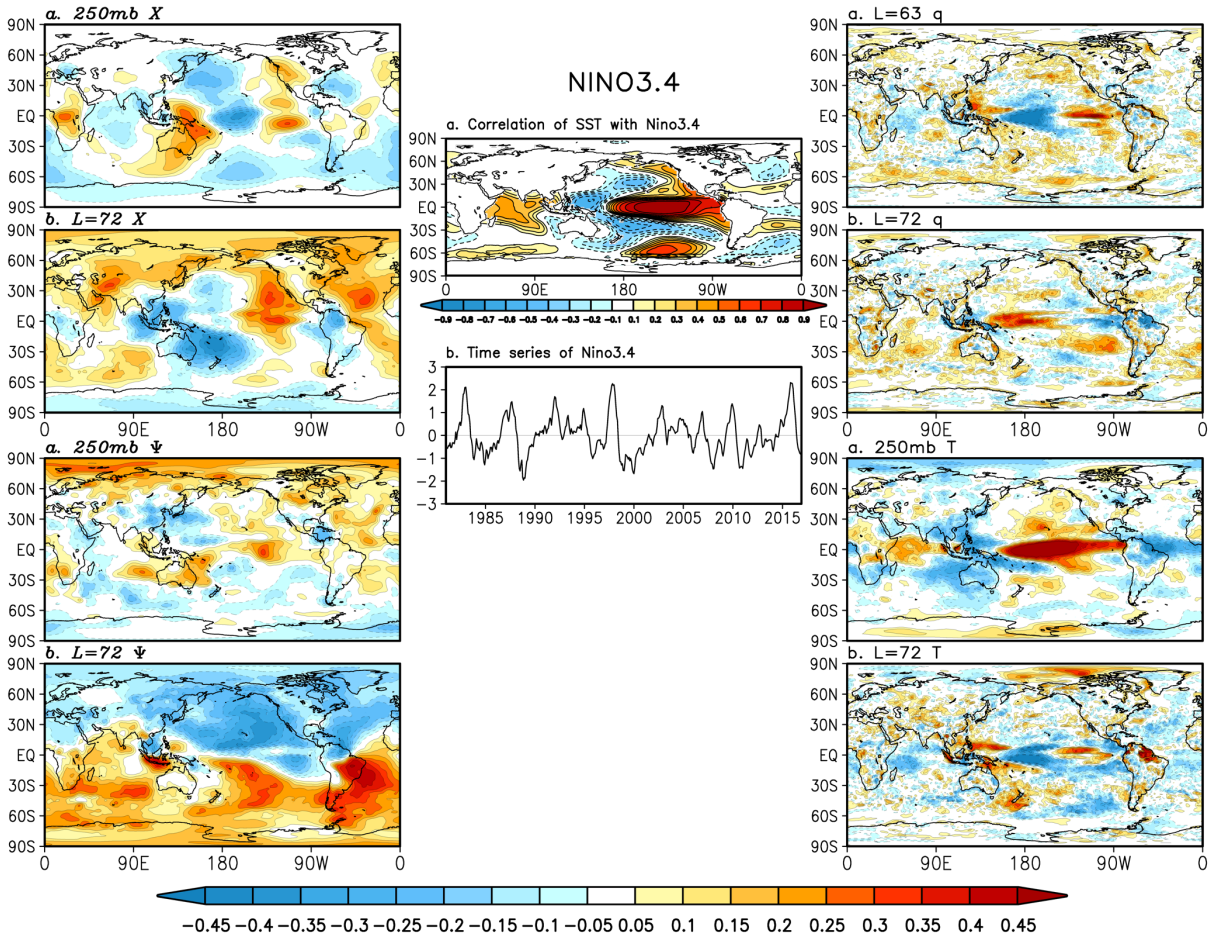

Figure 59: Same as Fig. 55 except for the Niño3.4 index. Here, the top middle panel shows the correlations between the Niño3.4 index and SST globally, and the bottom middle panel shows the time series of the Niño3.4 index for the period 1981-2016.

We next examine possible links to longer term (decadal) SST variability as reflected in the PDO (Fig. 60), recognizing that we are limited in this assessment by the shortness of our data record (we compute the REOFs using the NOAA Extended Reconstructed SST for the period 1981-2016). The PDO is isolated as the third REOF of the monthly SST (middle panel of Fig. 60), showing the typical structure of the PDO in the North Pacific. It should be noted that there is a well-known dependence of the structure of the PDO (reflecting uncertainties in the extent of a tropical connection and possible links to ENSO) on the domain and method for extracting the PDO signal

(e.g., Newman et al. 2016), but clearly our analysis here has the PDO as primarily an extratropical signal with substantial decadal-scale variability. Despite the largely extratropical signal of the PDO,

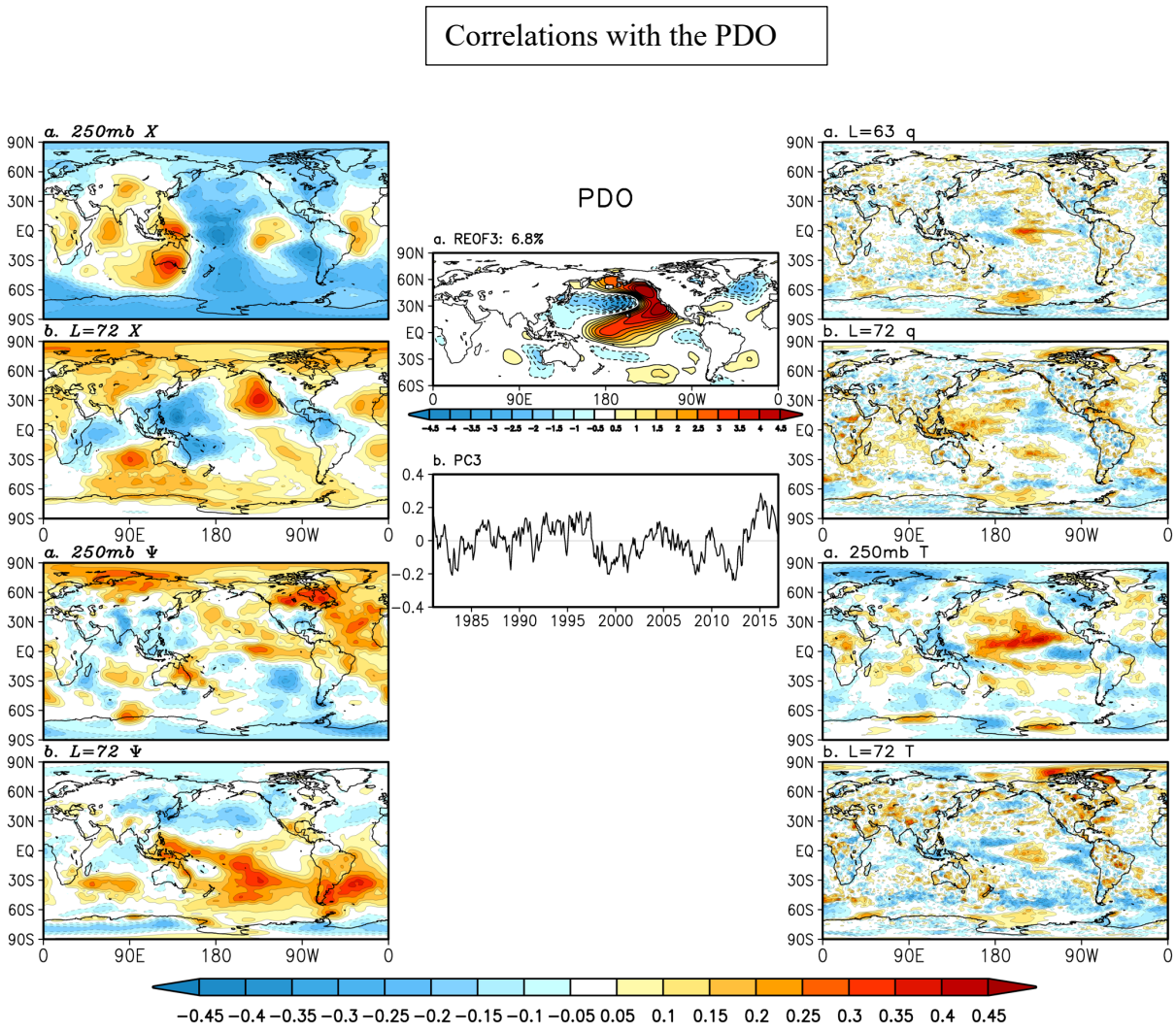

Figure 60: Same as Fig. 55 except for the PDO index. The PDO is determined here as the third REOF (6.4% explained variance) of the monthly NOAA Extended Reconstructed Sea Surface Temperature (ERSST) data for the period 1981-2016.

we do find substantial similarities with the Niño3.4 correlations for the wind increments (cf. left panels of Figs 59 and 60), especially at the surface (L=72) for the velocity potential fields. As such, it is not clear that the links to the PDO are providing substantially different linkages with the

increments that are independent of the links to ENSO. This may be in part due to the shortness of our data record.

Returning to shorter (subseasonal) time scales, we next look at the potential impacts of the MJO on the analysis increments (Figs. 61-63). Given the wave-like behavior of the MJO, we take a

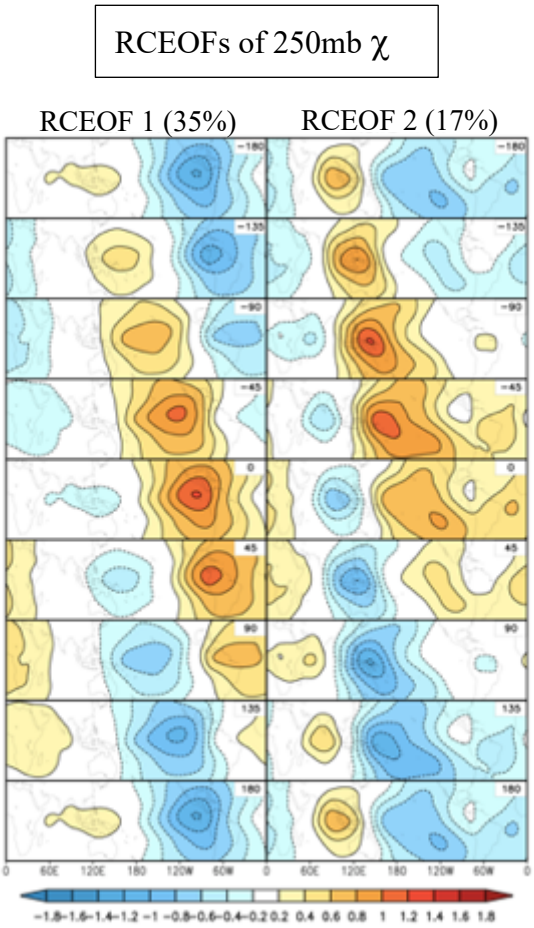

Figure 61: The Madden-Julian Oscillation (MJO) as determined from the first two rotated complex EOFs (RCEOFs) of the daily filtered (time scales longer than 10 days) 250mb velocity potential field computed from MERRA-2 data for the period 1980-2018. The first RCEOF explains 35% of the variance while the second explains 17% of the variance. The different panels indicate the different phases of the waves as they complete a circuit of the globe. See text for details.

compositing approach (rather than correlations with a single index) to assess the extent to which the analysis increments depend on the different phases of the MJO. As mentioned above, here we

employ a rotated complex EOF (RCEOF) decomposition of the daily velocity potential to better isolate the wave-like behavior of the MJO. Figure 61 shows that the first RCEOF captures about 35% of the daily low-pass filtered (time scales longer than about 10 days[4]) 250mb velocity potential variability, while the second adds another 17%. The first describes a large-scale eastward propagating wave (zonal wave number 1) characteristic of the MJO, while the second describes a roughly zonal wave number 2 disturbance that appears to reflect the more localized component of the MJO over the Indian Ocean and Pacific warm pool regions – with the latter being a region where the MJO tends to interact most strongly with convection. As such, both modes are apparently necessary to fully capture the behavior of the MJO.

We examine the impacts of the MJO by compositing those time periods when the amplitude of the first or second RCEOF (that is, the associated complex principal component, or PC) exceeds 1 standard deviation. We focus here on the potential impacts on the moisture increments. The left panels of Fig. 62 show the composite moisture increments at level 63, while the right panels show the near surface (L=72) moisture composites for RCEOF 1. While the composite increments are somewhat noisy, they do show some interesting structures. In particular, we see that at phase -45° the increments are adding moisture at level 63 (left column, four panels down) at the trailing edge of the region of large-scale sinking motion (as implied by the positive velocity potential anomalies) near the dateline, while they are removing moisture near the surface (level 72, right column, four panels down). This suggests the model is deficient in moving moisture out of the boundary layer at the *leading edge* of the active phase (the rising motion, as implied by the negative velocity potential anomalies) of the MJO – moisture the MJO presumably needs to advance the area of rising motion

[4] https://atmos.uw.edu/wallace/PDFs/Observations%20of%20low-frequency%20atmospheric%20variability.pdf

(negative velocity potential anomalies) eastward (a priming mechanism). Essentially the opposite occurs at a phase of 135° (180° out of phase).

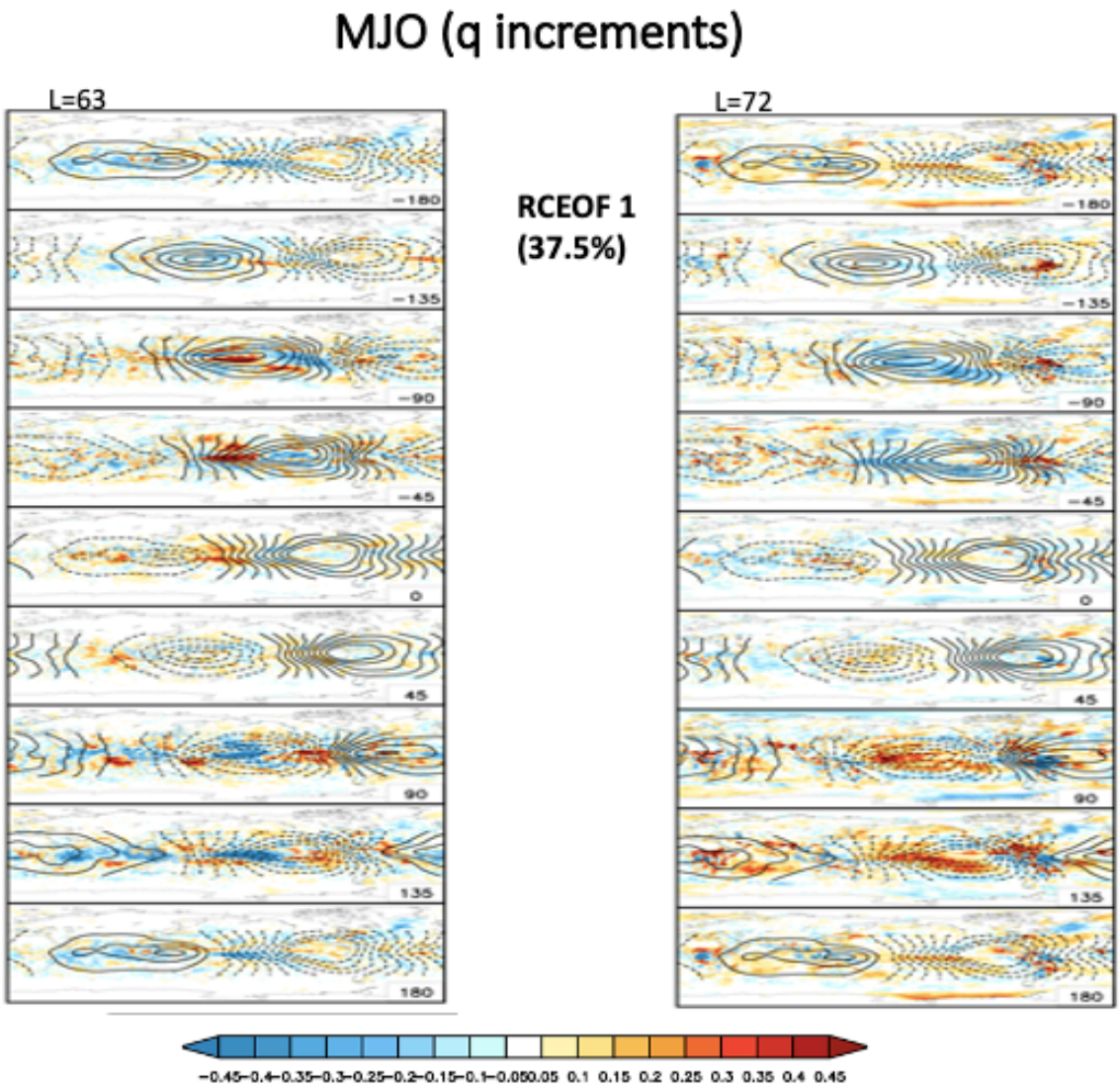

Figure 62. Composites associated with RCEOF 1 (contours) of the specific humidity increments at model level 63 (approximately 857mb, left panels) and those at model level 72 (approximately 992mb, right panels). The composites are based on those time periods when the associated complex PC 1 has magnitudes exceeding 1 standard deviation during 1981-2016.

In the case of REOF 2 (Fig. 63), a key feature appears to be the removal of moisture above the boundary layer at level 63 (left column, first panel) and addition of moisture near the surface (level

72, right column, first panel) at the *trailing edge* of the rising motion (-180° phase) as the active region of the MJO moves away from the warm pool region. Roughly the opposite occurs at °0 phase (adding moisture above the boundary layer and removing moisture near the surface). This suggests that the active phase of the MJO near the dateline removes too little moisture from above the boundary layer and takes too much moisture out of the boundary layer.

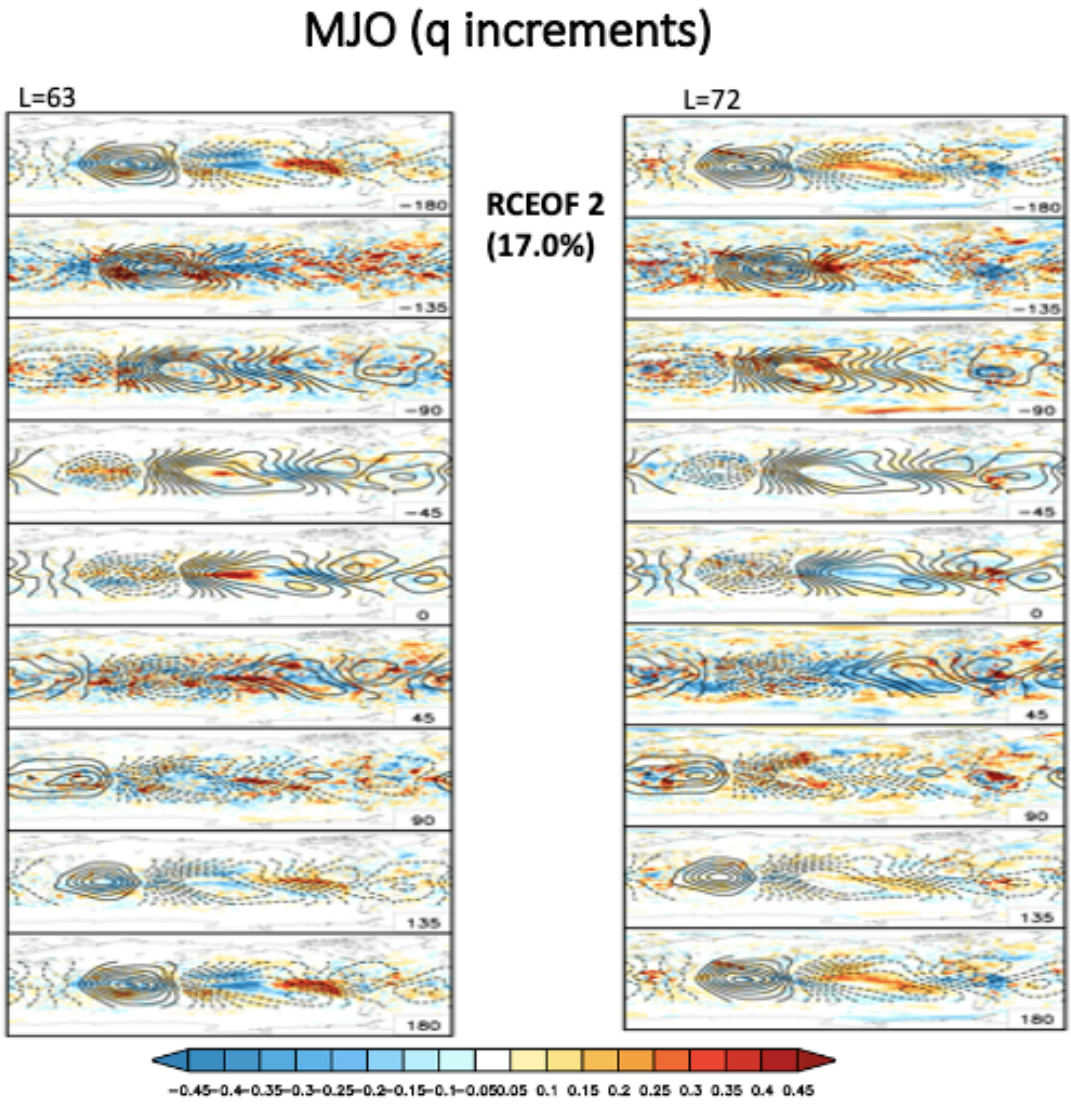

Figure 63. Same as Fig. 62 except for RCEOF 2.

Next, we turn to our second approach to addressing the links to the various climate modes, by correlating them directly with the leading REOFs (the associated monthly mean PCs) of the analysis increments discussed earlier. As mentioned earlier, this approach is more likely to show little or no linkages with the climate modes since many of those leading modes of variability in the analysis increments appear to be linked to changes in the observing system. This is borne out in Figure 64, where we present the correlations between the seven leading REOFs (the monthly averaged PCs) of the analysis increments and the monthly indices of the various climate modes. The correlations with absolute value greater than 0.19 (highlighted in red) are significant at the 1% level based on a t-test assuming roughly 200 degrees of freedom[5].

Immediately apparent is the general absence of significant correlations for the specific humidity and temperature increment PCs (right panels of Fig. 64). As we have seen, the variability of many of these PCs appears to be substantially impacted by changes in the observing system (see e.g., Fig. 41 for the temperature increments at model level 72 and Fig. 49 for the specific humidity increments at model level 72). There does appear to be a significant correlation (-.59) between REOF 1 (PC 1) of the specific humidity at model level 63 (see Fig. 52a) and Niño3.4. This REOF has most of the inspection of the time series in the right panel of Fig. 52a). As such, a connection between this PC and Niño3.4 is perhaps not surprising.

In contrast, the stream function and velocity potential increment REOFs (left panels of Fig. 64) have substantially more significant correlations, especially for the stream function REOFs at model level 72 (Fig. 64a). As we have seen, the PCs associated with these REOFs seem to be less impacted by

[5] While there are (12X36 = 420) months that are used to compute the correlations, we assume a reduced number of degrees of freedom (200) in the t-test to roughly account for serial correlation, though this is almost certainly still an overestimate in the degrees of freedom for the PDO and Niño3.4.

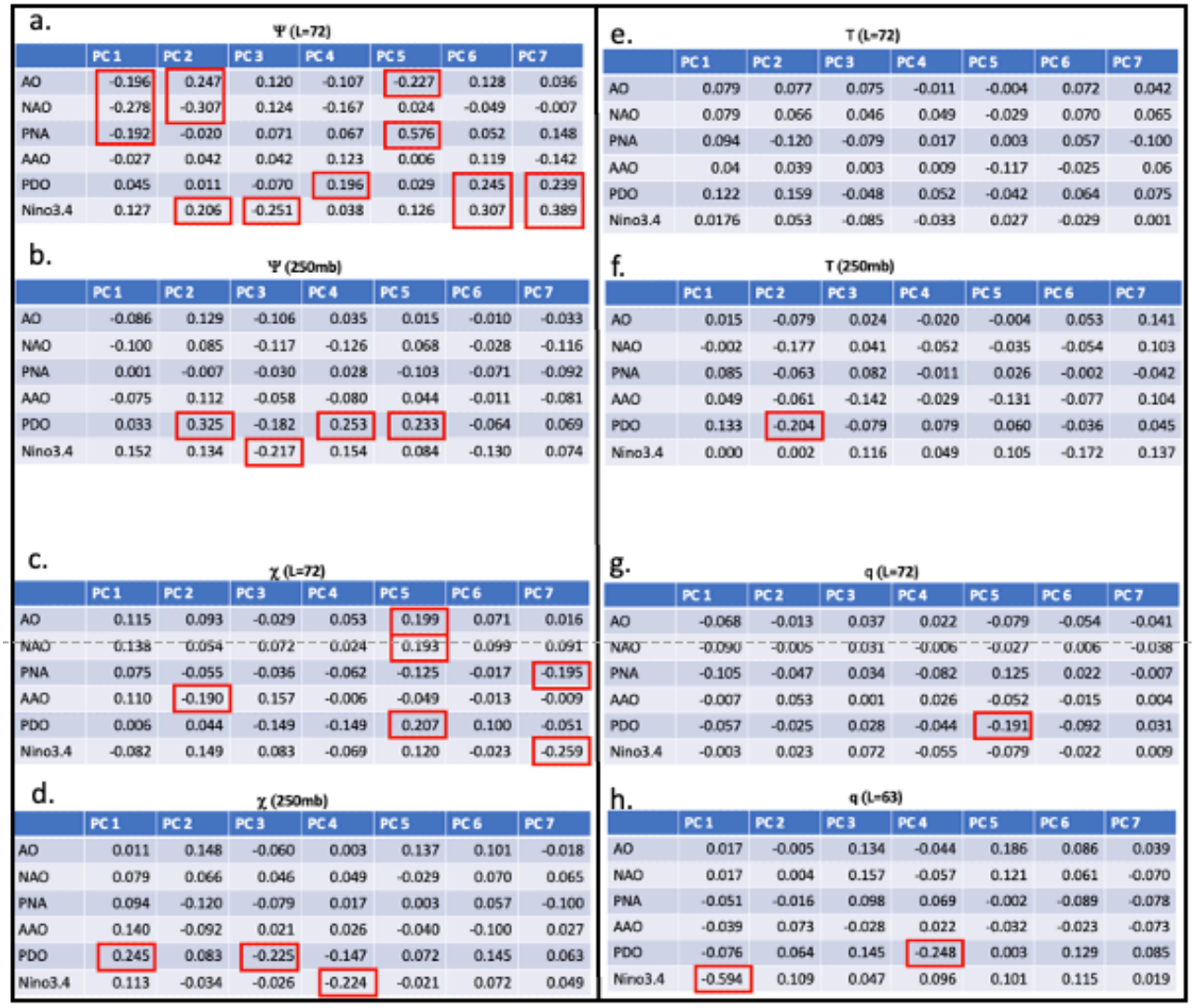

a. Ψ (L=72)

	PC 1	PC 2	PC 3	PC 4	PC 5	PC 6	PC 7
AO	-0.196	0.247	0.120	-0.107	-0.227	0.128	0.036
NAO	-0.278	-0.307	0.124	-0.167	0.024	-0.049	-0.007
PNA	-0.192	-0.020	0.071	0.067	0.576	0.052	0.148
AAO	-0.027	0.042	0.042	0.123	0.006	0.119	-0.142
PDO	0.045	0.011	-0.070	0.196	0.029	0.245	0.239
Nino3.4	0.127	0.206	-0.251	0.038	0.126	0.307	0.389

b. Ψ (250mb)

	PC 1	PC 2	PC 3	PC 4	PC 5	PC 6	PC 7
AO	-0.086	0.129	-0.106	0.035	0.015	-0.010	-0.033
NAO	-0.100	0.085	-0.117	-0.126	0.068	-0.028	-0.116
PNA	0.001	-0.007	-0.030	0.028	-0.103	-0.071	-0.092
AAO	-0.075	0.112	-0.058	-0.080	0.044	-0.011	-0.081
PDO	0.033	0.325	-0.182	0.253	0.233	-0.064	0.069
Nino3.4	0.152	0.134	-0.217	0.154	0.084	-0.130	0.074

c. χ (L=72)

	PC 1	PC 2	PC 3	PC 4	PC 5	PC 6	PC 7
AO	0.115	0.093	-0.029	0.053	0.199	0.071	0.016
NAO	0.138	0.054	0.072	0.024	0.193	0.099	0.091
PNA	0.075	-0.055	-0.036	-0.062	-0.125	-0.017	-0.195
AAO	0.110	-0.190	0.157	-0.006	-0.049	-0.013	-0.009
PDO	0.006	0.044	-0.149	-0.149	0.207	0.100	-0.051
Nino3.4	-0.082	0.149	0.083	-0.069	0.120	-0.023	-0.259

d. χ (250mb)

	PC 1	PC 2	PC 3	PC 4	PC 5	PC 6	PC 7
AO	0.011	0.148	-0.060	0.003	0.137	0.101	-0.018
NAO	0.079	0.066	0.046	0.049	-0.029	0.070	0.065
PNA	0.094	-0.120	-0.079	0.017	0.003	0.057	-0.100
AAO	0.140	-0.092	0.021	0.026	-0.040	-0.100	0.027
PDO	0.245	0.083	-0.225	-0.147	0.072	0.145	0.063
Nino3.4	0.113	-0.034	-0.026	-0.224	-0.021	0.072	0.049

e. T (L=72)

	PC 1	PC 2	PC 3	PC 4	PC 5	PC 6	PC 7
AO	0.079	0.077	0.075	-0.011	-0.004	0.072	0.042
NAO	0.079	0.066	0.046	0.049	-0.029	0.070	0.065
PNA	0.094	-0.120	-0.079	0.017	0.003	0.057	-0.100
AAO	0.04	0.039	0.003	0.009	-0.117	-0.025	0.06
PDO	0.122	0.159	-0.048	0.052	-0.042	0.064	0.075
Nino3.4	0.0176	0.053	-0.085	-0.033	0.027	-0.029	0.001

f. T (250mb)

	PC 1	PC 2	PC 3	PC 4	PC 5	PC 6	PC 7
AO	0.015	-0.079	0.024	-0.020	-0.004	0.053	0.141
NAO	-0.002	-0.177	0.041	-0.052	-0.035	-0.054	0.103
PNA	0.085	-0.063	0.082	-0.011	0.026	-0.002	-0.042
AAO	0.049	-0.061	-0.142	-0.029	-0.131	-0.077	0.104
PDO	0.133	-0.204	-0.079	0.079	0.060	-0.036	0.045
Nino3.4	0.000	0.002	0.116	0.049	0.105	-0.172	0.137

g. q (L=72)

	PC 1	PC 2	PC 3	PC 4	PC 5	PC 6	PC 7
AO	-0.068	-0.013	0.037	0.022	-0.079	-0.054	-0.041
NAO	-0.090	-0.005	0.031	-0.006	-0.027	0.006	-0.038
PNA	-0.105	-0.047	0.034	-0.082	0.125	0.022	-0.007
AAO	-0.007	0.053	0.001	0.026	-0.052	-0.015	0.004
PDO	-0.057	-0.025	0.028	-0.044	-0.191	-0.092	0.031
Nino3.4	-0.003	0.023	0.072	-0.055	-0.079	-0.022	0.009

h. q (L=63)

	PC 1	PC 2	PC 3	PC 4	PC 5	PC 6	PC 7
AO	0.017	-0.005	0.134	-0.044	0.186	0.086	0.039
NAO	0.017	0.004	0.157	-0.057	0.121	0.061	-0.070
PNA	-0.051	-0.016	0.098	0.069	-0.002	-0.089	-0.078
AAO	-0.039	0.073	-0.028	0.022	-0.032	-0.023	-0.073
PDO	-0.076	0.064	0.145	-0.248	0.003	0.129	0.085
Nino3.4	-0.594	0.109	0.047	0.096	0.101	0.115	0.019

Figure 64: The correlations between the monthly averaged PCs associated with the seven leading REOFs of the analysis increments and the monthly indices of the various climate modes (AO, AAO, PNA, AAO, PDO, and Niño3.4) for: a) the stream function increments at model level 72, b) the stream function increments at 250mb, c) the velocity potential increments at model level 72, d) the velocity potential increments at 250mb, e) the temperature increments at model level 72, f) the temperature increments at 250mb, g) the specific humidity increments at model level 72, h) the specific humidity increments at model level 63. Correlations with absolute values greater than 0.19 are significant at the 1% level (highlighted in red). See text for details.

observational discontinuities (see Fig. 28). We point out in particular the significant correlations between both PC 1 and 2 of the stream function increments at model level 72 and the AO and NAO climate modes. Recall that REOF 1 has a clear AO-like spatial structure (Fig. 26a), while REOF 2

has substantial spatial loadings over the North Atlantic and Europe (Fig. 26b), and as such, the connections with the AO and NAO are not unexpected. The largest correlation, however, occurs between PC 5 (0.58) and the PNA (Fig. 64a): the stream function REOF 5 (Fig. 28e) has the largest spatial loadings over the North Pacific, so again, that correlation is not surprising. It is also noteworthy that PC 6 and PC 7 show significant correlations with Niño3.4 and the PDO. Those REOFs (6 and 7, not shown) have the largest spatial loadings over the middle latitude South Pacific and northeastern South America/western South Atlantic, respectively.

At 250mb, REOFs 2, 4 and 5 of the stream function REOFs have some of the strongest correlations with the PDO (Fig. 64b). This is not surprising for REOF 5, which has the maximum spatial loadings concentrated over the North Pacific (Fig. 34e), but it is rather surprising for REOFs 2 (Fig. 34b) and 4 (Fig. 34d), which have the maximum loadings over the North Atlantic and South Atlantic, respectively. The results for all three of these PCs must, however, be viewed with some caution, given that these PCs appear to be substantially impacted by the changes in the observing system (Fig. 34). In the case of the 250mb velocity potential increments (Fig. 64d), the only apparent significant correlations occur with the PDO (PC 1 and PC 2) and Niño3.4 (PC 4), though it is again questionable that they are really significant given the substantial impact on the variability of these PCs from the observing system changes (Fig. 37). Also, as we noted earlier, the degrees of freedom used to assess the significance of the correlations is very likely overestimated for both Niño3.4 and (especially) the PDO.

3.4 A more direct link between increments and model errors

Here we examine whether it is possible to identify particular structural deficiencies in the GEOS model formulation based on a more careful (objective) assessment of what the variability of the increments can tell us about model error. We do this within a linear dynamical framework that is assumed to be a rough approximation of the GEOS model. In particular, we assume that the GEOS model forecast ($\vec{F}$) at time n can be written as a linear propagator (**U**) acting on the analysis ($\vec{A}$) at time n-1. As such[6],

$$\vec{F}_{\boldsymbol{n}} = \mathbf{U}\,\vec{A}_{\boldsymbol{n-1}}. \tag{5}$$

Then

$$\vec{A}_{\boldsymbol{n}} - \vec{F}_{\boldsymbol{n}} = \vec{\Delta}_{\boldsymbol{n}} \simeq \vec{A}_{\boldsymbol{n}} - \mathrm{U}\vec{A}_{\boldsymbol{n-1}},$$

and

$$\vec{A}_{\boldsymbol{n}} = \vec{\Delta}_{\boldsymbol{n}} + \mathrm{U}\vec{A}_{\boldsymbol{n-1}} \equiv \mathbf{V}\vec{A}_{\boldsymbol{n-1}}.$$

We now have a corrected forecast model

$$\vec{\mathrm{G}}_{\boldsymbol{n}} = \mathrm{V}\,\vec{A}_{\boldsymbol{n-1}}, \tag{6}$$

where the new propagator (an updated model with a state dependent correction) is

$$\mathbf{V} = \mathbf{U} + \langle \vec{\Delta}_{\boldsymbol{n}} \vec{A}^{\mathrm{T}}_{\mathrm{N-1}} \rangle\, \boldsymbol{\Sigma}^{-1}_{\mathrm{A}}\ . \tag{7}$$

In the above, $\vec{A}_{\boldsymbol{n}}$ is the analysis at time n (n-1 is 6 hours earlier). $\vec{F}_{\boldsymbol{n}}$ ($\vec{\mathrm{G}}_{\boldsymbol{n}}$) is the original (corrected) forecast valid at time n, and $\vec{\Delta}_{\boldsymbol{n}}$ is a vector of the analysis increments at time n. $\vec{A}$, $\vec{\Delta}$ and $\vec{F}$ (and $\vec{\mathrm{G}}$)

[6] We also assume that the equations are formulated for the anomalies with respect to some long-term climatology.

are vectors of length p (in general the dimension of the model consisting of, for example, all grid points and state variables of the model), while **U** and **V** are pxp square matrices. The angle brackets are time averages and $\boldsymbol{\Sigma}_A$ is the pxp analysis covariance matrix. As such, the new model operator **V** involves a correction to **U** (the uncorrected model) consisting of the covariance between the increments and the previous analysis. Note that if the increments are random in the sense that they are uncorrelated with the previous analysis, there is no correction and **V** = **U**. The hope is that we can learn something about any model structural errors from an inspection of

$$\langle \vec{\Delta}_{\boldsymbol{n}} \vec{A}_{N-1}^{T} \rangle \, \boldsymbol{\Sigma}_A^{-1} \, . \tag{8}$$

We note that including such a correction term (8) is essentially equivalent to modeling the increments to include a linear state dependent term (e.g., Chang et al. 2021).

In order to reduce the degrees of freedom and thereby improving the statistical robustness of the estimates of (8), we can first do an expansion in empirical orthogonal functions (EOFs). In particular, we expand all quantities in the EOFs of the analysis (**A)**. Then

$$\boldsymbol{\Sigma}_A^{-1} = \boldsymbol{E} \, \boldsymbol{\Gamma}_{\mathbf{A}}^{-1} \, \boldsymbol{E}^{T},$$

where **E** is the matrix of eigenvectors of $\boldsymbol{A}$, and $\boldsymbol{\Gamma}_{\boldsymbol{A}}$ is a diagonal matrix of the eigenvalues. Expanding the increments and analyses in the eigenvectors of $\boldsymbol{A}$, $\vec{e_i}$:

$$\boldsymbol{\Delta} = \sum_{\mathrm{i}} \mathrm{d_i} \; \vec{\mathrm{e}_{\mathrm{i}}},$$

and

$$\boldsymbol{A} = \sum_i \mathrm{g}_i \; \vec{e_i} \, .$$

Then

$$\langle \vec{\Delta}_{\boldsymbol{n}} \boldsymbol{A}_{n-1}^{T} \rangle \, \boldsymbol{\Sigma}_{\boldsymbol{A}}^{-\mathbf{1}} = \left(\sum_i \sum_j \langle d_i g_j \rangle \, \vec{e_i} \; \overrightarrow{e_j^{T}} \right) \, (\boldsymbol{E} \, \boldsymbol{\Gamma}_A^{-1} \, \boldsymbol{E}^{T}) \, . \tag{9}$$

In this way, by appropriately truncating the EOF expansion in (9), we can produce estimates with far fewer degrees of freedom than that contained in the full matrix (8) and therefore hopefully produce statistically more robust estimates.

However, at this stage rather than attempting to actually compute (8), or an EOF truncated version (9), we present here some preliminary results consisting simply of the spatial distribution of the lag correlations in order to get some idea of what (8) is telling us about model error. This is roughly equivalent to computing the diagonal elements of (8), normalized to produce a correlation (see below). In light of the pronounced semi-diurnal and diurnal variability of the increments resulting from the different types of observations entering the MERRA-2 analysis at different times of the day (see Section 3.2), we focus here on 1-day lags (rather than 6-hour lags). We however do include all times of the day (00z, 06z, 12z, 18z) in the calculations. In particular, we compute the lag correlation (for say temperature, T) at times n and n-1 (days) as

$$\mathrm{r_T(lag\ 1)} = \langle \Delta T_{\mathrm{n}} T_{\mathrm{n-1}} \rangle / (\langle \Delta T_{\mathrm{n}}^2 \rangle \langle T_{\mathrm{n-1}}^2 \rangle)^{1/2}. \tag{10}$$

Here, all quantities are deviations from a mean annual cycle (computed for each time of day), and the angle brackets again denote a time average. To help interpret the correlations, we can think of a local version of (7) such that:

$$\frac{\langle \Delta_{\mathrm{n}} \mathrm{a}_{\mathrm{n-1}} \rangle}{\sigma_{\mathrm{a}}^2} = \rho_{\Delta \mathrm{a}} \frac{\sigma_{\Delta}}{\sigma_{\mathrm{a}}}. \tag{11}$$

Here all quantities are now scalars (a is the analysis at a single grid point, Δ is the increment at that same point). Also, $\rho_{\Delta \mathrm{a}}$ is the correlation between the increment and the analysis one day earlier, and

σ_Δ and $\sigma_a$are the standard deviations of the increment and analysis, respectively. Then the solution to a univariate version of (7) is simply

$$a_n = v^n a_0 = (u + \rho_{\Delta a}\frac{\sigma_\Delta}{\sigma_a})^n a_0 \,. \qquad (12)$$

Assuming a stable (non-oscillating, damped) solution (0<*u*<1), a positive correlation will tend to increase the decay time, while negative correlations would tend to decrease it. In fact, the correction to *u* ($\rho_{\Delta a}\frac{\sigma_\Delta}{\sigma_a}$) could produce an unstable solution (*v*>1). This highlights a potential problem with actually implementing something like (8) as a correction to the GEOS model, in that sampling errors could lead to unstable solutions.

Figure 65 shows, for example, the correlations (11) for the temperature at the model's lowest level (L=72, roughly 992mb). We see that, throughout the year, the correlations tend to be negative over the oceans, while they tend to be positive over NH land (Fig. 65c). The positive correlations over NH land (Eurasia and North America) appear to reflect primarily the cold season correlations (DJF, Fig.65b). The tropical eastern Pacific shows an interesting north/south structure in the correlations that is especially pronounced during JJA (Fig. 65a) with positive correlations on and south of the equator and negative correlations just to the north. DJF also shows substantial negative correlations over northern South America (Fig. 65b). A possible interpretation (see above local analysis) of the negative correlations over the ocean is that the model tends to respond too strongly to the SST by not sufficiently damping the near surface temperature anomalies. This is, however, not the case in the eastern tropical Pacific cold tongue, on and just south of the equator, where the correlations tend to be positive, especially during JJA, Fig. 65a). The correlations also tend to be positive over the NH land during DJF (Fig. 65b) and over Australia and southern South America during JJA (Fig. 65a),

indicating that the model is predicting fluctuations with too short time scales over cold-season land areas.

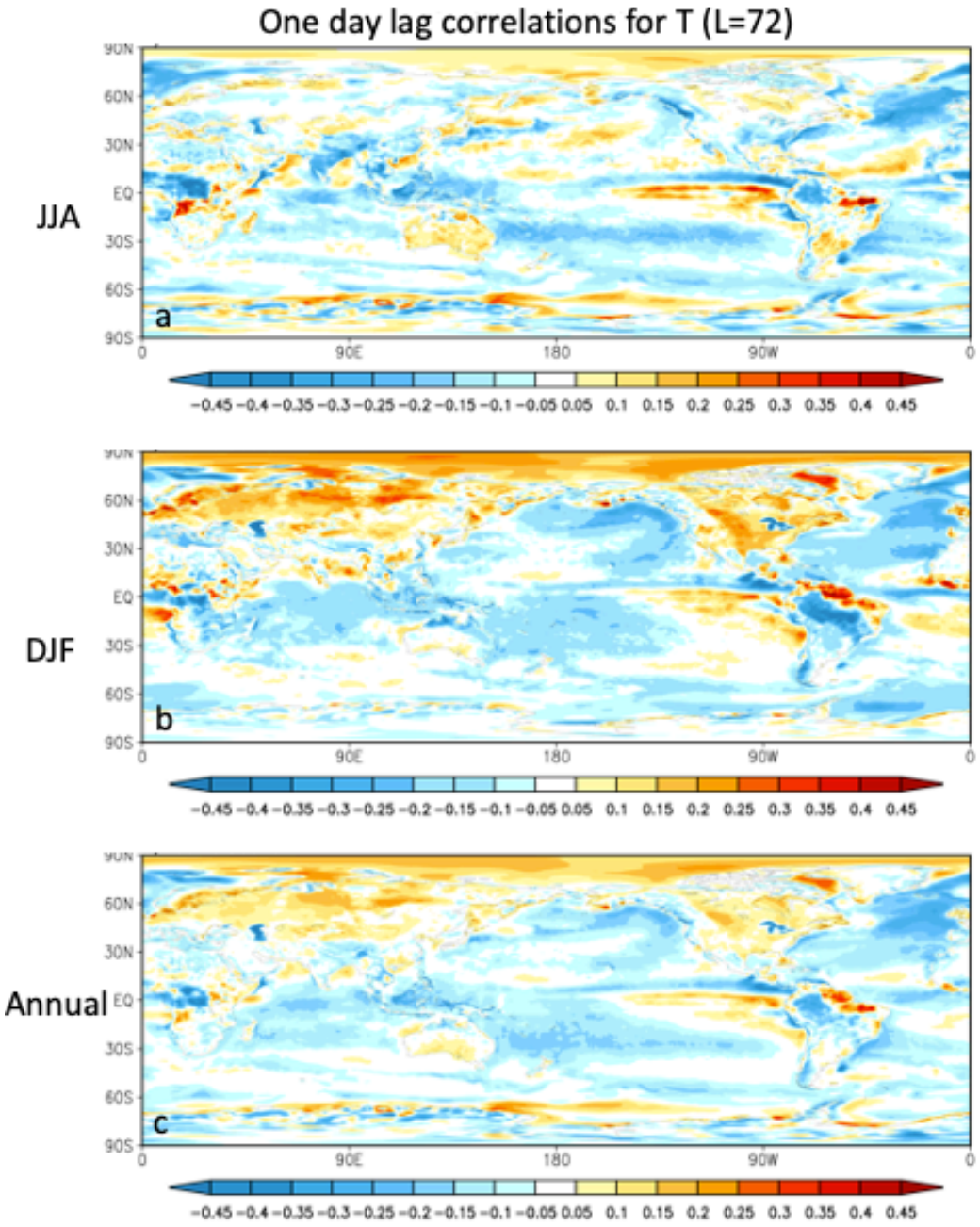

Figure 65: The correlations between the increments of the temperature at the lowest model level (L=72) at time (n) and the corresponding temperature field one day earlier [corr(ΔT_n, T_{n-1})] for a) JJA, b) DJF, and c) Annual. The calculation of the 1-day lag correlations includes all times of the day (00z, 06z, 12z and 18z). See text for details.

Figures 66 and 67 show the correlations for the specific humidity at model levels 72 (approx. 992mb) and 63 (approx. 857mb), respectively. The correlations tend to be somewhat smaller compared with those for the temperature (Fig. 65), but they are nevertheless spatially extensive with generally positive correlations over the tropical and subtropical oceans at level 72 (Fig. 66), and generally negative values over those regions at model level 63 (Fig. 67). As such, the correction (8) would act extend moisture fluctuations near the surface and shorten fluctuations above the boundary layer. Over land, the largest correlations occur at model level 72 (Fig. 66), with positive correlations tending to occur during the warm season (Fig. 66a) in both hemispheres (e.g., northern Eurasia, North America and Australia). DJF (Fig. 66b) is marked by extensive regions of negative correlations over southern Eurasia, western North America, Greenland, South America, and much of the SH high latitudes.

The implications of the above correlations for model deficiencies are of course only suggestive, and it is likely that additional, more targeted simulations in which we actually try to implement such corrections in the GEOS model would be necessary to achieve a greater understanding of those deficiencies. As such, our analysis can at best point developers in the right direction by identifying those regions of the world (and those physical processes) that require their attention.

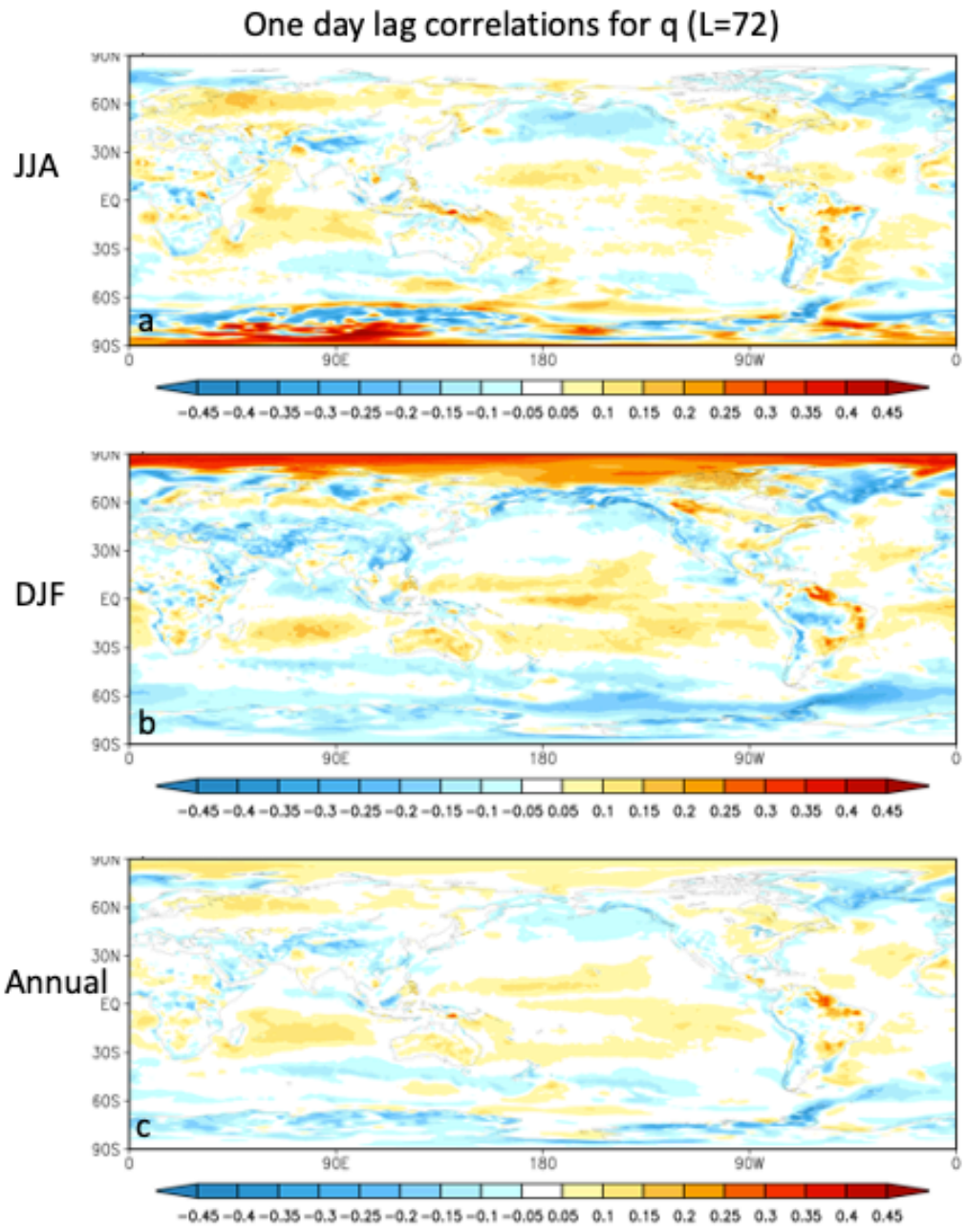

Figure 66: The correlations between the increments of the specific humidity at the lowest model level (L=72) at time (n) and the corresponding specific humidity field one day earlier [corr(Δq_n, q_{n-1})] for a) JJA, b) DJF, and c) Annual. The calculation of the 1-day lag correlations includes all times of the day (00z, 06z, 12z and 18z). See text for details.

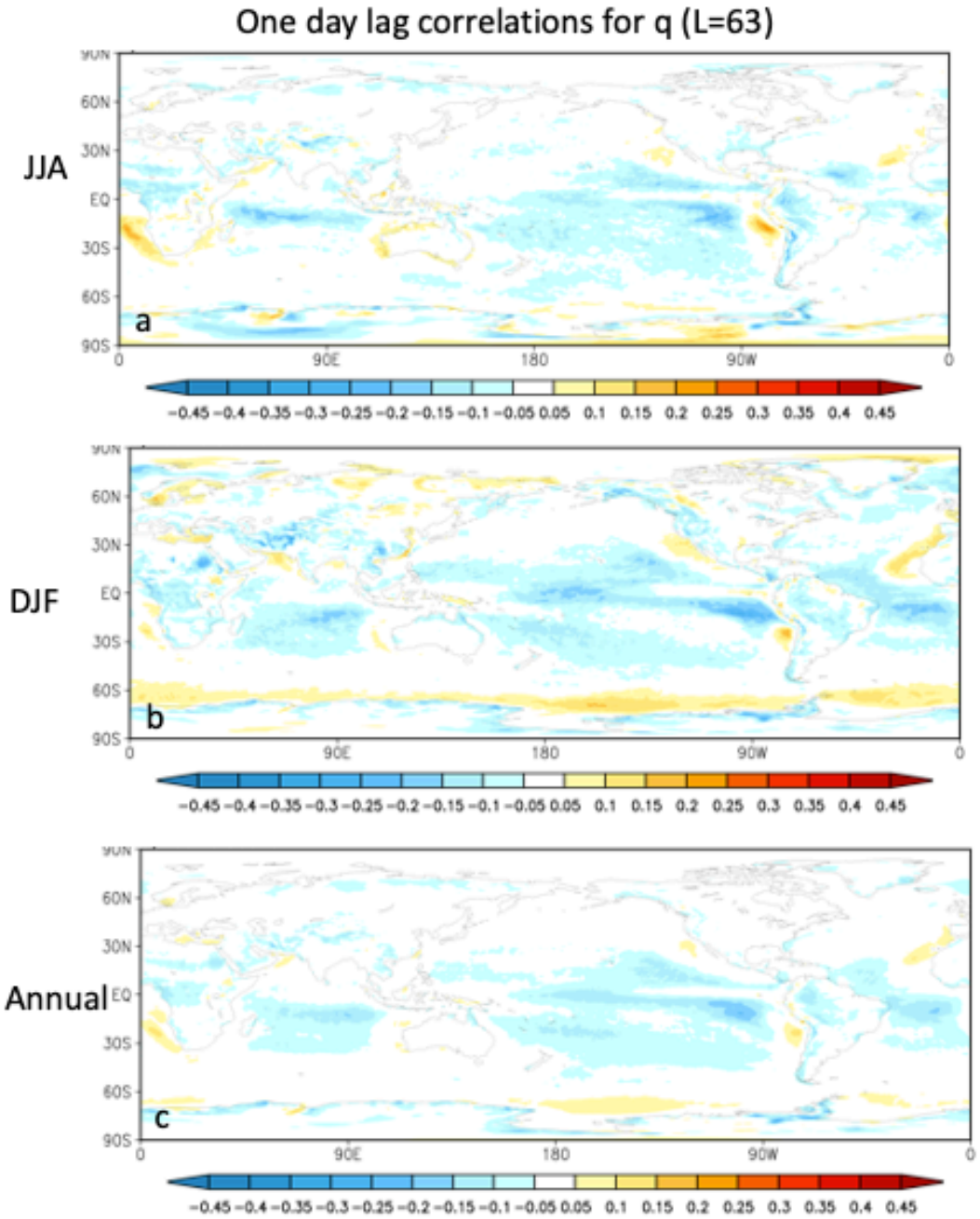

Figure 67: The correlations between the increments of the specific humidity at model level 63 at time (n) and the corresponding specific humidity field one day earlier [corr(Δq_n, q_{n-1})] for a) JJA, b) DJF, and c) Annual. The calculation of the 1-day lag correlations includes all times of the day (00z, 06z, 12z and 18z). See text for details.

4. Concluding Remarks

This report provides a comprehensive assessment of the analysis increments obtained by replaying the GEOS S2S-3 coupled model to MERRA-2 for the period 1981-2016. The results are intended to help isolate and understand 1) model deficiencies, 2) the impact on the increments from changes in the observing system, and 3) any state-dependence of the increments including potential links to some of the leading modes of climate variability. A key overarching goal is to determine the feasibility of extending the tendency bias correction methodology of Chang et al (2019) to include some type of state-dependence, thereby improving model forecast skill. Addressing model deficiencies within a replay framework benefits from the fact that we are examining errors very early in the course of a forecast (the first 6 hours) when their growth is presumably linear, so that we can hope to identify model deficiencies at the process level. This differs from the usual assessment of model climate biases, which reflect the statistically-stationary end-state of non-linear model error growth.

It is hoped that this report provides a template for routine model evaluation, especially as each new major version of the model is "frozen" and the focus turns to correcting existing deficiencies and developing the next version of the model. While the focus here is on the atmosphere (we are replaying to an atmospheric reanalysis), our approach could in principle be extended to also replaying the ocean - something we hope to do in the future once the GMAO transitions to a fully coupled reanalysis system.

Focusing first on model errors, we have shown that in some cases the improved input to the model's physical parameterizations (from replay) appears to produce improvements to the model's physical

forcing – we refer to this as correcting non-structural errors. As an example, we show how the split ITCZ of the free-running coupled model, as reflected in the model's moist heating profile, is corrected in replay mode. We contrast that with structural model deficiencies that are reflected in the time mean increments. These are deficiencies that remain even after the parameterizations are provided with improved input from replay. This could be something as simple as having insufficient resolution and/or incorrectly tuned parameterizations, or something more difficult to correct involving missing real-world physical processes. An example of a structural deficiency involves the upper tropospheric tropical time mean temperature increments which are consistently (during all seasons) positive, thereby presumably acting to correct for insufficiently deep tropical convection. As another example, we show some dependence of the time mean increments on the phase of the MJO, thereby providing some insight into how we might improve its simulation.

Turning to the observations, we have shown that the increments are indeed impacted by changes in the observing system. At the longest time scales (annual to decadal), this is especially evident for the near surface temperature and moisture increments at the ice margins of the high-latitude SH, apparently reflecting the different boundary forcings (sea ice and SST) used in MERRA-2. Overall, the introduction of AMSU and AIRS data tends to introduce a marked change in the character of many of the increments around the year 2000 (+/- 2 years). However, a substantial impact of the inhomogeneities in the observing system occurs at semi-diurnal and diurnal time scales, reflecting the different observational types entering the analysis at the different times of the day.

We have shown that, despite the spurious variability in the increments from the changing observing system, there are substantial links between the increments and climate variability on monthly time

scales. This includes links to the AO, NAO, PNA and ENSO. Some of the strongest correlations occur between Niño3.4 and tropical moisture and temperature increments, providing some of the best evidence that we should be able to introduce some kind of state dependence (based on ENSO) to the bias correction methodology.

We have also examined, within a linear framework, whether we can provide a more direct link between the increment variability and model deficiencies. The basic results of that analysis indicate that, to the extent that there is a correlation between the increments and the initial state, we can introduce a correction to the linear propagator (assumed in our analysis to represent the GEOS model). A preliminary assessment of those correlations for near surface temperature and moisture suggests that the model tends to produce near surface fluctuations that have excessively long time scales over the ocean and excessively short time scales over land areas during the cold season.

As a final note, it is important to be clear that the above state-dependent corrections are explicitly geared to improving the model's variability (versus bias correction, which was the focus of our earlier studies: Chang et al. 2019; Chang et al. 2021). Improving our understanding of what controls a model's variability is almost certainly more difficult to achieve than improving our understanding of the causes of model bias, which is in itself a difficult problem. The hope is that in addition to having a diagnostic value (learning something about model error), we can implement such corrections (as suggested by eq. 7 and/or by including an explicit dependence of the increments on particular climate phenomena) in the GEOS model and, as such, provide some improvement in the model's forecast skill (one of our key stated goals). Given the potential for introducing sampling errors that can result

in unwanted model behavior (e.g., unstable solutions, as discussed in Section 3.4), it is clear that implementing such corrections will require great care to suppress such sampling errors.

Acknowledgements and Data Availability

This study was supported by NASA MAP funding under NNG17HP01C and WBS 802678.02.17.01.33. MERRA-2 data were developed by the Global Modeling and Assimilation Office (GMAO) at NASA GSFC under funding by the NASA MAP program and disseminated through the Goddard Earth Science Data and Information Services Center (GES DISC). The data are available at https://disc.gsfc.nasa.gov/. The file specifications for the MERRA-2 output are documented in Bosilovich (2015). The GEOS coupled model replay experiment was produced by the GMAO. Output from the replay simulations is available by request.

Appendix: Additional Diagnostics

While our focus in this report is on the atmospheric increments, we provide here a few additional diagnostic fields that serve to highlight the quality of the replayed climate, focusing in particular on the precipitation and on surface and near surface fields over the ocean, and how these compare with the results from the free-running model (Base 9).

Figure A1 shows the seasonal mean precipitation from replay and from the free running (Base 9) model. What is most apparent is the tendency for Base 9 (bottom panels) to produce too much precipitation in the tropics, especially in the Pacific just north and just south of the equator, thereby contributing to the well-known problem of coupled models tending to produce a split or double ITCZ. This problem is much reduced in the replay run (top panels). Base 9 also produces too little precipitation over much of the maritime continent and southeast Asia, especially during MAM and JJA (bottom right panels). During JJA, this dry bias extends to the northeast such that the Indian subcontinent experiences little if any monsoon rainfall in the free-running model. These dry biases (during MAM and JJA) are essentially eliminated in the replay run (top right panels).

The left set of panels of Figure A2 show the SST bias from replay and from the free running (Base 9) model. While Base 9 is a major improvement over the previous version of the model (S2S-V2, see Molod et al. 2020) it nevertheless does have some warm SST biases (generally less than 1°C) in the tropics and subtropics, and especially large warm biases in the middle and high latitudes of the SH during DJF and MAM. There is also a tendency for negative biases in the NH extratropics. All these biases are reduced if not eliminated in the replay run. The right panels of Figure A2 show the surface latent heat flux bias (with respect to MERRA-2) from replay and from the free running (Base 9) model. The replay run shows overall reduced biases. For example, the relatively large

positive biases in the Indian Ocean (extending eastward into the maritime continent) during DJF and SON in Base 9 are largely eliminated in the replay run. There are however a few places where the biases have increased in the replay run. These include the negative biases over much of northern South America and equatorial Africa, and the positive biases in the NH storm tracks during DJF and MAM.

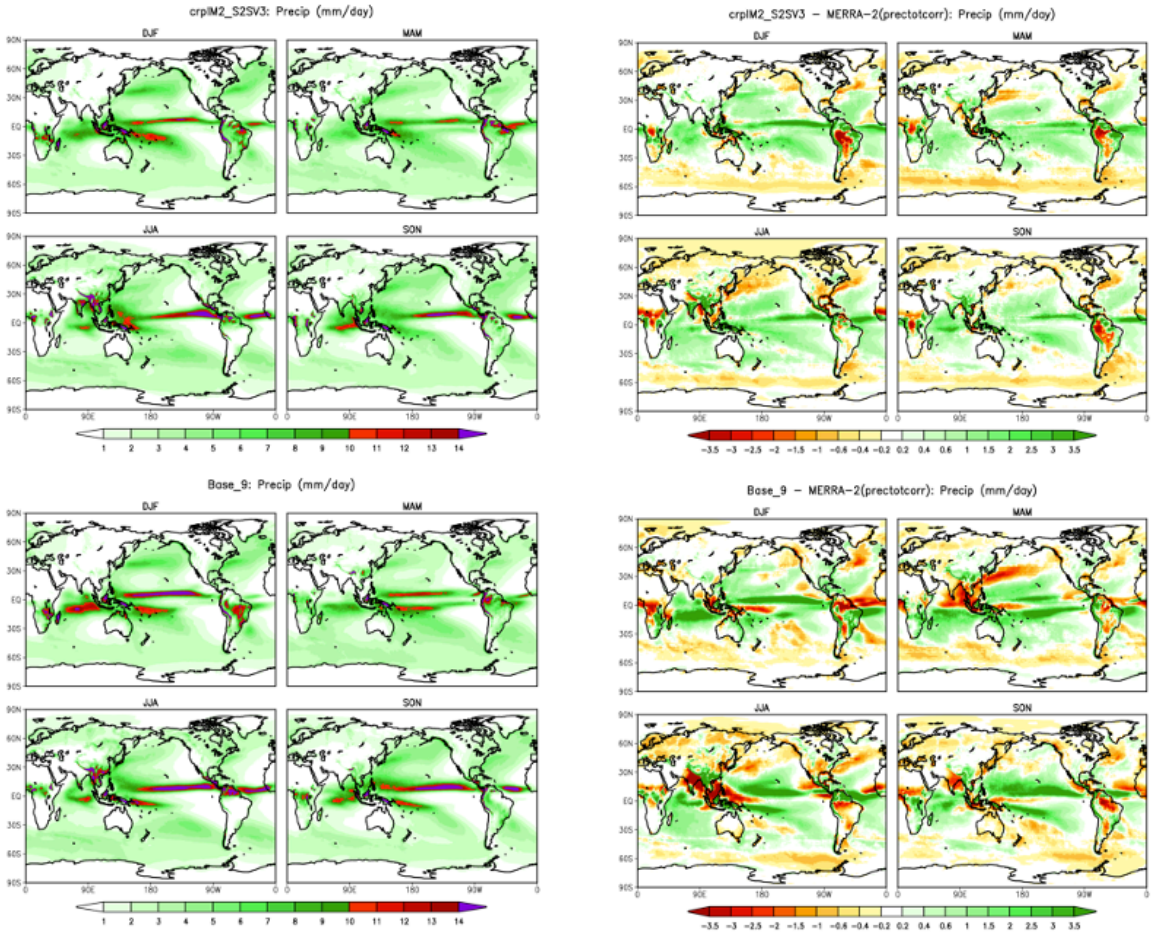

Figure A1: Left set of panels: The seasonal mean precipitation from the replay run (top panels) and the free running model (bottom panels). Right set of panels: the same as left but for the differences with respect to the MERRA-2 corrected precipitation. Units: mm/day.

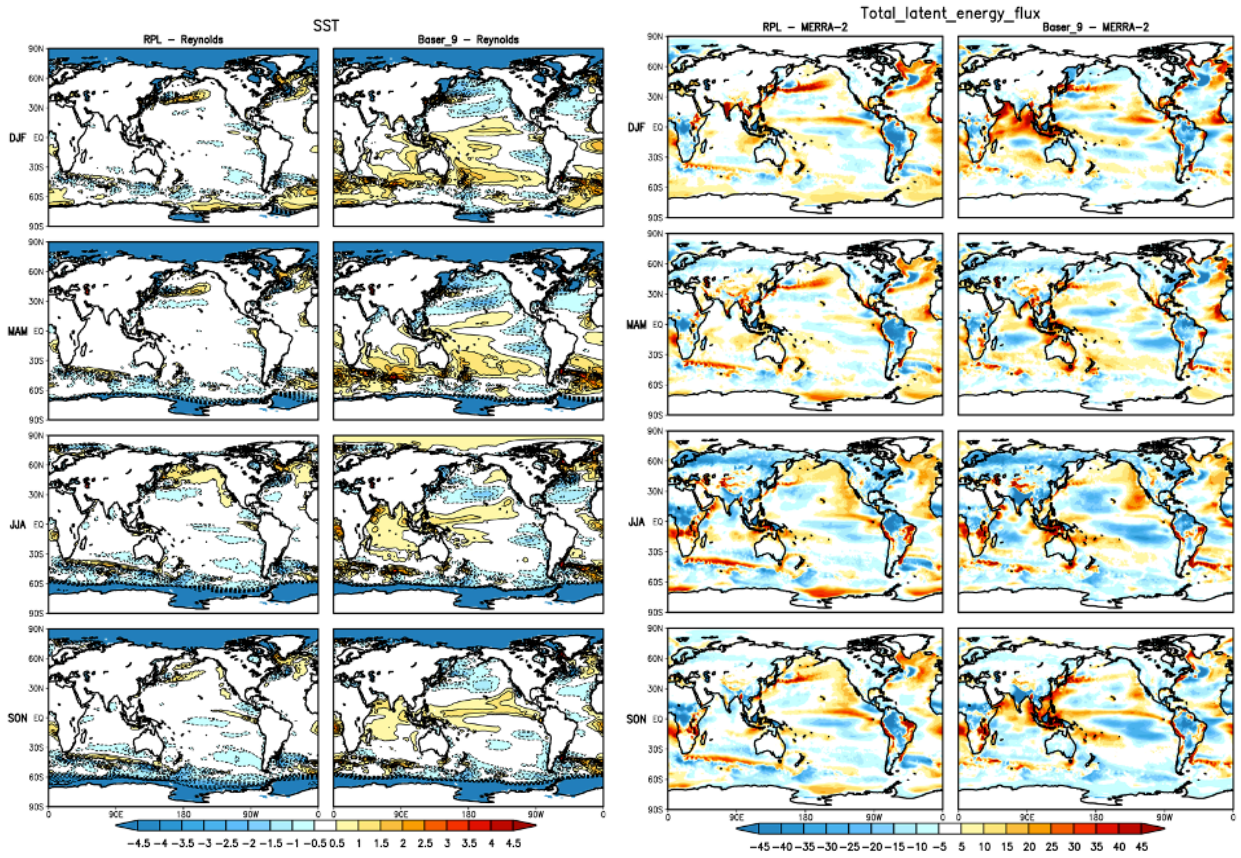

Figure A2: Left set of panels: The seasonal mean SST bias with respect to Reynolds for the replay run (first column) and the free running model (second column). Units: °C. Right set of panels: The seasonal mean surface latent energy flux bias with respect to MERRA-2 for the replay run (third column) and the free running model (fourth column). Units: W/m^2.

References

Argo (2000). Argo float data and metadata from Global Data Assembly Centre (Argo GDAC). SEANOE. https://doi.org/10.17882/42182.

Bloom, S. C., Takacs, L. L., da Silva, A. M., & Ledvina, D. (1996). Data Assimilation Using Incremental Analysis Updates, Monthly Weather Review, 124(6), 1256-1271.

Bosilovich, M. G., 2015: GMAO Office Note No. 9 (Version 1.1): MERRA-2: File Specification. Available at https://gmao.gsfc.nasa.gov/pubs/

Bosilovich, M. G., and coauthors, 2015: MERRA-2: Initial evaluation of the climate. NASA/TM–2015–104606, Vol. 43, 139 pp.

Chang, Y., Schubert, S., S-J Lin, S. Nebula, and B-W Shen, 2001: The climate of the FVCCM-3 Model. Technical Report Series on Global Modeling and Data Assimilation, Max J. Suarez, editor. NASA/TM-2001-104606, Vol. 20, 141 pp.

Chang, Y., S. Schubert, R. Koster, A. Molod and H. Wang. Tendency Bias Correction in Coupled and Uncoupled Global Climate Models with a focus on impacts over North America. J. Climate, 32, 639–661, 2019. https://doi.org/10.1175/JCLI-D-18-0598.1

Chang, Y., Schubert, S., R. Koster and A. Molod, 2021: Tendency Bias Correction in the GEOS AGCM. Technical Report Series on Global Modeling and Data Assimilation, Randal D. Koster, editor. NASA/TM-2021-104606, Vol. 57, 78 pp.

Colarco, P., da Silva, A., Chin, M., & Diehl, T. (2010). Online simulations of global aerosol distributions in the NASA GEOS-4 model and comparisons to satellite and ground-based aerosol optical depth. *Journal of Geophysical Research*, **115**, D14207

C3S (Copernicus Climate Change Service), 2017: ERA5: Fifth generation of ECMWF atmospheric reanalyses of the global climate . Copernicus Climate Change Service Climate Data Store (CDS), https://cds.climate.copernicus.eu/cdsapp#!/home

Dee, D. P., and R. Todling, 2000: Data assimilation in the presence of forecast bias: The GEOS moisture analysis. Mon. Wea. Rev., 128, 3268–3282.

Dee, D. P., and S. Uppala, 2009: Variational bias correction of satellite radiance data in the ERA-Interim reanalysis. Quart. J. Roy. Meteor. Soc., 135, 1830–1841, doi:10.1002/qj.493.

Gelaro, R., and Coauthors, 2017: The Modern-Era Retrospective Analysis for Research and Applications, Version 2 (MERRA-2). J. Climate, 30, 5419–5454, https://doi.org/10.1175/JCLI-D-16-0758.1.

Griffies, S. (2012). Elements of the Modular Ocean Model (MOM). http://mdl-mom5.herokuapp.com/web/docs/project/MOM5_elements.pdfGriffies, S., Gnanadesikan, A., Dixon, K. W., Dunne, J. P., Gerdes, R., Harrison, M. J., Rosatti, A., Russel, J. L., Samuels, B. L., Spelman, M. J., Winton, M., & Zhang, R. (2005). Formulation of an ocean model for global climate simulations. *Ocean Science*, **1**, 1025– 1035.

Hearty, T. J., III, Lee, J. N., Wu, D. L., Cullather, R., Blaisdell, J. M., Susskind, J., & Nowicki, S. M. J. (2018). Intercomparison of Surface Temperatures from AIRS, MERRA, and MERRA-2 with NOAA and GC-Net Weather Stations at Summit, Greenland, Journal of Applied Meteorology and Climatology, 57(5), 1231-1245.

Helfand, H. M., & Schubert, S. D. (1995). Climatology of the Simulated Great Plains Low-Level Jet and Its Contribution to the Continental Moisture Budget of the United States, Journal of Climate, 8(4), 784-806.

Hunke, E.C., Lipscomb, W.H., Turner, A.K., Jeffery, N. and Elliott, S., 2010. Cice: the los alamos sea ice model documentation and software user's manual version 4.1 la-cc-06-012. *T-3 Fluid Dynamics Group, Los Alamos National Laboratory*, *675*, p.500.

Koster, R. D., M. J. Suarez, A. Ducharne, M. Stieglitz, and P. Kumar, 2000: A catchment-based approach to modeling land surface processes in a general model: 1. Model structure. J. Geophys. Res., 105(D20), 24809-24822, doi:10.1029/2000JD900327.

Lin, S.-J. (2004). A vertically Lagrangian finite-volume dynamical core for global models. *Monthly Weather Review*, **132**, 2293– 2307.

Liu, W. T., and Xie, X., Double intertropical convergence zones—a new look using scatterometer, Geophys. Res. Lett., 29(22), 2072, doi:10.1029/2002GL015431, 2002.

Lu, Feiyu, M. Harrison, A. Rosati, T. Delworth, X. Yang, W. Cooke, Liwei Jia, C. McHugh, N. Johnson, M. Bushuk, Yongfei Zhang and A. Adcroft., 2020: GFDL's SPEAR Seasonal Prediction System: Initialization and Ocean Tendency Adjustment (OTA) for Coupled Model Predictions. Journal of Advances in Modeling Earth Systems 12 (2020).

McCarty, W., L. Coy, R. Gelaro, A. Huang, D. Merkova, E. B. Smith, M. Sienkiewicz, and K. Wargan, 2016: MERRA-2 input observations: Summary and initial assessment. Technical Report Series on Global Modeling and Data Assimilation, Vol. 46, NASA Tech. Rep. NASA/TM–2016–104606, 61 pp. [Available online at https://gmao.gsfc.nasa.gov/pubs/docs/McCarty885.pdf.]

Molod, A. M., L. Takacs, M. Suarez, and J. Bacmeister, 2015: Development of the GEOS-5 atmospheric general circulation model: evolution from MERRA to MERRA-2. Geosci. Model Dev., 8, 1339-1356, doi:10.5194/gmd-8-1339-2015.

Molod, A., et al., 2020: GEOS-S2S Version 2: The GMAO high-resolution coupled model and assimilation system for seasonal prediction, Journal of Geophysical Research: Atmospheres, 125(5), e2019JD031,767, doi:10.1029/2019JD031767, e2019JD031767 10.1029/2019JD031767.

Molod, A., et al., 2022: GEOS-S2S Version 3. In preparation.

Meyers, S. D., B. G. Kelly, and J. J. O'Brien, 1993: An introduction to wavelet analysis in oceanography and meteorology: With application to the dispersion of Yanai waves. Mon. Wea. Rev.,121,2858–2878.

Newman, M., Alexander, M. A., Ault, T. R., Cobb, K. M., Deser, C., Di Lorenzo, E., Mantua, N. J., Miller, A. J., Minobe, S., Nakamura, H., Schneider, N., Vimont, D. J., Phillips, A. S., Scott, J. D., & Smith, C. A. (2016). The Pacific Decadal Oscillation, Revisited, Journal of Climate, 29(12), 4399-4427.

Putman, W., and S.-J. Lin, 2007: Finite-volume transport on various cubed-sphere grids. J. Comput. Phys., 227, 55–78, doi:https://doi.org/10.1016/j.jcp.2007.07.022.

Reichle, R. H., and Q. Liu, 2014: Observation-Corrected Precipitation Estimates in GEOS-5. NASA Tech. Memo. TM–2014-104606, Vol. 35, 18 pp., https://ntrs.nasa.gov/archive/nasa/casi.ntrs.nasa.gov/20150000725.pdf.

Reichle, R. H., Liu, Q., Koster, R. D., Draper, C. S., Mahanama, S. P., & Partyka, G. S., 2017: Land surface precipitation in MERRA-2. J. Climate, 30, 1643-1664. doi: 10.1175/JCLI-D-16-0570.1.

Reynolds, R. W., N. A. Rayner, T. M. Smith, D. C. Stokes, and W. Wang, 2002: An improved in situ and satellite SST analysis for climate. *J. Climate*, **15 ,** 1609–1625.

Richman, M. B., 1986: Rotation of principal components. J. Climatol., 6, 293–335, doi:10.1002/joc.3370060305.

Rienecker, M. M., and coauthors, 2008: The GEOS-5 data assimilation system-documentation of version 5.0.1 and 5.1.0, and 5.2.0. NASA Tech. Rep. Series on Global Modeling and Data Assimilation, NASA/TM-2008-104606, 27, 92pp.

Rienecker, M.M., and Coauthors, 2011: MERRA - NASA's Modern-Era Retrospective Analysis for Research and Applications. J. Climate, 24, 3624-3648. doi: 10.1175/JCLI-D-11-00015.1.

Robertson, F. R., Bosilovich, M. G., Chen, J., & Miller, T. L. (2011). The Effect of Satellite Observing System Changes on MERRA Water and Energy Fluxes, Journal of Climate, 24(20), 5197-5217.

Schubert, S. D., Helfand, H. M., Wu, C., & Min, W. (1998). Subseasonal Variations in Warm-Season Moisture Transport and Precipitation over the Central and Eastern United States, Journal of Climate, 11(10), 2530-2555.

Schubert, S.D., Y. Chang, H. Wang, R. D. Koster and A. M. Molod, 2019: A Systematic Approach to Assessing the Sources and Global Impacts of Errors in Climate Models." J. Climate, https://doi.org/10.1175/JCLI-D-19-0189.1

Takacs, L.L., M.J. Suárez, and R. Todling, 2018: The Stability of Incremental Analysis Update. Mon. Wea. Rev., 146, 3259–3275, https://doi.org/10.1175/MWR-D-18-0117.1

Weng, H., & Lau, K. (1994). Wavelets, Period Doubling, and Time–Frequency Localization with Application to Organization of Convection over the Tropical Western Pacific, Journal of Atmospheric Sciences, 51(17), 2523-2541.

Previous Volumes in This Series

Volume 1 September 1994	*Documentation of the Goddard Earth Observing System (GEOS) general circulation model - Version 1* L.L. Takacs, A. Molod, and T. Wang
Volume 2 October 1994	*Direct solution of the implicit formulation of fourth order horizontal diffusion for gridpoint models on the sphere* Y. Li, S. Moorthi, and J.R. Bates
Volume 3 December 1994	*An efficient thermal infrared radiation parameterization for use in general circulation models* M.-D. Chou and M.J. Suarez
Volume 4 January 1995	*Documentation of the Goddard Earth Observing System (GEOS) Data Assimilation System - Version 1* James Pfaendtner, Stephen Bloom, David Lamich, Michael Seablom, Meta Sienkiewicz, James Stobie, and Arlindo da Silva
Volume 5 April 1995	*Documentation of the Aries-GEOS dynamical core: Version 2* Max J. Suarez and Lawrence L. Takacs
Volume 6 April 1995	*A Multiyear Assimilation with the GEOS-1 System: Overview and Results* Siegfried Schubert, Chung-Kyu Park, Chung-Yu Wu, Wayne Higgins, Yelena Kondratyeva, Andrea Molod, Lawrence Takacs, Michael Seablom, and Richard Rood
Volume 7 September 1995	*Proceedings of the Workshop on the GEOS-1 Five-Year Assimilation* Siegfried D. Schubert and Richard B. Rood
Volume 8 March 1996	*Documentation of the Tangent Linear Model and Its Adjoint of the Adiabatic Version of the NASA GEOS-1 C-Grid GCM: Version 5.2* Weiyu Yang and I. Michael Navon

Volume 9 March 1996	*Energy and Water Balance Calculations in the Mosaic LSM* Randal D. Koster and Max J. Suarez
Volume 10 April 1996	*Dynamical Aspects of Climate Simulations Using the GEOS General Circulation Model* Lawrence L. Takacs and Max J. Suarez
Volume 11 May 1997	*Documentation of the Tangent Linear and Adjoint Models of the Relaxed Arakawa-Schubert Moisture Parameterization Package of the NASA GEOS-1 GCM (Version 5.2)* Weiyu Yang, I. Michael Navon, and Ricardo Todling
Volume 12 August 1997	*Comparison of Satellite Global Rainfall Algorithms* Alfred T.C. Chang and Long S. Chiu
Volume 13 December 1997	*Interannual Variability and Potential Predictability in Reanalysis Products* Wie Ming and Siegfried D. Schubert
Volume 14 August 1998	*A Comparison of GEOS Assimilated Data with FIFE Observations* Michael G. Bosilovich and Siegfried D. Schubert
Volume 15 June 1999	*A Solar Radiation Parameterization for Atmospheric Studies* Ming-Dah Chou and Max J. Suarez
Volume 16 November 1999	*Filtering Techniques on a Stretched Grid General Circulation Model* Lawrence Takacs, William Sawyer, Max J. Suarez, and Michael S. Fox-Rabinowitz
Volume 17 July 2000	*Atlas of Seasonal Means Simulated by the NSIPP-1 Atmospheric GCM* Julio T. Bacmeister, Philip J. Pegion, Siegfried D. Schubert, and Max J. Suarez
Volume 18	*An Assessment of the Predictability of Northern Winter Seasonal Means with the NSIPP1 AGCM*

December 2000 — Philip J. Pegion, Siegfried D. Schubert, and Max J. Suarez

Volume 19 — *A Thermal Infrared Radiation Parameterization for Atmospheric Studies*

July 2001 — Ming-Dah Chou, Max J. Suarez, Xin-Zhong Liang, and Michael M.-H. Yan

Volume 20 — *The Climate of the FVCCM-3 Model*

August 2001 — Yehui Chang, Siegfried D. Schubert, Shian-Jiann Lin, Sharon Nebuda, and Bo-Wen Shen

Volume 21 — *Design and Implementation of a Parallel Multivariate Ensemble Kalman Filter for the Poseidon Ocean General Circulation Model*

September 2001 — Christian L. Keppenne and Michele M. Rienecker

Volume 22 — *A Coupled Ocean-Atmosphere Radiative Model for Global Ocean Biogeochemical Models*

August 2002 — Watson W. Gregg

Volume 23 — *Prospects for Improved Forecasts of Weather and Short-term Climate Variability on Subseasonal (2-Week to 2-Month) Time Scales*

November 2002 — Siegfried D. Schubert, Randall Dole, Huang van den Dool, Max J. Suarez, and Duane Waliser

Volume 24 — *Temperature Data Assimilation with Salinity Corrections: Validation for the NSIPP Ocean Data Assimilation System in the Tropical Pacific Ocean, 1993–1998*

July 2003 — Alberto Troccoli, Michele M. Rienecker, Christian L. Keppenne, and Gregory C. Johnson

Volume 25 — *Modeling, Simulation, and Forecasting of Subseasonal Variability*

December 2003 — Duane Waliser, Siegfried D. Schubert, Arun Kumar, Klaus Weickmann, and Randall Dole

Volume 26
April 2005

Documentation and Validation of the Goddard Earth Observing System (GEOS) Data Assimilation System – Version 4

Senior Authors: S. Bloom, A. da Silva and D. Dee

Contributing Authors: M. Bosilovich, J-D. Chern, S. Pawson, S. Schubert, M. Sienkiewicz, I. Stajner, W-W. Tan, and M-L. Wu

Volume 27
December 2008

The GEOS-5 Data Assimilation System - Documentation of Versions 5.0.1, 5.1.0, and 5.2.0.

M.M. Rienecker, M.J. Suarez, R. Todling, J. Bacmeister, L. Takacs, H.-C. Liu, W. Gu, M. Sienkiewicz, R.D. Koster, R. Gelaro, I. Stajner, and J.E. Nielsen

Volume 28
April 2012

The GEOS-5 Atmospheric General Circulation Model: Mean Climate and Development from MERRA to Fortuna

Andrea Molod, Lawrence Takacs, Max Suarez, Julio Bacmeister, In-Sun Song, and Andrew Eichmann

Volume 29
June 2012

Atmospheric Reanalyses – Recent Progress and Prospects for the Future.

A Report from a Technical Workshop, April 2010

Michele M. Rienecker, Dick Dee, Jack Woollen, Gilbert P. Compo, Kazutoshi Onogi, Ron Gelaro, Michael G. Bosilovich, Arlindo da Silva, Steven Pawson, Siegfried Schubert, Max Suarez, Dale Barker, Hirotaka Kamahori, Robert Kistler, and Suranjana Saha

Volume 30
December 2012

The GEOS-iODAS: Description and Evaluation

Guillaume Vernieres, Michele M. Rienecker, Robin Kovach and Christian L. Keppenne

Volume 31
March 2013

Global Surface Ocean Carbon Estimates in a Model Forced by MERRA

Watson W. Gregg, Nancy W. Casey and Cécile S. Rousseaux

Volume 32
March 2014

Estimates of AOD Trends (2002-2012) over the World's Major Cities based on the MERRA Aerosol Reanalysis

Simon Provencal, Pavel Kishcha, Emily Elhacham, Arlindo M. da Silva, and Pinhas Alpert

Volume 33 August 2014	*The Effects of Chlorophyll Assimilation on Carbon Fluxes in a Global Biogeochemical Model* Cécile S. Rousseaux and Watson W. Gregg
Volume 34 September 2014	*Background Error Covariance Estimation using Information from a Single Model Trajectory with Application to Ocean Data Assimilation into the GEOS-5 Coupled Model* Christian L. Keppenne, Michele M. Rienecker, Robin M. Kovach, and Guillaume Vernieres
Volume 35 December 2014	*Observation-Corrected Precipitation Estimates in GEOS-5* Rolf H. Reichle and Qing Liu
Volume 36 March 2015	*Evaluation of the 7-km GEOS-5 Nature Run* Ronald Gelaro, William M. Putman, Steven Pawson, Clara Draper, Andrea Molod, Peter M. Norris, Lesley Ott, Nikki Prive, Oreste Reale, Deepthi Achuthavarier, Michael Bosilovich, Virginie Buchard, Winston Chao, Lawrence Coy, Richard Cullather, Arlindo da Silva, Anton Darmenov, Ronald M. Errico, Marangelly Fuentes, Min-Jeong Kim, Randal Koster, Will McCarty, Jyothi Nattala, Gary Partyka, Siegfried Schubert, Guillaume Vernieres, Yuri Vikhliaev, and Krzysztof Wargan
Volume 37 March 2015	*Maintaining Atmospheric Mass and Water Balance within Reanalysis* Lawrence L. Takacs, Max Suarez, and Ricardo Todling
Volume 38 September 2015	*The Quick Fire Emissions Dataset (QFED) – Documentation of versions 2.1, 2.2 and 2.4* Anton S. Darmenov and Arlindo da Silva
Volume 39 September 2015	*Land Boundary Conditions for the Goddard Earth Observing System Model Version 5 (GEOS-5) Climate Modeling System - Recent Updates and Data File Descriptions* Sarith Mahanama, Randal Koster, Gregory Walker, Lawrence Takacs, Rolf Reichle, Gabrielle De Lannoy, Qing Liu, Bin Zhao, and Max Suarez
Volume 40 October 2015	*Soil Moisture Active Passive (SMAP) Project Assessment Report for the Beta-Release L4_SM Data Product*

Rolf H. Reichle, Gabrielle J. M. De Lannoy, Qing Liu, Andreas Colliander, Austin Conaty, Thomas Jackson, John Kimball, and Randal D. Koster

Volume 41
October 2015

GDIS Workshop Report

Siegfried Schubert, Will Pozzi, Kingtse Mo, Eric Wood, Kerstin Stahl, Mike Hayes, Juergen Vogt, Sonia Seneviratne, Ron Stewart, Roger Pulwarty, and Robert Stefanski

Volume 42
November 2015

Soil Moisture Active Passive (SMAP) Project Calibration and Validation for the L4_C Beta-Release Data Product

John Kimball, Lucas Jones, Joseph Glassy, E. Natasha Stavros, Nima Madani, Rolf Reichle, Thomas Jackson, and Andreas Colliander

Volume 43
September 2015

MERRA-2: Initial Evaluation of the Climate

Michael G. Bosilovich, Santha Akella, Lawrence Coy, Richard Cullather, Clara Draper, Ronald Gelaro, Robin Kovach, Qing Liu, Andrea Molod, Peter Norris, Krzysztof Wargan, Winston Chao, Rolf Reichle, Lawrence Takacs, Yury Vikhliaev, Steve Bloom, Allison Collow, Stacey Firth, Gordon Labow, Gary Partyka, Steven Pawson, Oreste Reale, Siegfried Schubert, and Max Suarez

Volume 44
February 2016

Estimation of the Ocean Skin Temperature using the NASA GEOS Atmospheric Data Assimilation System

Santha Akella, Ricardo Todling, Max Suarez

Volume 45
October 2016

The MERRA-2 Aerosol Assimilation

C. A. Randles, A. M. da Silva, V. Buchard, A. Darmenov, P. R. Colarco, V. Aquila, H. Bian, E. P. Nowottnick, X. Pan, A. Smirnov, H. Yu, and R. Govindaraju

Volume 46
October 2016

The MERRA-2 Input Observations: Summary and Assessment

Will McCarty, Lawrence Coy, Ronald Gelaro, Albert Huang, Dagmar Merkova, Edmond B. Smith, Meta Sienkiewicz, and Krzysztof Wargan

Volume 47
May 2017

An Evaluation of Teleconnections Over the United States in an Ensemble of AMIP Simulations with the MERRA-2 Configuration of the GEOS Atmospheric Model.

Allison B. Marquardt Collow, Sarith P. Mahanama, Michael G. Bosilovich, Randal D. Koster, and Siegfried D. Schubert

Volume 48
July 2017

Description of the GMAO OSSE for Weather Analysis Software Package: Version 3

Ronald M. Errico, Nikki C. Prive, David Carvalho, Meta Sienkiewicz, Amal El Akkraoui, Jing Guo, Ricardo Todling, Will McCarty, William M. Putman, Arlindo da Silva, Ronald Gelaro, and Isaac Moradi

Volume 49
March 2018

Preliminary Evaluation of Influence of Aerosols on the Simulation of Brightness Temperature in the NASA Goddard Earth Observing System Atmospheric Data Assimilation System

Jong Kim, Santha Akella, Will McCarty, Ricardo Todling, and Arlindo M. da Silva

Volume 50
March 2018

The GMAO Hybrid Ensemble-Variational Atmospheric Data Assimilation System: Version 2.0

Ricardo Todling and Amal El Akkraoui

Volume 51
July 2018

The Atmosphere-Ocean Interface Layer of the NASA Goddard Earth Observing System Model and Data Assimilation System

Santha Akella and Max Suarez

Volume 52
July 2018

Soil Moisture Active Passive (SMAP) Project Assessment Report for Version 4 of the L4_SM Data Product

Rolf H. Reichle, Qing Liu, Randal D. Koster, Joe Ardizzone, Andreas Colliander, Wade Crow, Gabrielle J. M. De Lannoy, and John Kimball

Volume 53
October 2019

Ensemble Generation Strategies Employed in the GMAO GEOS-S2S Forecast System

Siegfried Schubert, Anna Borovikov, Young-Kwon Lim, and Andrea Molod

Volume 54
August 2020

Position Estimation of Atmospheric Motion Vectors for Observation System Simulation Experiments

David Carvalho and Will McCarty

Volume 55 February 2021	*A Phenomenon-Based Decomposition of Model-Based Estimates of Boreal Winter ENSO Variability* Schubert, Siegfried, Young-Kwon Lim, Andrea Molod, and Alllison Collow
Volume 56 June 2021	*Validation Assessment for the Soil Moisture Active Passive (SMAP) Level 4 Carbon (L4_C) Data Product Version 5* John S. Kimball, K. Arthur Endsley, Tobias Kundig, Joseph Glassy, Rolf H. Reichle, and Joseph V. Ardizzone
Volume 57 July 2021	*Tendency Bias Correction in the GEOS AGCM* Yehui Chang, Siegfried Schubert, Randal Koster, and Andrea Molod
Volume 58 August 2021	*Soil Moisture Active Passive (SMAP) Project Assessment Report for Version 5 of the L4_SM Data Product* Rolf H. Reichle, Qing Liu, Randal D. Koster, Joseph V. Ardizzone, Andreas Colliander, Wade Crow, Gabrielle J. M. De Lannoy, and John S. Kimball
Volume 59 November 2021	*Observation-Corrected Land Surface Precipitation for the SMAP Level 4 Soil Moisture (Version 6) Product and the GEOS R21C Reanalysis* Rolf H. Reichle and Qing Liu
Volume 60 January 2022	*Soil Moisture Active Passive (SMAP) Project Assessment Report for Version 6 of the L4_SM Data Product* Rolf H. Reichle, Qing Liu, Randal D. Koster, Joseph V. Ardizzone, Andreas Colliander, Wade Crow, Gabrielle J. M. De Lannoy, and John S. Kimball
Volume 61 April 2022	*Validation Assessment for the Soil Moisture Active Passive (SMAP) Level 4 Carbon (L4_C) Data Product Version 6* John S. Kimball, K. Arthur Endsley, Tobias Kundig, Joseph Glassy, Rolf H. Reichle, Joseph V. Ardizzone